

ΠΑΝΑΚΕΙΑ - Παραδοτέο Π8.11 (ΠΒΕΑΑ)

Δημοσιεύσεις για την ατμοσφαιρική ρύπανση σε διεθνή περιοδικά και συνέδρια (τουλάχιστον 1)

ΠΕ 8: Ρύπανση της Ατμόσφαιρας και έκθεση πληθυσμού (JRA1)

Ημερ/νία έναρξης – λήξης: 03.09.2018 – 02.04.2022

Ημερ/νία παράδοσης: 28.02.2022

Το Ίδρυμα Ιατροβιολογικών Ερευνών της Ακαδημίας Αθηνών (ΙΙΒΕΕΑ) συμμετείχε στην ερευνητική υποδομή ΠΑΝΑΚΕΙΑ, α) με την ανάλυση μετρήσεων του στρώματος του όζοντος που πραγματοποιήθηκαν στο Κέντρο Επιπτώσεων του Περιβάλλοντος στην Υγεία του ΙΙΒΕΑΑ, και β) με την ανάλυση μετρήσεων του επιφανειακού όζοντος και του μονοξειδίου του άνθρακα που πραγματοποιήθηκαν στο συνεργαζόμενο ερευνητικό περιβαλλοντικό παρατηρητήριο Navarino Environmental Observatory (NEO) στη Μεσσηνία.

Στα πλαίσια του έργου, η ερευνητική ομάδα του ΙΙΒΕΑΑ δημοσίευσε 4 πρωτότυπες ερευνητικές εργασίες σε επιστημονικά με κριτές και πραγματοποίησε 4 ανακοινώσεις σε επιστημονικά συνέδρια, με ευχαριστίες και χρηματοδότηση από το έργο ΠΑΝΑΚΕΙΑ, όπως αναλύονται παρακάτω.

Δημοσιεύσεις σε επιστημονικά περιοδικά με κριτές

Οι δημοσιεύσεις που προέκυψαν στα πλαίσια του έργου από την ανάλυση μετρήσεων όζοντος και ηλιακής υπεριώδους ακτινοβολίας από το φασματοφωτόμετρο Brewer που λειτουργεί στο ΙΙΒΕΑΑ, ήταν οι εξής:

1. Eleftheratos, K., Zerefos, C. S., Balis, D. S., Koukouli, M.-E., Kapsomenakis, J., Loyola, D. G., Valks, P., Coldewey-Egbers, M., Lerot, C., Frith, S. M., Haslerud, A. S., Isaksen, I. S. A., and Hassinen, S.: The use of QBO, ENSO and NAO perturbations in the evaluation of GOME-2 MetOp A total ozone measurements, Atmospheric Measurement Techniques, 12, 987–1011, <https://doi.org/10.5194/amt-12-987-2019>, 2019.
2. Eleftheratos, K., Kapsomenakis, J., Zerefos, C. S., Bais, A. F., Fountoulakis, I., Dameris,

M., Jöckel, P., Haslerud, A. S., Godin-Beekmann, S., Steinbrecht, W., Petropavlovskikh, I., Brogniez, C., Leblanc, T., Liley, J. B., Querel R., and Swart, D. P. J.: Possible Effects of Greenhouse Gases to Ozone Profiles and DNA Active UV-B Irradiance at Ground Level, *Atmosphere*, 11, 228, doi:10.3390/atmos11030228, 2020.

3. Raptis, P., Eleftheratos, K., Kazadzis, S., Kosmopoulos, P., Papachristopoulou, K., and Solomos, S.: The combined effect of ozone and aerosols on erythemal irradiance in an extremely low ozone event during May 2020, *Atmosphere*, 12, 145, <https://doi.org/10.3390/atmos12020145>, 2021.
4. Eleftheratos, K., Kouklaki, D., and Zerefos, C. S.: 16 years of measurements of ozone over Athens, Greece with a Brewer spectrophotometer, *Oxygen*, 1(1), 32–45, <https://doi.org/10.3390/oxygen1010005>, 2021.

Η πρώτη εργασία είχε σκοπό να αναδείξει την επίδραση βασικών κλιματικών διαταραχών στην μεταβλητότητα της ολικής στήλης του όζοντος στα μέσα και στα μεγάλα γεωγραφικά πλάτη. Οι κλιματικές διαταραχές που μελετήθηκαν ήταν η Σχεδόν Διετής Κύμανση (QBO), η Νότια Κύμανση (ENSO) και η Κύμανση του Βορείου Ατλαντικού Ωκεανού (NAO). Συγκρίθηκαν οι επίγειες μετρήσεις του όζοντος με τις μετρήσεις σύγχρονων δορυφορικών οργάνων (GOME-2A) για την περίοδο 2007-2016. Οι μέσες διαφορές ήταν της τάξεως του $-0.7 \pm 1.4\%$ στους τροπικούς, $0.1 \pm 2.1\%$ στα μέσα γεωγραφικά πλάτη, και $2.5 \pm 3.2\%$ και $0.0 \pm 4.3\%$ στα βόρεια και νότια μεγάλα γεωγραφικά πλάτη, αντίστοιχα. Οι δορυφορικές και οι επίγειες μετρήσεις συμφωνούν πολύ καλά ως προς τις επιδράσεις των φυσικών διακυμάνσεων QBO, ENSO, NAO. Οι διαφορές μεταξύ του όζοντος από τις δορυφορικές και τις επίγειες μετρήσεις λόγω της QBO είναι εντός του 1% στις τροπικές περιοχές. Οι διαφορές μεταξύ των δορυφορικών και των επίγειων μετρήσεων στο νησί Σαμόα (Αμερικανική Σαμόα) είναι εντός του $\pm 1.9\%$. Βρήκαμε πολύ καλή συμφωνία μεταξύ των δορυφορικών και επίγειων μετρήσεων όζοντος στον Καναδά και την Ευρώπη ως προς τη μεταβλητότητα που σχετίζεται με το NAO, με τις μέσες διαφορές να φθάνουν τα επίπεδα του 1%. Η συμφωνία και οι μικρές διαφορές που βρέθηκαν μεταξύ των δορυφορικών και των επίγειων δεδομένων όζοντος ως προς την επίδραση των QBO, ENSO και NAO έδειξαν τη σημασία αυτών των κλιματολογικών δεικτών για την παρακολούθηση της μακροχρόνιας σταθερότητας των δορυφορικών – επίγειων διαφορών.

Η δεύτερη εργασία επικεντρώθηκε στη μελέτη του αντίκτυπου της μείωσης των στρατοσφαιρικών αλογόνων (χημεία) και της αύξησης των αερίων του θερμοκηπίου (υπερθέρμανση) στις αλλαγές του στρατοσφαιρικού όζοντος. Δόθηκε προσοχή στην επίδραση των αερίων του θερμοκηπίου στην υπεριώδη-B ακτινοβολία στο έδαφος. Χρησιμοποιήθηκαν επίγειες και δορυφορικές μετρήσεις όζοντος καθώς και προσομοιώσεις μοντέλων χημείας-μεταφοράς και χημείας-κλίματος. Προέκυψε ότι (α) η μείωση των αλογόνων μεγιστοποιεί την ανάκαμψη του όζοντος στα 1,7 hPa, κάτι που παρατηρείται σε όλους τους επίγειους σταθμούς, και (β) ότι σημαντική επίδραση των αερίων του θερμοκηπίου στην ανάκαμψη του στρατοσφαιρικού όζοντος προβλέπεται μετά το έτος 2050. Τα αποτελέσματα έδειξαν ότι η υπεριώδης-B ηλιακή ακτινοβολία που προκαλεί βλάβη στο DNA θα αυξηθεί μετά το έτος 2050 κατά +1,3% ανά δεκαετία. Μια τέτοια αλλαγή οφείλεται σε μια σημαντική μείωση της νεφοκάλυψης λόγω της εξέλιξης των αερίων του θερμοκηπίου στο μέλλον και μιας ασήμαντης τάσης στο ολικό όζον. Εάν οι εκτιμήσεις αποδειχθούν αληθείς, τότε είναι πιθανό ότι η διαδικασία της κλιματικής αλλαγής θα κατακλύσει την επίδραση της ανάκαμψης του όζοντος στην ακτινοβολία UV-B στα μέσα πλάτη.

Η τρίτη εργασία εστίασε στις μετρήσεις υπεριώδους ακτινοβολίας στην περιοχή της Αθήνας, κατά τη διάρκεια ενός επεισοδίου με χαμηλή ποσότητα ολικού όζοντος. Κατά την περίοδο 12-19 Μαΐου 2020, η ολική στήλη του όζοντος έδειξε εξαιρετικά χαμηλές τιμές, περίπου 35-55 μονάδες Dobson (έως 15%) κάτω από το μέσο όρο (μικρότερες του 2σ). Αυτή η κατάσταση ευνόησε την αύξηση της υπεριώδους ακτινοβολίας UV, καθώς το στρατοσφαιρικό όζον είναι ο σημαντικότερος παράγοντας εξασθένισης στη φασματική περιοχή UV-B. Ταυτόχρονα, μία εισβολή αερολυμάτων σκόνης από την έρημο Σαχάρα σκίασε ένα μεγάλο μέρος της επίδρασης του χαμηλού όζοντος στην υπεριώδη ακτινοβολία. Για να διερευνηθούν οι επιδράσεις των δύο φαινομένων, αναλύθηκαν οι φασματικές ηλιακές μετρήσεις από το φασματοφωτόμετρο PSR, οι μετρήσεις του ολικού όζοντος από το φασματοφωτόμετρο Brewer και υπολογισμοί από μοντέλο διάδοσης της ακτινοβολίας. Οι υπολογισμοί του δείκτη UV έδειξαν αύξηση κατά ~30% σε σχέση με τις μακροχρόνιες τιμές του δείκτη λόγω του χαμηλού όζοντος, ενώ ταυτόχρονα τα αερολύματα σκίαζαν αυτό το αποτέλεσμα σε συγκεκριμένες ημέρες κατά ~20%. Το μοντέλο χρησιμοποιήθηκε για τη διερεύνηση της απόκρισης αυτών των μεταβολών στη φασματική περιοχή UV σε διάφορες ηλιακές ζενίθιες γωνίες. Τα προσομοιωμένα φάσματα συγκρίθηκαν με τις μετρήσεις και βρέθηκε μια μέση διαφορά της τάξεως του 2%. Η μελέτη επισήμανε τη σημασία των ακριβών μετρήσεων και των προβλέψεων του όζοντος και των

αερολυμάτων για τον υπολογισμό του δείκτη UV υπό ασυνήθιστες συνθήκες χαμηλού όζοντος – υψηλής συγκέντρωσης αερολυμάτων.

Η τέταρτη εργασία παρουσίασε τα επίπεδα του στρώματος του όζοντος στο αστικό περιβάλλον της Αθήνας από τις μετρήσεις του φασματοφωτόμετρου Brewer που λειτουργεί στο ΙΙΒΕΑΑ από τον Ιούλιο του 2003. Το στρώμα του όζοντος παρουσιάζεται σταθεροποιημένο κατά την τελευταία 18ετία πάνω από την Αττική, χωρίς να παρατηρείται κάποια σημαντική αλλαγή. Η μέση τιμή του στρώματος του όζοντος παραμένει σταθερή στις 320 μονάδες Dobson, ποσότητα που αντιστοιχεί σε ένα στρώμα πάχους 3,2 χιλιοστών. Τα δεδομένα του όζοντος από το φασματοφωτόμετρο Brewer συγκρίθηκαν με τα δορυφορικά δεδομένα TOMS, OMI και GOME-2A. Τα αποτελέσματα έδειξαν εξαιρετικές συσχετίσεις μεταξύ των επίγειων και των δορυφορικών δεδομένων μεγαλύτερες από 0,9. Τέλος, μελετήθηκε η μεταβλητότητα του στρώματος του όζοντος στην Αθήνα λόγω των εποχιακών μεταβολών, της σχεδόν διετούς κύμανσης (Quasi Biennial Oscillation), της νότιας κύμανσης (El Nino Southern Oscillation), της κύμανσης του Βορείου Ατλαντικού Ωκεανού (North Atlantic Oscillation), της ενδεκαετούς ηλιακής δραστηριότητας (11-year solar cycle) και των μεταβολών του ύψους της τροπόπαυσης.

Ανακοινώσεις σε επιστημονικά συνέδρια

Οι ανακοινώσεις σε επιστημονικά συνέδρια στις οποίες παρουσιάστηκαν μετρήσεις από το φασματοφωτόμετρο Brewer του ΙΙΒΕΑΑ και από τους αναλυτές αέριων ρύπων όζοντος και μονοξειδίου του άνθρακα του Navarino Environmental Observatory (N.E.O.), ήταν οι εξής:

1. Eleftheratos, K., Zerefos, C., Kapsomenakis, J., Bais, A., Fountoulakis, I., Dameris, M., Haslerud, A. S., Godin-Beekmann, S., Steinbrecht, W., Petropavlovskikh, I.: A note on possible effects of the unexpected increase in global CFC-11 to ozone profiles and erythemal doses at ground level, International Symposium On: The Unexpected Increase in Emissions of Ozone-Depleting CFC-11, Vienna, Austria, 25–27 March 2019.
2. Eleftheratos, K., Stavrika, T., and Zerefos, C.: 15 years of measurements of total ozone over Athens, Greece with a Brewer spectrophotometer, First scientific conference PANACEA, University of Crete, Heraklion, 23–24 September 2019.

3. Weber M., Schüller L., and Eleftheratos K.: The role of Dobsons and Brewers in satellite ground-truthing: Will that change in the future?, Commemorative event celebrating 20 Years WMO Regional Dobson Calibration Centre Europe / Middle East, Invitation by Dr. Ulf Köhler and Dr. Wolfgang Steinbrecht, Meteorological Observatory Hohenpeissenberg, 2 October 2019.
4. Stavraka, T., Eleftheratos, K., Kapsomenakis, J., Zerefos, C., Gerasopoulos, E., Pantazis, C., Maneas, G., Kouvarakis, G., and Mihalopoulos, N.: Ozone and carbon monoxide measurements at the Navarino Environmental Observatory (NEO) in Messenia, Greece, Second scientific conference PANACEA, Web Conferencing, 29 September – 1 October 2020.

Στην πρώτη ανακοίνωση παρουσιάστηκαν οι πιθανές επιπτώσεις από την απροσδόκητη αύξηση του παγκόσμιου CFC-11 στα προφίλ του στρατοσφαιρικού όζοντος και στην ερυθματογόνο ακτινοβολία που φτάνει στο έδαφος σε διάφορα γεωγραφικά πλάτη.

Η δεύτερη ανακοίνωση οδήγησε στη δημοσίευση με αριθμό 4 από τους Eleftheratos et al. (2021).

Στην τρίτη ανακοίνωση γιορτάστηκαν τα 20 χρόνια λειτουργίας του κέντρου βαθμονόμησης των φασματοφωτόμετρων Dobson του WMO, όπου παρουσιάστηκαν οι μετρήσεις του στρώματος του όζοντος στα μέσα και τα μεγάλα γεωγραφικά πλάτη από τα φασματοφωτόμετρα τύπου Dobson και Brewer.

Στην τέταρτη ανακοίνωση παρουσιάστηκαν οι ατμοσφαιρικές συγκεντρώσεις του όζοντος (O_3) και του μονοξειδίου του άνθρακα (CO) στη Μεσσηνία, από τις μετρήσεις που πραγματοποιήθηκαν στον σταθμό ατμοσφαιρικής παρακολούθησης N.E.O. στη Μεθώνη κατά την περίοδο 2016-2010. Ο ρόλος του σταθμού, ο οποίος είναι μέρος της ερευνητικής υποδομής της ΠΑΝΑΚΕΙΑ, είναι να παρακολουθεί σε μακροχρόνια βάση τα επίπεδα βασικών σωματιδίων και αέριων ρύπων, σε μια προσπάθεια να ρίξει φως στους παράγοντες που ελέγχουν τα επίπεδα και τη μεταβλητότητά τους, και να διαχωρίσει τη σχετική συμβολή των τοπικών πηγών από πηγές περιφερειακής κλίμακας. Υπολογίστηκαν οι μέσες μηνιαίες τιμές για τη μελέτη του εποχιακού κύκλου των δύο ρύπων. Για να διερευνηθεί η περιφερειακή αντιπροσωπευτικότητα των μετρήσεων, ειδικά εντός των κλιματολογικά διαφορετικών τμημάτων του δυτικού και ανατολικού τμήματος της Ελλάδας, τα δεδομένα συγκρίθηκαν με

αντίστοιχες συγκεντρώσεις από τον σταθμό της Φινοκαλιάς στην Κρήτη. Οι συντελεστές συσχέτισης μεταξύ των μέσων ημερήσιων συγκεντρώσεων O₃ και CO στη Μεθώνη και τη Φινοκαλιά, είναι περίπου +0,5 και +0,6, αντίστοιχα. Δόθηκε έμφαση στους παράγοντες που καθορίζουν τη συμμεταβολή τους και στις περιόδους όπου τα επίπεδα διέφεραν σημαντικά.



The use of QBO, ENSO, and NAO perturbations in the evaluation of GOME-2 MetOp A total ozone measurements

Kostas Eleftheratos^{1,2}, Christos S. Zerefos^{2,3,4,5}, Dimitris S. Balis⁶, Maria-Elissavet Koukoulis⁶, John Kapsomenakis³, Diego G. Loyola⁷, Pieter Valks⁷, Melanie Coldewey-Egbers⁷, Christophe Lerot⁸, Stacey M. Frith⁹, Amund S. Haslerud¹⁰, Ivar S. A. Isaksen^{10,11,†}, and Seppo Hassinen¹²

¹Laboratory of Climatology and Atmospheric Environment, Faculty of Geology and Geoenvironment, National and Kapodistrian University of Athens, Athens, Greece

²Biomedical Research Foundation of the Academy of Athens, Athens, Greece

³Research Centre for Atmospheric Physics and Climatology, Academy of Athens, Athens, Greece

⁴Mariolopoulos-Kanaginis Foundation for the Environmental Sciences, Athens, Greece

⁵Navarino Environmental Observatory (N.E.O.), Messinia, Greece

⁶Laboratory of Atmospheric Physics, Department of Physics, Aristotle University of Thessaloniki, Thessaloniki, Greece

⁷Institut für Methodik der Fernerkundung (IMF), Deutsches Zentrum für Luft- und Raumfahrt (DLR), Oberpfaffenhofen, Germany

⁸Royal Belgian Institute for Space Aeronomy (BIRA), Brussels, Belgium

⁹Science Systems and Applications, Inc., Lanham, MD, USA

¹⁰Cicero Center for International Climate Research, Oslo, Norway

¹¹Department of Geosciences, University of Oslo, Oslo, Norway

¹²Finnish Meteorological Institute, Helsinki, Finland

†deceased

Correspondence: Kostas Eleftheratos (kelef@geol.uoa.gr)

Received: 16 June 2018 – Discussion started: 14 August 2018

Revised: 21 January 2019 – Accepted: 24 January 2019 – Published: 14 February 2019

Abstract. In this work we present evidence that quasi-cyclical perturbations in total ozone (quasi-biennial oscillation – QBO, El Niño–Southern Oscillation – ENSO, and North Atlantic Oscillation – NAO) can be used as independent proxies in evaluating Global Ozone Monitoring Experiment (GOME) 2 aboard MetOp A (GOME-2A) satellite total ozone data, using ground-based (GB) measurements, other satellite data, and chemical transport model calculations. The analysis is performed in the frame of the validation strategy on longer time scales within the European Organisation for the Exploitation of Meteorological Satellites (EUMETSAT) Satellite Application Facility on Atmospheric Composition Monitoring (AC SAF) project, covering the period 2007–2016. Comparison of GOME-2A total ozone with ground observations shows mean differences of about $-0.7 \pm 1.4\%$ in the tropics ($0\text{--}30^\circ$), about $+0.1 \pm 2.1\%$ in the mid-latitudes ($30\text{--}60^\circ$), and about $+2.5 \pm 3.2\%$ and

$0.0 \pm 4.3\%$ over the northern and southern high latitudes ($60\text{--}80^\circ$), respectively. In general, we find that GOME-2A total ozone data depict the QBO–ENSO–NAO natural fluctuations in concurrence with the co-located solar backscatter ultraviolet radiometer (SBUV), GOME-type Total Ozone Essential Climate Variable (GTO-ECV; composed of total ozone observations from GOME, SCIAMACHY – SCanning Imaging Absorption SpectroMeter for Atmospheric CHartography, GOME-2A, and OMI – ozone monitoring instrument, combined into one homogeneous time series), and ground-based observations. Total ozone from GOME-2A is well correlated with the QBO (highest correlation in the tropics of $+0.8$) in agreement with SBUV, GTO-ECV, and GB data which also give the highest correlation in the tropics. The differences between deseasonalized GOME-2A and GB total ozone in the tropics are within $\pm 1\%$. These differences were tested further as to their correlations with the QBO.

The differences had practically no QBO signal, providing an independent test of the stability of the long-term variability of the satellite data. Correlations between GOME-2A total ozone and the Southern Oscillation Index (SOI) were studied over the tropical Pacific Ocean after removing seasonal, QBO, and solar-cycle-related variability. Correlations between ozone and the SOI are on the order of $+0.5$, consistent with SBUV and GB observations. Differences between GOME-2A and GB measurements at the station of Samoa (American Samoa; 14.25° S, 170.6° W) are within $\pm 1.9\%$. We also studied the impact of the NAO on total ozone in the northern mid-latitudes in winter. We find very good agreement between GOME-2A and GB observations over Canada and Europe as to their NAO-related variability, with mean differences reaching the $\pm 1\%$ levels. The agreement and small differences which were found between the independently produced total ozone datasets as to the influence of the QBO, ENSO, and NAO show the importance of these climatological proxies as additional tool for monitoring the long-term stability of satellite-ground-truth biases.

1 Introduction

Ozone is an important gas of the Earth's atmosphere. In the stratosphere, ozone is considered *good ozone*, because it absorbs ultraviolet B radiation from the sun, thus protecting the biosphere from a large part of the sun's harmful radiation (e.g. Eleftheratos et al., 2012; Hegglin et al., 2015). In the lower atmosphere and near the surface, natural ozone has an equally important beneficial role, because it initiates the chemical removal of air pollutants from the atmosphere such as carbon monoxide, nitrogen oxides, and methane. Above natural levels, however, ozone is considered *bad ozone* because it can harm humans, plants, and animals. In addition, ozone is a greenhouse gas, warming the Earth's surface. In both the stratosphere and the troposphere, ozone absorbs infrared radiation emitted from Earth's surface, trapping heat in the atmosphere. As a result, increases or decreases in stratospheric or tropospheric ozone induce a climate forcing (Hegglin et al., 2015).

Ozone in the atmosphere can be measured by ground-based (GB) instruments, balloons, aircraft, and satellites and can be calculated by chemical transport model (CTM) simulations. Measurements by satellites from space provide ozone profiles and column amounts over nearly the entire globe on a daily basis (e.g. WMO, 2014). The three Global Ozone Monitoring Experiment 2 (GOME-2) instruments carried on MetOp platforms A, B, and C (GOME-2A, GOME-2B, and GOME-2C, respectively) serve this purpose. The first was launched on 19 October 2006, the second on 19 September 2012, and the last on 7 November 2018. The three GOME-2 instruments will provide unique long-term datasets of more than 15 years (2007–2024) related to atmospheric

composition and surface ultraviolet radiation using consistent retrieval techniques (Hassinen et al., 2016). The GOME-2 offline data are set to make a significant contribution towards climate and atmospheric research while providing near real-time data for use in weather forecasting and air quality forecasting applications (Hassinen et al., 2016).

Validation of satellite ozone measurements is performed with ground-based measurements as well as other satellite instruments (Hassinen et al., 2016). Validation of GOME-2A total ozone for the period 2007–2011 was performed by Loyola et al. (2011) and Koukouli et al. (2012). It was found that GOME-2 total ozone data agree at the $\pm 1\%$ level with GB measurements and other satellite datasets (Hassinen et al., 2016). The consistency between GOME-2A and GOME-2B total ozone columns, including a validation with GB measurements, was presented by Hao et al. (2014). An updated time series of the differences between GOME-2A and GOME-2B with GB observations can be found in Hassinen et al. (2016). The long-term stability of the two satellite instruments was also noted in that study. Both satellites are consistent over the Northern Hemisphere with negligible latitudinal dependence, while over the Southern Hemisphere there is a systematic difference of 1% between the two satellite instruments (Hassinen et al., 2016).

Chiou et al. (2014) compared zonal mean total column ozone inferred from three independent multi-year data records, namely solar backscatter ultraviolet radiometer (SBUV; v8.6) total ozone (McPeters et al., 2013), GOME-type Total Ozone Essential Climate Variable (GTO-ECV; Coldewey-Egbers et al., 2015; Garane et al., 2018), and GB total ozone for the period 1996–2011. Their analyses were conducted for the latitudinal zones of $0\text{--}30^{\circ}$ S, $0\text{--}30^{\circ}$ N, $50\text{--}30^{\circ}$ S, and $30\text{--}60^{\circ}$ N. It was found that, on average, the differences in monthly zonal mean total ozone vary between -0.3% and 0.8% and are well within 1% . In that study it was concluded that, despite the differences in the satellite sensors and retrievals methods, the SBUV v8.6 and GTO-ECV data records show very good agreement both in the monthly zonal mean total ozone and the monthly zonal mean anomalies between 60° S and 60° N. The GB zonal means showed larger scatter in the monthly mean data compared to satellite-based records, but the scatter was significantly reduced when seasonal zonal averages were analysed. The differences between SBUV and GB total ozone data presented in Chiou et al. (2014) are well in agreement with Labow et al. (2013), who systematically compared SBUV (v8.6) total ozone data with those measured by Brewer and Dobson instruments at various stations as a function of time, satellite solar zenith angle, and latitude. The comparisons showed good agreement (within $\pm 1\%$) over the past 40 years, with the very small bias approaching zero over the last decade. Comparisons with ozone sonde data showed good agreement in the integrated column up to 25 hPa, with differences not exceeding 5% (Labow et al., 2013).

The observed small biases (at the percentage level) between satellite and GB observations of total ozone, as have been documented in the above studies, ensure the provision of accurate satellite ozone measurements. The high accuracy and stability of the satellite instruments is essential for monitoring the expected recovery of the ozone layer resulting from measures adopted by the 1987 Montreal Protocol and its amendments (e.g. Zerefos et al., 2009; Loyola et al., 2011; Solomon et al., 2016; de Laat et al., 2017; Kuttippurath and Nair, 2017; Pazmiño et al., 2018; Stone et al., 2018; Strahan and Douglass, 2018). It is known that total ozone varies strongly with latitude and longitude as a result of chemical and transport processes in the atmosphere. Total ozone also varies with season. Seasonal variations are larger over mid-latitudes and high latitudes and are smaller in the tropics (e.g. WMO, 2014). On longer time scales total ozone variability is related to large-scale natural oscillations such as the quasi-biennial oscillation (QBO; e.g. Zerefos et al., 1983; Baldwin et al., 2001), the El Niño–Southern Oscillation (ENSO; e.g. Zerefos et al., 1992; Oman et al., 2013; Coldewey-Egbers et al., 2014), the North Atlantic Oscillation (NAO; e.g. Ossó et al., 2011; Chehade et al., 2014), and the 11-year solar cycle (e.g. Zerefos et al., 2001; Tourpali et al., 2007; Brönniman et al., 2013). Moreover, volcanic eruptions may also alter the thickness of the ozone layer (Zerefos et al., 1994; Frossard et al., 2013; Rieder et al., 2013; WMO, 2014). These natural perturbations affect the background atmosphere and consequently the distribution of the ozone layer. In this context, the study of the effect of known natural fluctuations in total ozone could serve as additional tool for evaluating the long-term variability of satellite total ozone data records.

The objective of the present work is to examine the ability of the GOME-2A total ozone data to capture the variability related to dynamical proxies of global and regional importance, such as the QBO, ENSO, and NAO, in comparison to GB measurements, other satellite data, and model calculations. The variability of total ozone from GOME-2A is compared with the variability of total ozone from the other examined datasets during these naturally occurring fluctuations in order to evaluate the ability of GOME-2A to depict natural perturbations. The analysis is performed in the frame of the validation strategy of GOME-2A data on longer time scales within the European Organisation for the Exploitation of Meteorological Satellites (EUMETSAT) Satellite Application Facility on Atmospheric Composition Monitoring (AC SAF) project. The evaluation of GOME-2A data performed here includes the study of monthly means of total ozone, the annual cycle of total ozone, the amplitude of the annual cycle (i.e. (maximum value – minimum value)/2), the relation with the QBO (correlation with zonal wind at the Equator at 30 hPa), the relation with ENSO (correlation with the Southern Oscillation Index – SOI), and the relation with the NAO (correlation with the NAO index in winter – DJF mean).

The annual cycle describes regular oscillations in total ozone that occur from month to month within a year. In general, month-to-month variations of total ozone are larger in the mid-latitudes and high latitudes than in the tropics. The QBO dominates the variability of the equatorial stratosphere (~ 16 – 50 km) and is easily seen as downward-propagating easterly and westerly wind regimes, with a variable period averaging approximately 28 months. Circulation changes induced by the QBO affect temperature and chemistry (Baldwin et al., 2001). The ENSO and NAO are naturally occurring patterns or modes of atmospheric and oceanic variability which orchestrate large variations in climate over large regions with profound impacts on ecosystems (Hurrell and Deser, 2009). We present the level of agreement between satellite-derived GOME-2A and GB total ozone in depicting natural oscillations like the QBO, ENSO, and NAO, highlighting the importance of these climatological proxies to be used as additional tools for monitoring the long-term stability of satellite–ground-truth biases.

2 Data sources

The analysis uses GOME-2 satellite total ozone columns for the period 2007–2016. This data forms part of the operational EUMETSAT AC SAF GOME-2 MetOp A GDP4.8 data product provided by the German Aerospace Center (DLR). The GOME-2 total ozone data have been averaged on a monthly $1^\circ \times 1^\circ$ latitude longitude grid. The overview of the GOME-2A satellite instrument and of the GOME-2 atmospheric data provided by AC SAF can be found in Hasinen et al. (2016).

To examine the natural variability of ozone on longer time scales, we have additionally analysed the Global Ozone Monitoring Experiment (GOME) aboard the second European Remote Sensing satellite (ERS-2), Scanning Imaging Absorption SpectroMeter for Atmospheric CHartography (SCIAMACHY) on Envisat, GOME-2A, and ozone monitoring instrument (OMI) on Aura merged prototype level-3 harmonized data record (GTO-ECV, $1^\circ \times 1^\circ$) data for the period 1995–2016 (Coldewey-Egbers et al., 2015; Garane et al., 2018). This GTO-ECV ozone data product was generated and provided by DLR as part of the European Space Agency Ozone Climate Change Initiative (ESA O3 CCI). The ESA O3 CCI merged level-3 record, which is based on GOME–SCIAMACHY–GOME-2A–OMI level-2 data, was obtained using the GODFIT v3.0 retrieval algorithm. More on ESA O3 CCI datasets can be found in the studies by Van Roozendael et al. (2012), Lerot et al. (2014), Koukouli et al. (2015), and Garane et al. (2018).

Both datasets are compared with a combined Total Ozone Mapping Spectrometer (TOMS), OMI, and Ozone Mapping Profiler Suite (OMPS) satellite total ozone dataset constructed using data from the TOMS on Nimbus 7 (1979–1993); TOMS on Meteor 3 (1991–1994); TOMS on Earth

Probe (1996–2005); the OMI aboard the NASA Earth Observing System (EOS) Aura satellite (2005–present); and data from the next-generation OMPS nadir profiler instrument, launched in October 2011 on the Suomi National Polar-orbiting Partnership (NPP) satellite (McPeters et al., 2015). The total ozone data are available at $1^\circ \times 1.25^\circ$ (TOMS) or $1^\circ \times 1^\circ$ (OMI–OMPS) resolution from <https://acd-ext.gsfc.nasa.gov/anonftp/toms/> (last access: 15 June 2018). From these data we constructed monthly mean total ozone data on a $5^\circ \times 5^\circ$ grid. To account for known biases between the instruments (e.g. Labow et al., 2013) we use the SBUV v8.6 merged ozone dataset (MOD) monthly zonal mean total ozone (https://acd-ext.gsfc.nasa.gov/Data_services/merged/index.html, also see next paragraph; last access: 15 June 2018) as a reference. We adjust each instrument such that the zonal mean in each 5° band averaged over the instrument lifetime matches the corresponding SBUV MOD zonal mean average. Thus the inherent longitudinal variability is retained from the TOMS–OMI–OMPS measurements, but any latitude-dependent bias between the instruments is removed. With the exception of the Meteor 3 TOMS in the Northern Hemisphere, all offsets were within 2% at low and mid-latitudes. Such a dataset should not be used for long-term trends but is sufficient for analysing periodic variability such as that for the QBO, ENSO, and NAO. We used data for the period 1995–2016. We note here that another long-term dataset which has been analysed for the QBO, ENSO, NAO and other perturbations comes from the multi-sensor reanalysis (MSR; Knibbe et al., 2014) but is not examined here.

In addition, we compare this with satellite SBUV station overpass data from 1995 to 2016. The satellite data are based on measurements from three SBUV-type instruments from April 1970 to the present (continuous data coverage from November 1978). Even though the time series includes different versions of the SBUV instrument, the basic measurement technique remains the same over the advancement of the instrument from the backscatter ultraviolet radiometer (BUV) to Solar Backscatter Ultraviolet Radiometer 2 (SBUV-2; Bhartia et al., 2013). Satellite overpass data over various ground-based stations are provided per day from <https://acd-ext.gsfc.nasa.gov/anonftp/toms/sbuv/MERGED/> (last access: 15 June 2018). These overpass data are analogous to the SBUV MOD monthly zonal mean data previously mentioned. Both are constructed by first filtering measurements of lesser quality and then averaging data from individual satellites when more than one instrument is operating. Monthly averages have been calculated by averaging the daily merged ozone overpass data for stations listed in Supplement Table S1. Details about the data are provided by MCPeters et al. (2013) and Frith et al. (2014).

We also compare this with GB observations of total ozone from a number of stations contributing to the World Ozone and Ultraviolet Radiation Data Centre (WOUDC). The WOUDC data centre is one of six world data centres which are part of the Global Atmosphere Watch programme of the

World Meteorological Organization (WMO). The WOUDC data centre is operated by the Meteorological Service of Canada, a branch of Environment Canada. In total, we analysed total ozone daily summaries from 193 ground-based stations operating Brewer, Dobson, filter, Système D'Analyse par Observations Zénithales (SAOZ), or Microtops instruments. The GB total ozone measurements are available from the website https://woudc.org/archive/Summaries/TotalOzone/Daily_Summary/ (last access: 15 June 2018). The various stations used in this study are listed in Table S1.

We have also analysed simulations of total ozone from the global 3-D CTM, the Oslo CTM3 (Søvde et al., 2012). The Oslo CTM3 has traditionally been driven by 3-hourly meteorological forecast data from the European Centre for Medium-Range Weather Forecasts (ECMWF) Integrated Forecast System (IFS) model, whereas in this study we apply the OpenIFS model (<https://software.ecmwf.int/wiki/display/OIFS/>; last access: 15 June 2018), cycle 38r1, which is an improvement from Søvde et al. (2012). Details on the model are given in Søvde et al. (2012). The Oslo CTM3 comprises both detailed tropospheric and stratospheric chemistry. Photochemistry is calculated using Fast-JX version 6.7c (Prather, 2015) and chemical kinetics from the Jet Propulsion Laboratory (JPL) 2011 (Sander et al., 2011). Total ozone columns compare well with measurements and other model studies (Søvde et al., 2012 and references therein). The horizontal resolution of the model is $2.25^\circ \times 2.25^\circ$. We used the global monthly mean total ozone columns for the period 1995–2016.

To examine the QBO component of total ozone we made use of the monthly mean zonal winds in Singapore at 30 hPa. The zonal wind data at 30 hPa were provided by the Freie Universität Berlin (FU-Berlin) at <https://www.geo.fu-berlin.de/met/ag/strat/produkte/qbo/qbo.dat> (last access: 15 June 2018; Naujokat, 1986). The impact of ENSO in the tropics was investigated by using the SOI from the Bureau of Meteorology of the Australian Government (<http://www.bom.gov.au/climate/current/soi2.shtml>; last access: 15 June 2018). The correlation between total ozone and the NAO index was mainly computed for the winter mean (DJF) when the NAO amplitude is large (e.g. Hurrell and Deser, 2009), but it is also addressed in other seasons. Emphasis is placed on Canada, Europe, and the North Atlantic Ocean in winter. The NAO index (DJF) based on the principal component (PC) provided by the Climate Analysis Section of NCAR in Boulder, CO, USA (available at: <https://climatedataguide.ucar.edu/climate-data/hurrell-north-atlantic-oscillation-nao-index-pc-based>; last access: 15 June 2018), was used. Total ozone variability is also related to dynamical variability, for example, variability in tropopause height (e.g. Dameris et al., 1995; Hoinka et al., 1996; Steinbrecht et al., 1998). The impact of tropopause height variations on total ozone variability was examined by analysing the tropopause pressure from the independently produced NCEP/NCAR (National Centers for Environ-

mental Prediction – National Center for Atmospheric Research) Reanalysis 1 dataset computed on a 2.5° grid. The NCEP/NCAR reanalysis data were provided from the website at <https://www.esrl.noaa.gov/psd/data/gridded/data.ncep.reanalysis.tropopause.html> (last access: 15 June 2018; Kalnay et al., 1996).

3 Results and discussion

3.1 Monthly zonal means and annual cycle

Figure 1 compares monthly mean total ozone from GOME-2A and SBUV (v8.6) satellite overpass data for stations shown in Table S1. The GOME-2A data were taken at a spatial resolution of $1^\circ \times 1^\circ$ around each of the ground-based monitoring stations listed in Table S1 and then averaged over the tropics, mid-latitudes, and high latitudes of both hemispheres in 30° latitudinal zones to provide the large-scale monthly zonal means for the GOME-2A data. Accordingly, SBUV satellite overpass data were averaged over each geographical zone to provide the large-scale zonal means for the SBUV observations. Mean differences and standard deviations between GOME-2A and SBUV total ozone were found to be $+0.1 \pm 0.7\%$ in the tropics ($0\text{--}30^\circ$), about $+0.8 \pm 1.6\%$ in the mid-latitudes ($30\text{--}60^\circ$), about $+1.3 \pm 2.2\%$ over the northern high latitudes ($60\text{--}80^\circ\text{N}$), and about $-0.5 \pm 2.9\%$ over the southern high latitudes ($60\text{--}80^\circ\text{S}$). The differences were estimated as $(\text{GOME-2A} - \text{SBUV})/\text{SBUV} (\%)$ from January 2007 to December 2016. Small differences were also found between GOME-2A and GB measurements (Fig. 2 and Table 1), and here GB station data were averaged over each geographical zone to provide the large-scale zonal means for the GB measurements. Mean differences and standard deviations between GOME-2A and GB total ozone were found to be $-0.7 \pm 1.4\%$ in the tropics ($0\text{--}30^\circ$), $+0.1 \pm 2.1\%$ in the mid-latitudes ($30\text{--}60^\circ$), $+2.5 \pm 3.2\%$ over the northern high latitudes ($60\text{--}80^\circ\text{N}$), and $0.0 \pm 4.3\%$ over the southern high latitudes ($60\text{--}80^\circ\text{S}$). Recall that all estimates refer to the period between January 2007 and December 2016.

In summary, the largest differences between GOME-2A, SBUV (v8.6), and GB measurements are found over the northern high latitudes ($60\text{--}80^\circ\text{N}$), and the highest variability (standard deviation of the mean difference) is observed over the latitude belt ($60\text{--}80^\circ\text{S}$). In addition, these differences (especially at the high latitudes) can be affected by the fact that the same days have not always been used for the construction of the monthly mean values for the different datasets. In the tropics and mid-latitudes the respective differences are within $\pm 1\%$ or less, in line with Chiou et al. (2014). Validation results were also presented by Loyola et al. (2011), Koukouli et al. (2012), Coldewey-Egbers et al. (2015), and Koukouli et al. (2015), and updates of which are included in Hassinen et al. (2016). Our results based on data updated to 2017 largely confirm those studies, pointing

to the good performance of GOME-2A when extending the period of record.

Next, we studied the correlation between total ozone from GOME-2A and SBUV satellite data using linear regression analysis for the period 2007–2016. The statistical significance of the correlation coefficients, R , was calculated using the t -test formula for R with $N - 2$ degrees of freedom, as used in Zerefos et al. (2018). The regression model showed statistically significant correlations between the different datasets as follows: $R = +0.99$ in the tropics, mid-latitudes, and the northern high latitudes and $R = +0.97$ in the southern high latitudes. All correlation coefficients are highly statically significant (99.9 % confidence level). In the long term, statistically significant correlation coefficients ($R \geq +0.94$) are also found between GOME-2A satellite and GB measurements (Fig. 2), despite the different type of instruments used to measure total ozone from the ground. The regression parameters for the correlation coefficients shown in Figs. 1 and 2 are provided in Table 2.

A large part of the strong correlations shown in Figs. 1 and 2 is attributable to the seasonal variability of total ozone which is presented in Fig. 3 for GOME-2A, SBUV, and GB data. More specifically, Fig. 3 shows the seasonal variations of total ozone from station data, averaged from zones per 10° latitude, north and south. At high latitudes our analysis stops at 80° . There is a very good agreement between the annual cycles of total ozone from the three datasets denoting the consistency of the satellite retrievals with GB observations. Similar annual cycles are also found with the GTO-ECV ozone data (not shown). Similar consistency is also revealed for the amplitudes of the annual cycles, computed as $(\text{maximum value} - \text{minimum value})/2$ in Dobson units (DU). Figure 4 shows global maps of the amplitude of the annual cycle of total ozone for the period 2007–2016 from GOME-2A (panel a), GTO-ECV (panel b), and the TOMS–OMI–OMPS (panel c) satellite data. All maps are plotted against the sine of the latitude north and south in order to show areas according to their actual size. As can be seen from Fig. 4, the amplitude of the annual cycle is less than 20 DU in the tropics, increasing as we move towards the mid-latitudes and high latitudes to up to 75 DU. Interestingly, there is a region with small amplitude of the annual cycle in the southern mid-latitudes with values of about 10–15 DU, seen in Fig. 4 as a blue curved line crossing the longitudes around 60°S , which points to small seasonal variations of total ozone in these parts. The seasonal increase in Antarctic ozone is delayed by 2–3 months compared to the northern polar region. Only with the breakdown of the polar vortex in late spring, i.e. at a time when the poleward transport over lower latitudes has already ceased, does a strong ozone influx occur in the Antarctic. With this delay the amplitude of the seasonal variation stays much smaller poleward of $55\text{--}60^\circ$ in the south than in the north (Dütsch, 1974). These features are consistent between all examined satellite datasets and are reproduced to a large extent by the Oslo CTM3 model as well, except in the south-

Table 1. Mean differences and their standard deviations in percent between total ozone from GOME-2A, SBUV (v8.6) satellite overpass data, and ground-based observations over different latitude zones, as shown in Figs. 1 and 2.

	(GOME-2A – SBUV)/SBUV (%) Station mean data	(GOME-2A – GROUND)/GROUND (%) Station mean data
60–80° N	+1.3 ± 2.2	+2.5 ± 3.2
30–60° N	+0.8 ± 1.6	+0.1 ± 1.9
0–30° N	0.0 ± 0.7	–0.5 ± 1.2
0–30° S	+0.1 ± 0.7	–0.9 ± 1.6
30–60° S	+0.9 ± 1.6	0.0 ± 2.4
60–80° S	–0.5 ± 2.9	0.0 ± 4.3

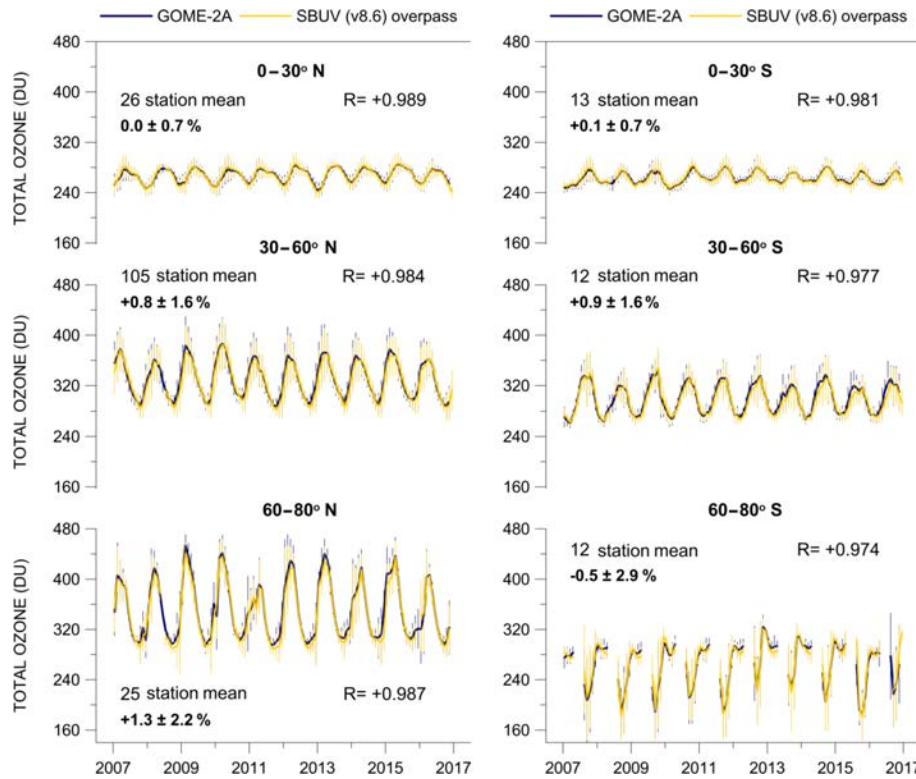


Figure 1. Monthly mean total ozone from GOME-2A compared with monthly mean total ozone from SBUV (v8.6) satellite overpass data for the period 2007–2016 over the Northern and the Southern Hemisphere, based on station mean data. R is the correlation coefficient between the two lines. Error bars show the standard deviation of each monthly mean. Mean differences $\pm\sigma$ are given as (GOME-2A – SBUV)/SBUV (%).

ern mid-latitudes, where the model seems to underestimate the observed annual cycle (Fig. 4, panel d).

In summary, we find a similar pattern and amplitude of the annual cycle between total ozone from GOME-2A and the other examined total ozone datasets. The mean differences in the annual cycles of GOME-2A and SBUV satellite data are small in the tropics ($0\text{--}30^\circ$: 0.3 ± 2.4 DU) and increase as we move towards the mid-latitudes ($30\text{--}60^\circ$: 2.4 ± 4.4 DU) and higher latitudes ($60\text{--}80^\circ$: 1.7 ± 4.8 DU). These numbers are consistent with the ones found between GOME-2A and GB measurements (tropics: 1.1 ± 2.3 DU; mid-latitudes: 1.2 ± 5.1 DU; high latitudes: 5.1 ± 7.1 DU). In all latitude

zones the correlation coefficients between the annual cycles of GOME-2A–SBUV and GOME-2A–GB data pairs were found to be greater than 0.9.

Before examining correlations with the large-scale natural fluctuations QBO, ENSO, and NAO, the mean annual cycle has been removed from the ozone datasets as described in the next section.

3.2 Correlation with QBO

We then studied how changes in dynamics affect the ozone columns in the atmosphere. The time series obtained have

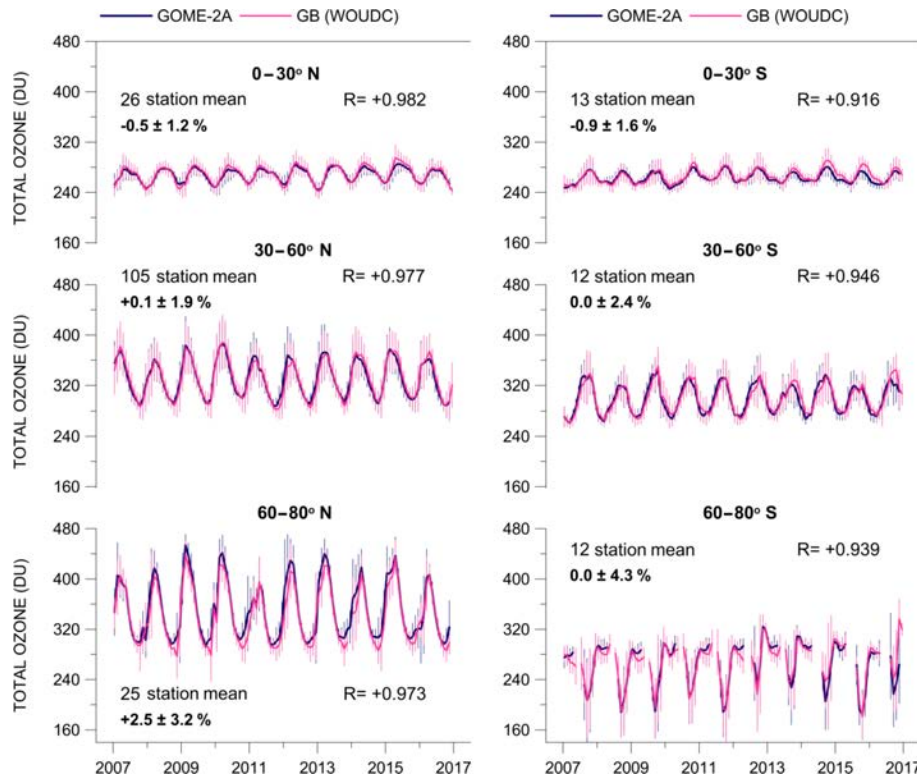


Figure 2. Same as in Fig. 1, but for GOME-2A and GB observations. *R* is the correlation coefficient between the two lines. Error bars show the standard deviation of each monthly mean. Mean differences $\pm\sigma$ are given as (GOME-2A – GROUND)/GROUND (%).

Table 2. Statistics of the correlations shown in Figs. 1 and 2 between total ozone from (a) GOME-2A data and SBUV (v8.6) overpass data and (b) GOME-2A data and ground-based measurements.

(a) GOME-2A and SBUV (v8.6)	Correlation	Intercept (DU)	Slope*	Error	<i>t</i> value	<i>p</i> value	<i>N</i>
60–80° N	+0.987	4.925	0.999	0.015	65.224	<0.0001	117
30–60° N	+0.984	5.002	0.993	0.017	59.784	<0.0001	118
0–30° N	+0.989	28.304	0.894	0.012	72.404	<0.0001	118
0–30° S	+0.981	21.575	0.919	0.017	53.874	<0.0001	118
30–60° S	+0.977	–4.198	1.023	0.021	49.123	<0.0001	118
60–80° S	+0.974	2.944	0.984	0.025	39.985	<0.0001	88
(b) GOME-2A and ground-based	Correlation	Intercept (DU)	Slope*	Error	<i>t</i> value	<i>p</i> value	<i>N</i>
60–80° N	+0.973	7.651	1.002	0.022	45.155	<0.0001	118
30–60° N	+0.977	15.772	0.952	0.019	49.671	<0.0001	119
0–30° N	+0.982	49.534	0.810	0.014	56.951	<0.0001	119
0–30° S	+0.916	56.520	0.778	0.032	24.655	<0.0001	119
30–60° S	+0.946	12.423	0.958	0.030	31.612	<0.0001	119
60–80° S	+0.939	0.405	0.999	0.039	25.439	<0.0001	89

* Error, *t* value, and *p* value refer to slope.

been deseasonalized by subtracting the long-term monthly mean from each individual monthly mean value. Ozone column variations for different latitude zones in the Northern and Southern Hemispheres have been compared. Figure 5 compares total ozone deseasonalized anomalies (in % of the mean) from GOME-2A and SBUV satellite retrievals in

the tropics (10° N–10° S), subtropics (10°–30° N and 10°–30° S), and mid-latitudes (30°–60° N and 30°–60° S). The right panel of Fig. 5 shows the respective anomalies from GTO-ECV data. Mean differences between GOME-2A and SBUV deseasonalized monthly zonal means between 60° N and 60° S are less than $\pm 0.5\%$.

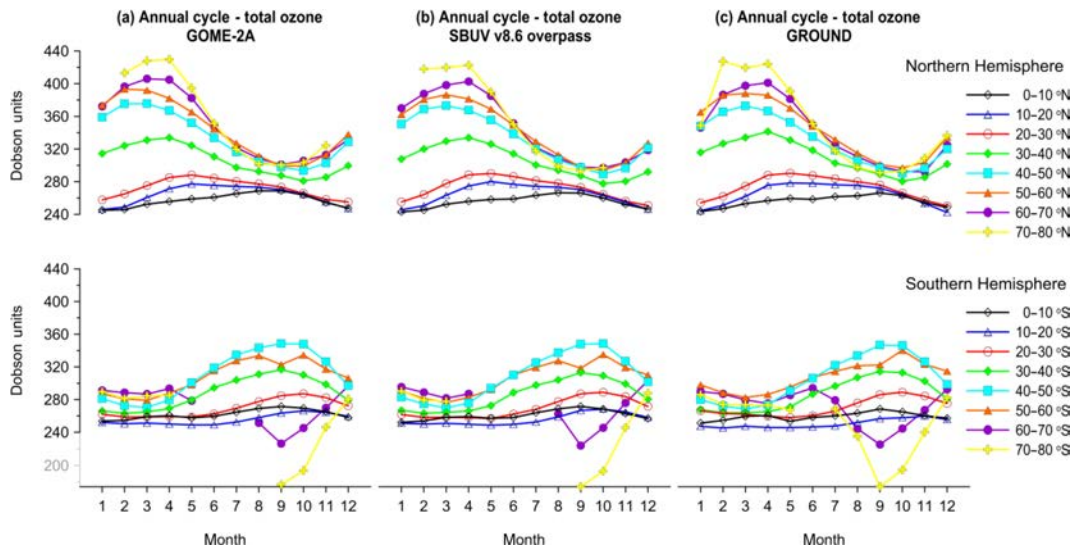


Figure 3. Comparison of the annual cycle of total ozone from GOME-2A with that from SBUV (v8.6) satellite overpass data and GB observations in the period 2007–2016 based on station data averaged per 10° latitude zones. The annual cycle is distorted above 60° S due to the Antarctic ozone hole.

The dotted line superimposed on the ozone anomalies in Fig. 5 shows the equatorial zonal winds at 30 hPa, which were used as a proxy index to study the impact of QBO on total ozone. The general features include a QBO signal in total ozone at latitudes between 10° N and 10° S, which almost matches with the phase of QBO in the zonal winds. At higher northern and southern latitudes there is a phase shift in the QBO impact on total ozone. The impact of QBO is most pronounced in the tropics and is less pronounced in the subtropics and mid-latitudes. Strong positive correlations with the QBO are found in the tropics (correlation between GOME-2A and the QBO is about $+0.77$, t test = 12.91) and weaker (usually of the opposite sign), less significant correlations are found at higher latitudes (about -0.15 in the northern extratropics and about -0.45 in the southern extratropics). Similar correlation patterns with the QBO are found for the GTO-ECV, SBUV, and GB data. These correlations suggest that the variability that can be attributed to the QBO in the tropics is about 60 % and is about 2 % and 20 % in the northern and the southern extratropics, respectively.

Table 3 summarizes the correlation and regression coefficients between total ozone and the QBO at 30 hPa for the different latitude zones and the different datasets. For latitudes between 10° N and 10° S correlations between total ozone from GOME-2A, GTO-ECV, SBUV, GB data, and the QBO are all positive. At latitudes between 10 and 30° the correlations turn to negative, in agreement with the results of Knibbe et al. (2014), who noted that when moving from the tropics towards higher latitudes, the regression estimates switch to negative values at approximately 10° N and 10° S. The correlations with the QBO at 30 hPa remain negative up to 60° , a consistent result among all our datasets and something also

reported by Knibbe et al. (2014) with the MSR ozone data. The correlation and regression coefficients between GOME-2A and the QBO are fairly similar to those found between SBUV and the QBO, as well as among all datasets as seen in Table 3, despite the different periods of records.

These features are also evident in Fig. 6, which compares GOME-2A (and GTO-ECV) satellite total ozone with GB observations with respect to the QBO. Mean differences and standard deviations between GOME-2A and GB and between GTO-ECV and GB deseasonalized total ozone data do not exceed 1 %. Again, correlation coefficients between deseasonalized GOME-2A and deseasonalized GB data are highly significant in all latitude zones ($30\text{--}60^\circ$ N, $+0.91$: slope = 0.818, error = 0.035, t value = 23.466, and $N = 119$; $10\text{--}30^\circ$ N, $+0.91$: slope = 0.786, error = 0.033, t value = 23.529, and $N = 119$; 10° N– 10° S, $+0.94$: slope = 0.973, error = 0.034, t value = 28.449, and $N = 109$; $10\text{--}30^\circ$ S, $+0.87$: slope = 0.864, error = 0.044, t value = 19.659, and $N = 119$; $30\text{--}60^\circ$ S, $+0.88$: slope = 0.858, error = 0.043, t value = 19.854, and $N = 119$). The same is true for the correlations between GTO-ECV and GB data pairs ($30\text{--}60^\circ$ N, $+0.94$; $10\text{--}30^\circ$ N, $+0.89$; 10° N– 10° S, $+0.94$; $10\text{--}30^\circ$ S, $+0.87$; $30\text{--}60^\circ$ S, $+0.85$). Our results are in line with Eleftheratos et al. (2013) and Isaksen et al. (2014), who compared QBO-related ozone column variations from the chemical transport model Oslo CTM2 with SBUV satellite data for shorter time periods. In summary, it has been shown that GOME-2A depicts the significant effects of QBO on stratospheric ozone in concurrence with SBUV and GB measurements. The instrument captures the variability of ozone in the tropics and the mid-latitudes correctly, which is nearly in phase with the QBO in the trop-

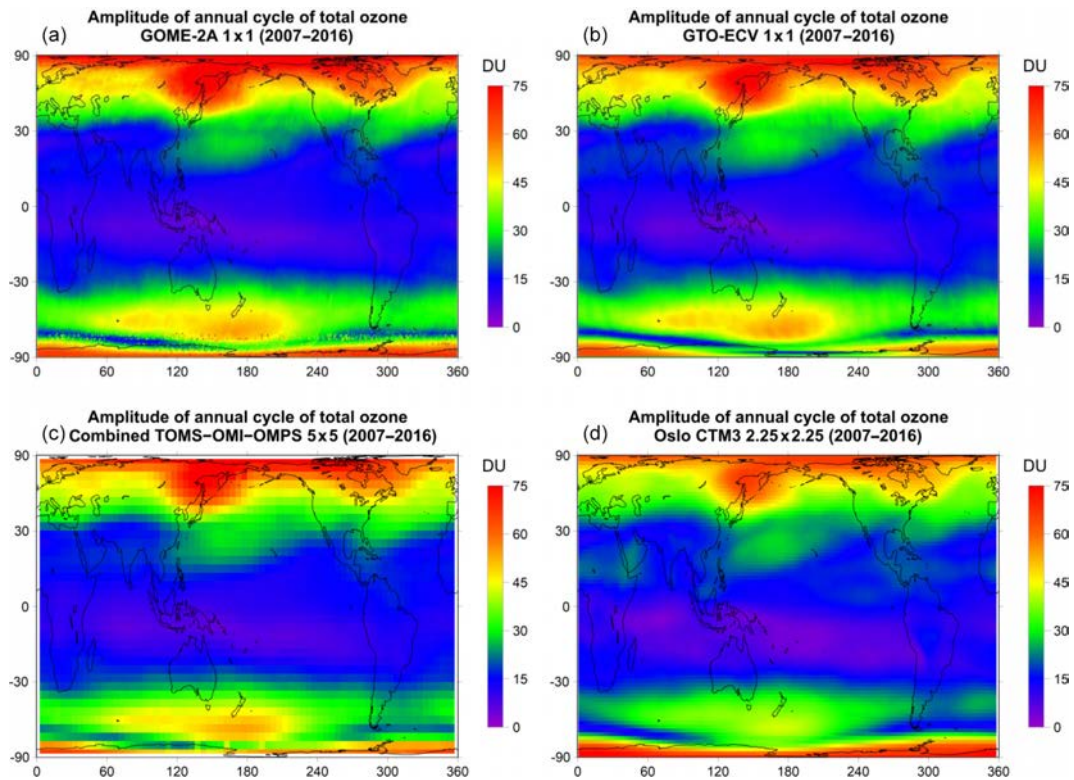


Figure 4. Comparison of the amplitude, i.e. (maximum value – minimum value)/2, of the annual cycle of total ozone from GOME-2A (a) with the amplitude of the annual cycle of total ozone from GTO-ECV (b), the combined TOMS–OMI–OMPS satellite data (c), and Oslo CTM3 model simulations (d).

ics and out of phase in the northern and the southern mid-latitudes, as has been shown by earlier studies (e.g. Zerefos, 1983; Baldwin et al., 2001).

3.3 Correlation with ENSO

Apart from the QBO, which affects the variability of total ozone in the tropics, an important mode of natural climate variability in the tropics is the ENSO. To examine the impact of the ENSO on total ozone in the tropics we first removed variability related to the QBO and the solar cycle and then performed the correlation analysis with the SOI. The effect of the QBO was removed from the time series by using a linear regression model for the total ozone variations at each grid box, of the form

$$D(t) = a_0 + a_1 \times \text{QBO}(t) + \text{residuals}(t); 0 < t \leq T, \quad (1)$$

where $D(t)$ is the monthly deseasonalized total ozone and t is the time in months, with $t = 0$ corresponding to the initial month and $t = T$ corresponding to the last month. The term a_0 is the intercept of the statistical model. To model the QBO we made use of the equatorial zonal winds at 30 hPa. The term a_1 is the regression coefficient of the QBO. The QBO component was removed from the time series by using a phase lag with a maximum correlation of 28 months

(month lag -14 to month lag 13). The QBO-related coefficients α_0 and α_1 of Eq. (1) for the deseasonalized GOME-2A, GTO-ECV, TOMS–OMI–OMPS, and Oslo CTM3 zonal mean data are presented in Table 3. Additional information for the regression coefficients α_1 of QBO is provided in the Supplement Fig. S1, which shows the spatial distribution of the regression coefficients in latitude–longitude maps.

The residuals from Eq. (1) were then inserted in a second regression (Eq. 2) to account for the effect of the solar cycle on total ozone, as follows:

$$\text{O}_3(t) = \beta_0 + \beta_1 \times F_{10.7}(t) + \text{residuals}(t); 0 < t \leq T, \quad (2)$$

where β_0 and β_1 are now the intercept and regression coefficients of the solar cycle, respectively. To model the solar cycle we used the 10.7 cm wavelength solar radio flux ($F_{10.7}$) as a proxy, taken from the National Research Council and Natural Resources Canada at ftp://ftp.geolab.nrcan.gc.ca/data/solar_flux/monthly_averages/solflux_monthly_average.txt (last access: 12 December 2018). We use the absolute solar fluxes, which are adjusted to account for variations in Earth–Sun distance and uncertainty in antenna gain and waves reflected from the ground. Latitude–longitude maps of the regression coefficients β_1 of the solar cycle are presented in the Fig. S2. We note that the global pattern of the regression coefficients

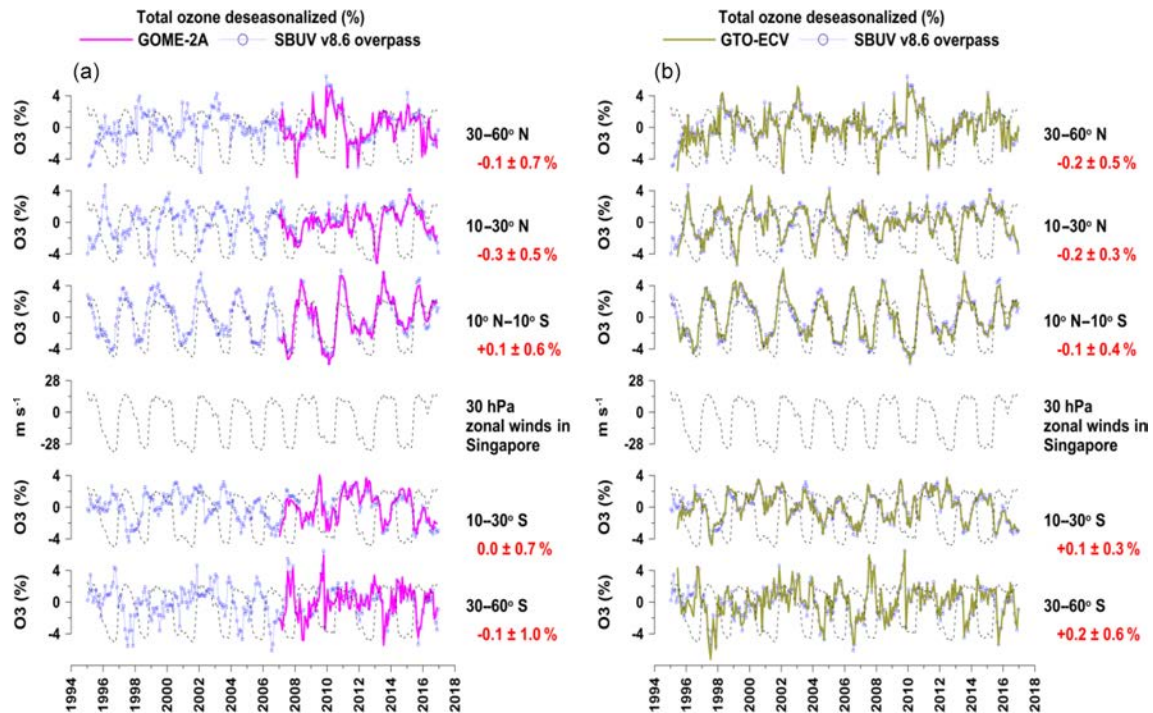


Figure 5. (a) Time series of deseasonalized total ozone from GOME-2A and SBUV (v8.6) satellite overpasses over different latitude zones, along with the equatorial zonal winds at 30 hPa as an index of the QBO; (b) same as in (a), but for GTO-ECV and SBUV. Values with red colour refer to the mean differences $\pm\sigma$ (in %) between GOME-2A and SBUV deseasonalized data averaged over various WOUDC stations (150 stations in the northern mid-latitudes – 30–60° N; 21 stations in the northern subtropics – 10–30° N; eight stations in the tropics – 10° S–10° N; 10 stations in southern subtropics – 10–30° S; and 12 stations in the southern mid-latitudes – 30–60° S). The QBO proxy is superimposed on the ozone anomalies.

of the solar cycle from GOME-2A data matches well with what has been shown by Knibbe et al. (2014) with the re-analysis MSR data.

The remainders from Eq. (2) were used in a third regression (Eq. 3) to study the correlations between total ozone and SOI at each individual grid box:

$$O_3(t) = c_0 + c_1 \times SOI(t) + \text{residuals}(t); 0 < t \leq T, \quad (3)$$

where c_0 and c_1 are now the intercept and regression coefficients of ENSO, respectively. Estimates of the regression coefficients c_1 are shown in the Fig. S3.

Figure 7 presents the correlations between the SOI and total ozone from GOME-2A (panel a), GTO-ECV (panel b), and TOMS–OMI–OMPS satellite data (panel c) as well as between the SOI and the Oslo model simulations (panel d). All four plots refer to the period 2007–2016. As can be seen from Fig. 7a, correlations of >0.3 between GOME-2A total ozone and the SOI are found in the tropical Pacific Ocean at latitudes between 25° N and 25° S. These correlations were tested as to their statistical significance in the period 2007–2016, using the t test for R with $N - 2$ degrees of freedom (as in Zerefos et al., 2018), and were found to be statistically significant. A similar picture of correlation coefficients is also observed by the GTO-ECV and TOMS–OMI–OMPS

data. Both datasets show similar results as to the range of correlations (>0.3) in the tropical Pacific for the common period of observations. Nevertheless, the spatial resolution is higher in the GOME-2A and GTO-ECV ($1 \times 1^\circ$) data than in the TOMS–OMI–OMPS ($5 \times 5^\circ$) data, so the former datasets perform better when looking at smaller space scales. We have to note here that in both maps there are larger areas with correlation coefficients >0.3 in the southern part of the tropics than in the northern part. However, this was mostly observed during the period 2007–2016. By examining the longer-term data record of the TOMS–OMI–OMPS data, which extends back to 1979, we find symmetry in the pattern of correlations north and south of the Equator in the tropical Pacific Ocean (Fig. A1 of Appendix A), which indicates that both sides of the tropical Pacific are affected more or less in a similar way by El Niño–La Niña events. Finally, the Oslo CTM3 gives small correlations (<0.3) in the tropical Pacific Ocean around the Equator, except over the northern and southern subtropics where the model compares better with the observations.

The small rectangle in Fig. 7 corresponds to the southern Pacific region (10–20° S, 180–220° E), and the blue cross corresponds to the Samoa station (American Samoa; 14.25° S, 189.4° E), where total ozone has been studied with respect to the impact of ENSO after removing the variabil-

Table 3. Statistics of correlations between deseasonalized total ozone and the QBO at 30 hPa for (a) GOME-2A data, (b) GTO-ECV data, (c) SBUV (v8.6) overpass data, and (d) ground-based measurements.

(a) GOME-2A and QBO	Correlation	Intercept (%)	Slope*	Error	<i>t</i> value	<i>p</i> value	<i>N</i>
30–60° N	–0.073	–0.045	–0.008	0.010	–0.791	0.4307	119
10–30° N	–0.099	–0.048	–0.008	0.008	–1.077	0.2835	119
10° N–10° S	+0.767	0.654	0.114	0.009	12.910	<0.0001	119
10–30° S	–0.472	–0.273	–0.048	0.008	–5.799	<0.0001	119
30–60° S	–0.424	–0.262	–0.046	0.009	–5.063	<0.0001	119
(b) GTO-ECV and QBO	Correlation	Intercept (%)	Slope*	Error	<i>t</i> value	<i>p</i> value	<i>N</i>
30–60° N	–0.116	–0.090	–0.012	0.007	–1.869	0.0628	259
10–30° N	–0.142	–0.100	–0.014	0.006	–2.293	0.0226	259
10° N–10° S	+0.779	0.705	0.109	0.005	19.949	<0.0001	259
10–30° S	–0.484	–0.306	–0.046	0.005	–8.873	<0.0001	259
30–60° S	–0.417	–0.312	–0.048	0.007	–7.345	<0.0001	259
(c) SBUV (v8.6) and QBO	Correlation	Intercept (%)	Slope*	Error	<i>t</i> value	<i>p</i> value	<i>N</i>
30–60° N	–0.165	–0.112	–0.018	0.007	–2.694	0.0075	262
10–30° N	–0.177	–0.114	–0.018	0.006	–2.901	0.0040	263
10° N–10° S	+0.748	0.648	0.104	0.006	18.223	<0.0001	263
10–30° S	–0.488	–0.287	–0.046	0.005	–9.037	<0.0001	263
30–60° S	–0.458	–0.328	–0.051	0.006	–8.333	<0.0001	263
(d) Ground-based and QBO	Correlation	Intercept (%)	Slope*	Error	<i>t</i> value	<i>p</i> value	<i>N</i>
30–60° N	–0.158	–0.123	–0.017	0.007	–2.594	0.0100	264
10–30° N	–0.142	–0.083	–0.016	0.007	–2.317	0.0213	264
10° N–10° S	+0.695	0.553	0.095	0.006	15.327	<0.0001	253
10–30° S	–0.490	–0.268	–0.046	0.005	–9.091	<0.0001	264
30–60° S	–0.431	–0.322	–0.048	0.006	–7.734	<0.0001	264

* The slope is in % per unit change of the explanatory variable. Error, *t* value, and *p* value refer to slope.

Table 4. Annual mean total ozone, amplitude of annual cycle, amplitude of QBO, amplitude of solar cycle, and amplitude of ENSO in the period 1995–2016 from GOME-2A, GTO-ECV, the combined TOMS–OMI–OMPS satellite data, and Oslo CTM3 model calculations over the southern Pacific region (10–20° S, 180–220° E) and at the Samoa station (14.25° S, 189.4° E), located within this region.

	Southern Pacific Ocean				Samoa station			
	GOME-2A*	GTO-ECV	TOMS–OMI–OMPS	Oslo CTM3	GOME-2A*	GTO-ECV	GROUND	SBUV (v8.6)
Annual mean	255.3 DU	254.7 DU	253.0 DU	259.5 DU	252.7 DU	252.2 DU	249.2 DU	251.9 DU
Amplitude of annual cycle	7.4 DU (2.9 %)	7.7 DU (3.0 %)	7.3 DU (2.9 %)	5.2 DU (2.0 %)	7.1 DU (2.8 %)	6.7 DU (2.7 %)	6.7 DU (2.7 %)	7.3 DU (2.9 %)
Amplitude of QBO	2.7 DU (1.0 %)	2.2 DU (0.9 %)	2.4 DU (0.9 %)	2.3 DU (0.9 %)	3.0 DU (1.2 %)	2.2 DU (0.9 %)	2.7 DU (1.1 %)	2.0 DU (0.8 %)
Amplitude of solar cycle	2.1 DU (0.8 %)	4.1 DU (1.6 %)	4.6 DU (1.8 %)	1.8 DU (0.7 %)	2.0 DU (0.8 %)	4.5 DU (1.8 %)	1.6 DU (0.6 %)	4.5 DU (1.8 %)
Amplitude of ENSO	6.2 DU (2.4 %)	8.8 DU (3.5 %)	6.0 DU (2.4 %)	8.8 DU (3.4 %)	5.6 DU (2.2 %)	7.7 DU (3.0 %)	5.5 DU (2.2 %)	7.5 DU (3.0 %)

* Period 2007–2016.

ity related to the annual cycle, QBO, and the solar cycle. Figure 8 shows an example of the ENSO impact on total ozone in the southern Pacific Ocean. Figure 8a shows the time series of total ozone anomalies from GOME-2A, GTO-ECV, and TOMS–OMI–OMPS satellite data together with the SOI. Comparisons of GOME-2A data with GTO-ECV data, SBUV overpass data, and GB measurements at the

Samoa station are shown in Fig. 8b. The dotted line shows the respective tropopause pressure anomalies from the NCEP reanalysis. All datasets point to the strong influence of ENSO on total ozone. Most evident is the strong decrease of about 4 % in 1997–1998, which was caused by the strongest El Niño event in the examined period. A strong decrease is also observed in the tropopause pressures by NCEP. Also no-

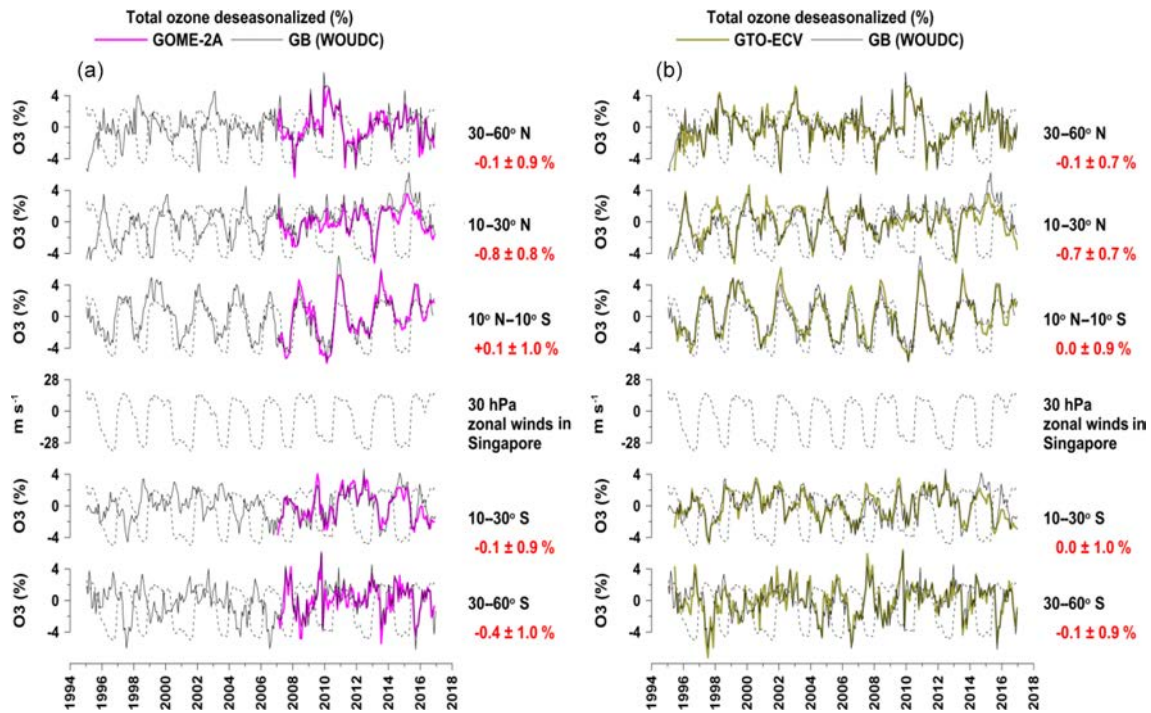


Figure 6. Same as in Fig. 5, but for GOME-2A and GB observations (a) and for GTO-ECV and GB observations (b). The QBO proxy is superimposed on the ozone anomalies.

table is the strong La Niña event in 2010 which caused total ozone to increase by about 4%. We calculate a strong correlation between total ozone from GTO-ECV and the SOI of $+0.66$ (99% confidence level), which accounts for about 40% of the variability of total ozone over the tropical Pacific Ocean when the annual cycle, QBO signal, and solar cycle are removed. From the regression with SOI we estimated an ENSO-related term from which we calculated the amplitude of ENSO in total ozone as (maximum ozone – minimum ozone)/2. The amplitude of ENSO in total ozone was estimated to be 8.8 DU, or 3.5% of the annual mean. This is comparable to the amplitude of the annual cycle (7.7 DU, or 3.0% of the mean) and is larger than the amplitude of QBO (2.2 DU or 0.8% of the mean) and the amplitude of the solar cycle in this region (4.1 DU, or 1.6% of the mean). These results are based on the GTO-ECV total ozone data. Similar results were also found at the Samoa station from GB observations (i.e. correlation with SOI: $+0.55$; amplitude of ENSO: 7.7 DU, or 3.0% of the mean; amplitude of the annual cycle: 6.7 DU, or 2.7% of the mean). Statistics of total ozone such as mean, amplitude of the annual cycle, amplitude of the QBO, amplitude of the solar cycle, and amplitude of the ENSO in total ozone over the selected areas are presented in Table 4. Satellite, GB, and model data show consistent results. It also appears that the Samoa station represents the greater area in the southern Pacific well as to the impact of the ENSO.

Differences between GOME-2A and its data pairs in the southern Pacific Ocean are of the order of $-0.2 \pm 1.0\%$ between GOME-2A and TOMS–OMI–OMPS data, $-0.3 \pm 0.9\%$ between GOME-2A and GTO-ECV, and $-0.9 \pm 1.8\%$ between GOME-2A and Oslo CTM3. Accordingly, differences in Samoa are $-0.6 \pm 1.9\%$ between GOME-2A and GB data, $0.0 \pm 1.4\%$ between GOME-2A and GTO-ECV, and $-0.1 \pm 1.3\%$ between GOME-2A and SBUV. Despite the small differences found, we note here that GOME-2A values in the last 4 years of Figs. 8 and 9 slightly deviate from the other datasets and correlate weaker with the SOI than the other years in the time series. For instance, we estimate a drop in the correlation coefficient between GOME-2A and the SOI at the Samoa station ($+0.58$ in the period 2007–2012 and $+0.47$ in the period 2007–2016), which nevertheless does not alter the statistical significance of the correlation.

From Fig. 8 it also appears that there are high correlations with the tropopause height. The correlation coefficient between the NCEP tropopause pressure and GOME-2A total ozone over the southern Pacific Ocean is of the order of $+0.59$ (Student's t -test statistic results: t value = 7.946, p value < 0.0001 , and $N = 119$). Accordingly, the correlation with GTO-ECV ozone data is of the order of $+0.64$ (t value = 13.165, p value < 0.0001 , and $N = 252$), and with TOMS–OMI–OMPS, it is of the order of $+0.58$ (t value = 10.913, p value < 0.0001 , and $N = 241$). The high correlation between the tropopause pressure and total ozone on in-

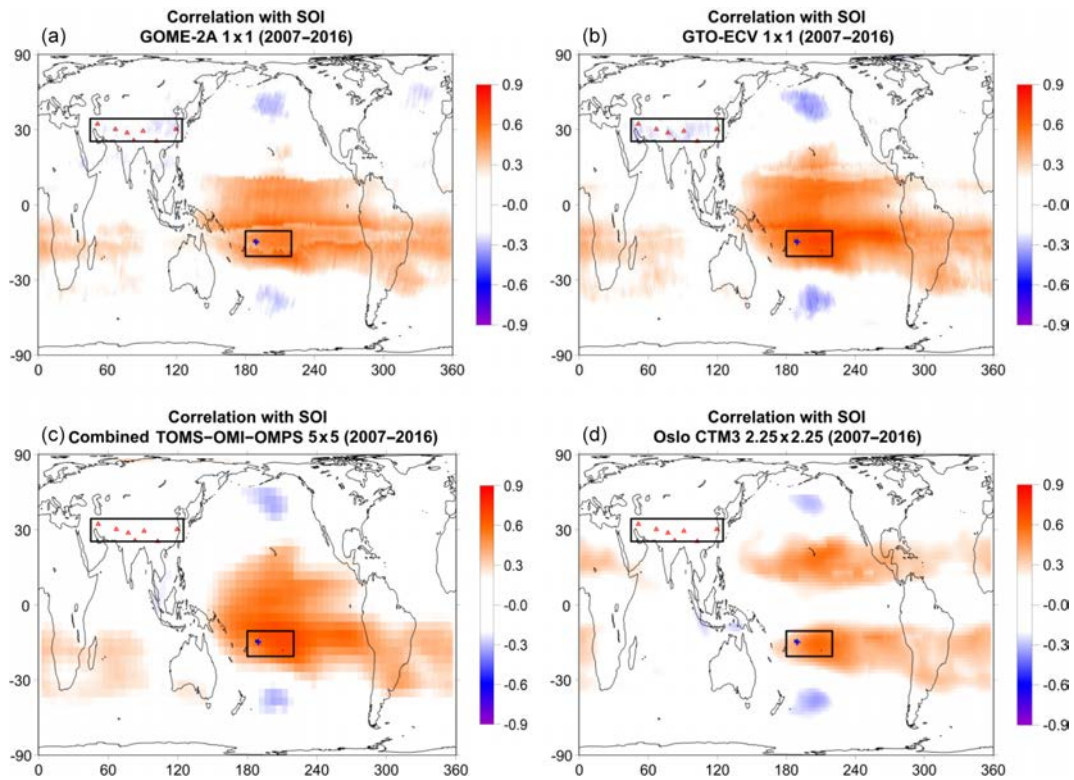


Figure 7. Map of correlation coefficients between total ozone and SOI for GOME-2A (a), GTO-ECV (b), TOMS–OMI–OMPS satellite data (c), and Oslo CTM3 model simulations (d). Rectangles correspond to the southern Pacific region (10–20° S, 180–220° E) and southern Asia region (35–45° N, 45–125° E), blue cross corresponds to the Samoa station (14.25° S, 189.4° E), and red triangles correspond to stations in southern Asia, where total ozone has been studied as to the impact of ENSO after removing variability related to the annual cycle, QBO, and solar cycle. Positive correlations are shown in red colours, while negative correlations are shown in blue colours. Only correlation coefficients above or below ± 0.2 are shown.

terannual and longer time scales points to the very strong link between these parameters. These links were already documented in the past (e.g. Steinbrecht et al., 1998, 2001) and are verified with the GOME-2A data. At the same time a strong correlation is also evident between tropopause pressure and the SOI, again on interannual and longer time scales ($R = +0.66$, t value = 13.825, p value < 0.0001, $N = 252$). The above results point to the strong impact of the ENSO on the tropical ozone column through the tropical tropopause; warm (El Niño) and cold (La Niña) events affect the variability of the tropopause, which in turn affects the distribution of stratospheric ozone. In the tropics, where total ozone is mainly stratospheric, as the tropopause moves to higher altitudes (lower pressure), the stratosphere is compressed, reducing the amount of stratospheric (total) ozone. This happens during warm (El Niño) episodes. The opposite phenomenon occurs during cold (La Niña) events, when the tropopause height decreases (higher pressure) and total ozone is then increased. These events can affect the long-term ozone trends in the tropics when looking at time periods when strong El Niño and La Niña events occur at the begin-

ning and the end of the trend period respectively (Coldewey-Egbers et al., 2014).

Furthermore, in Fig. 8 we have marked seven stations in the greater southern Asia region (35–45° N, 45–125° E), where total ozone is anti-correlated with the SOI. Admittedly, these anti-correlations are weak (about -0.3), but we thought presenting the time series in these areas to be worthwhile as well. Figure 9 shows the variability of total ozone after removing seasonal, QBO, and solar-cycle-related variations, over the southern Asian region (panel a) and over the seven stations averaged within this region (panel b). As can be seen from this figure, the explained variance from the ENSO is small, not exceeding 9%. All correlations from the comparisons with the SOI are summarized in Table 5. In spite of the small correlations with the SOI, the consistency between GOME-2A, GTO-ECV, TOMS–OMI–OMPS, and Oslo CTM3 data anomalies is very high, and their differences are within $\pm 1\%$. Differences at the seven stations in southern Asia are as follows: $-1.3 \pm 2.4\%$ between GOME-2A and GB data, $-0.4 \pm 1.0\%$ between GOME-2A and GTO-ECV, and $-0.5 \pm 1.0\%$ between GOME-2A and SBUV.

Table 5. Statistics of the comparisons between total ozone, tropopause pressures, and SOI for (a) southern Pacific (10–20° S, 180–220° E), (b) Samoa station (14.25° S, 189.4° E), (c) southern Asia (35–45° N, 45–125° E), and (d) seven stations in southern Asia.

(a) Southern Pacific	Correlation with SOI	Intercept (%)	Slope*	Error	<i>t</i> value	<i>p</i> value	<i>N</i>
GOME-2A	+0.56	−0.238	0.118	0.016	7.236	<0.0001	119
GTO-ECV	+0.66	−0.069	0.145	0.010	14.014	<0.0001	252
TOMS–OMI–OMPS	+0.62	−0.139	0.134	0.011	12.285	<0.0001	241
Oslo CTM3	+0.55	−0.064	0.144	0.014	10.501	<0.0001	252
Tropopause	+0.66	−0.761	0.241	0.017	13.825	<0.0001	252
(b) Samoa	Correlation with SOI	Intercept (%)	Slope*	Error	<i>t</i> value	<i>p</i> value	<i>N</i>
GOME-2A	+0.47	−0.217	0.108	0.018	5.823	<0.0001	119
GTO-ECV	+0.55	−0.100	0.127	0.012	10.366	<0.0001	252
SBUV overpass	+0.59	−0.114	0.127	0.011	11.398	<0.0001	251
GB (WOUDC)	+0.42	−0.058	0.106	0.017	6.194	<0.0001	178
Tropopause	+0.65	−0.799	0.223	0.017	13.405	<0.0001	252
(c) Southern Asia	Correlation with SOI	Intercept (%)	Slope*	Error	<i>t</i> value	<i>p</i> value	<i>N</i>
GOME-2A	−0.23	0.090	−0.044	0.018	−2.525	0.0129	119
GTO-ECV	−0.30	0.073	−0.074	0.015	−5.047	<0.0001	252
TOMS–OMI–OMPS	−0.28	−0.212	−0.073	0.016	−4.553	<0.0001	241
Oslo CTM3	−0.18	0.140	−0.040	0.014	−2.877	0.0044	252
Tropopause	−0.27	−0.188	−0.129	0.029	−4.476	<0.0001	252
(d) Southern Asia (seven station mean)	Correlation with SOI	Intercept (%)	Slope*	Error	<i>t</i> value	<i>p</i> value	<i>N</i>
GOME-2A	−0.23	0.090	−0.043	0.017	−2.518	0.0132	119
GTO-ECV	−0.30	0.067	−0.072	0.014	−5.040	<0.0001	252
SBUV overpass	−0.27	0.086	−0.066	0.015	−4.464	<0.0001	251
GB (WOUDC)	−0.36	0.427	−0.103	0.017	−5.912	<0.0001	240
Tropopause	−0.28	−0.122	−0.160	0.035	−4.597	<0.0001	252

* The slope is in % per unit change of the explanatory variable. Error, *t* value, and *p* value refer to slope.

In summary, our findings indicate that GOME-2A captures the disturbances in total ozone during ENSO events well with respect to satellite SBUV and GB observations. Our findings on the ENSO-related total ozone variations (low ozone during ENSO warm events, high ozone during ENSO cold events, and magnitude of changes) are in line with recent studies (e.g. Randel and Thompson, 2011; Oman et al., 2013; Sioris et al., 2014) included in the 2014 Ozone Assessment report (Pawson and Steinbrecht, 2014; WMO, 2014). Our results are also in agreement with Knibbe et al. (2014), who showed negative ozone effects of El Niño between 25° S and 25° N, especially over the Pacific.

3.4 Correlation with NAO

The residuals from Eq. (3), free from seasonal, QBO, solar, and ENSO-related variations, were later used to study the correlation between total ozone and the NAO in winter. The results are presented in Fig. 10 which shows the correlation coefficients between total ozone and the NAO index in winter from the GOME-2A (panel a), GTO-ECV (panel b) and TOMS–OMI–OMPS satellite data (panel c), and the Oslo CTM3 model calculations (panel d). Negative correlations

between total ozone and the NAO are presented with blue colours, while positive correlations are presented with red colours. From Fig. 10a it appears that total ozone is strongly correlated with the NAO in many regions. Strong negative correlation coefficients are observed in the majority of the northern mid-latitudes (*R* about −0.6), while positive correlations exist in the tropics and some negative correlations exist in the southern mid-latitudes. These characteristics are observed in both GTO-ECV and TOMS–OMI–OMPS datasets and are reproduced by the Oslo model as well, all for the common period 2007–2016. The regression coefficients on these comparisons are presented in the Fig. S4.

We note here that the results of the correlation analysis for the period 2007–2016 were based on a relative small sample of data from 10 winters, therefore many of these correlation coefficients may not be statistically significant. The statistical significance of the correlation coefficients in every grid box was only tested with the TOMS–OMI–OMPS data (Fig. A2, Appendix A), which provided us with the opportunity to calculate the respective correlations using data for the whole period of record 1979–2016. It appears that when extending the data back to the 1980s, the negative correlations in the southern mid-latitudes in winter disappear while the positive

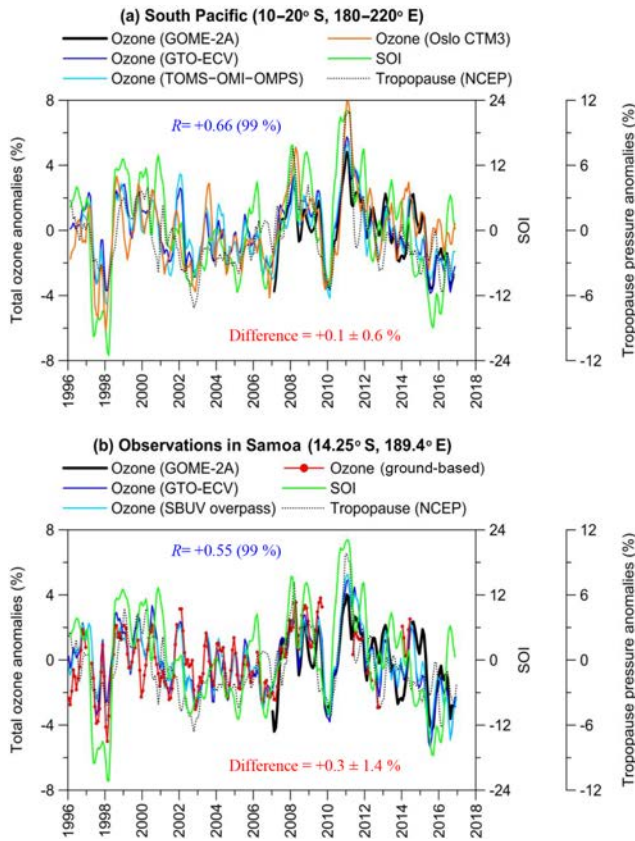


Figure 8. (a) Example of regional time series of total ozone (%) over the southern Pacific region (10–20° S, 180–220° E) along with SOI. The dotted line shows the respective tropopause pressure variability from NCEP. R is the correlation coefficient between GTO-ECV total ozone and SOI (statistical significance of R is given in parentheses). The difference refers to the mean difference $\pm\sigma$ (in %) between GTO-ECV and the combined TOMS–OMI–OMPS satellite data; (b) same as in (a), but for SBUV overpass and GB data at the Samoa station. The difference refers to the mean difference $\pm\sigma$ (in %) between GTO-ECV and GB data.

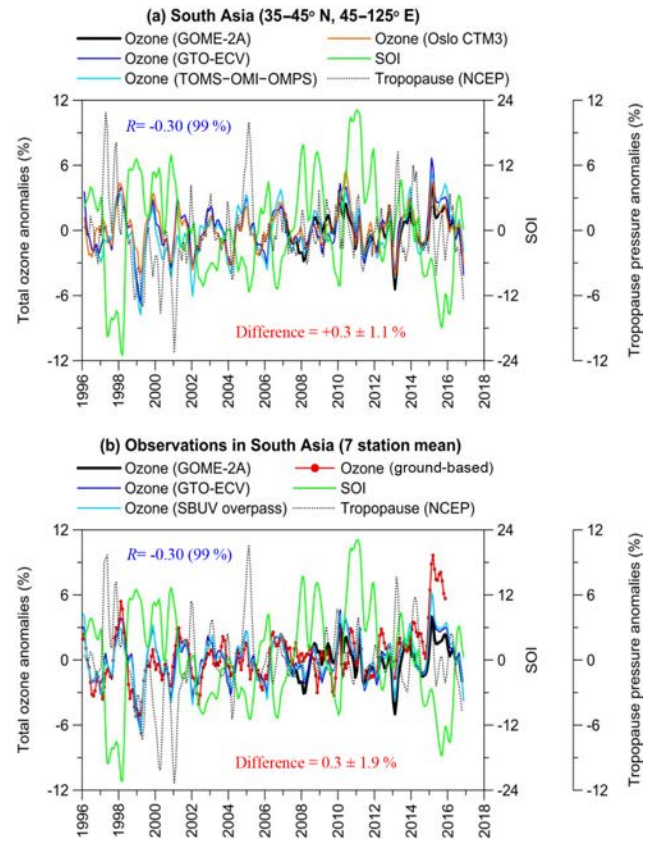


Figure 9. (a) Example of regional time series of total ozone (%) over southern Asia (35–45° N, 45–125° E) along with SOI. The dotted line shows the respective tropopause pressure variability from NCEP. R is the correlation coefficient between GTO-ECV total ozone and SOI (statistical significance of R is given in parentheses). The difference refers to the mean difference $\pm\sigma$ (in %) between GTO-ECV and the combined TOMS–OMI–OMPS satellite data; (b) same as in (a) but with SBUV overpass and GB data averaged at seven stations in southern Asia. The difference refers to the mean difference $\pm\sigma$ (in %) between GTO-ECV and GB data.

correlations in the tropics become weaker; yet the observed anti-correlation between total ozone and the NAO index in the northern mid-latitude zone remains strong. The dotted line in the plot shows areas with statistically significant correlation coefficients (99% confidence level). Indeed, in the long term, statistically significant correlations between total ozone and the NAO index during winter are mostly found over the northern mid-latitudes and the subtropics. A small, statistically significant signal is also seen over Antarctica, but it was not analysed further.

According to this finding, we have restricted the analysis of the NAO to the northern mid-latitudes. Rectangles (Fig. 10a) correspond to two regions in the North Atlantic, i.e. 35–50° N, 20–50° W and 15–27° N, 30–60° W, which were studied for the impact of the NAO on total ozone after removing variability related to the annual cycle, QBO, solar

cycle, and ENSO. In addition we have studied a number of stations in Canada, USA, and Europe that contribute ozone data to WOUDC, which are marked by red and green crosses in Fig. 10. The red crosses refer to the monitoring stations in Canada and the US, and the green crosses refer to the stations in Europe. In Fig. 11 we present the times series of total ozone anomalies from GOME-2A, GTO-ECV, and TOMS–OMI–OMPS satellite data along with the NAO index in winter over the North Atlantic. Model calculations are shown as well. The dotted line shows the respective tropopause pressure anomalies from NCEP reanalysis. Comparisons between GOME-2A, GTO-ECV, SBUV (v8.6) overpass data, and GB measurements over the various stations in Canada, USA, and Europe are shown in Fig. 12.

The observed anomalies over the North Atlantic Ocean point to the strong influence of the NAO on total ozone in

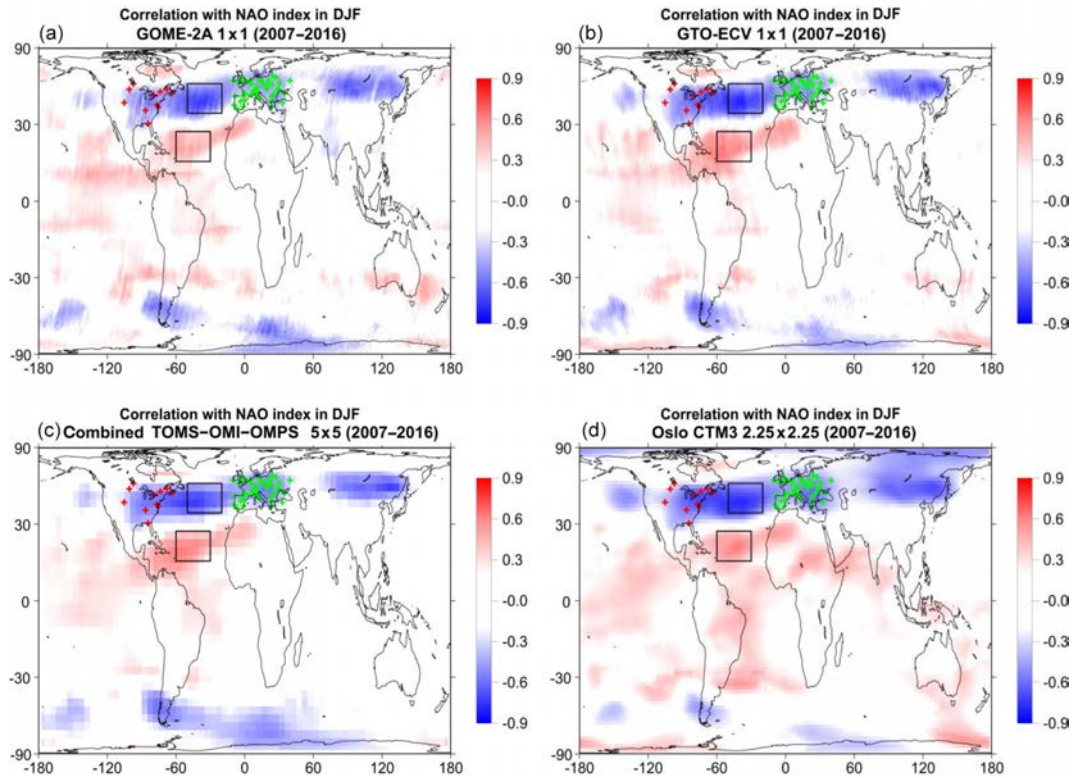


Figure 10. Map of correlation coefficients between total ozone and the NAO index during winter (December, January, and February; DJF) for GOME-2A (a), GTO-ECV (b), TOMS–OMI–OMPS satellite data (c), and Oslo CTM3 model simulations (d). Rectangles correspond to regions in the North Atlantic ($35\text{--}50^\circ\text{N}$, $20\text{--}50^\circ\text{W}$; $15\text{--}27^\circ\text{N}$, $30\text{--}60^\circ\text{W}$), and red and green crosses correspond to stations in Canada and USA and Europe, where total ozone has been studied as to the impact of NAO after removing variability related to the annual cycle, QBO, solar cycle, and ENSO. Positive correlations are shown by red colours, while negative correlations are shown by blue colours. Only correlation coefficients above or below ± 0.2 are shown.

winter. Most evident is the strong increase in total ozone in 2010 of more than 8 %, particularly over $35\text{--}50^\circ\text{N}$ and $20\text{--}50^\circ\text{W}$. This increase was accompanied by a strong increase in tropopause pressures. Both changes (in total ozone and tropopause pressures) occurred under a strong negative phase of the NAO, the strongest one in the past 20 years. We observe strong anti-correlation among total ozone and the NAO index in winter ($R = -0.74$ over $35\text{--}50^\circ\text{N}$, $20\text{--}50^\circ\text{W}$), which is statistically significant at the 99 % confidence level. This anti-correlation suggests that about 50 % of the variability of total ozone in winter is explained by the NAO when the annual cycle, QBO, solar cycle, and ENSO signals are removed. Differences for GOME-2A, and its data pairs are estimated to be $-0.7 \pm 1.1\%$ between GOME-2A and TOMS–OMI–OMPS data, $+0.1 \pm 1.0\%$ between GOME-2A and GTO-ECV, and $-0.2 \pm 1.5\%$ between GOME-2A and Oslo CTM3 data. From the regression with the NAO index we derived an NAO-related term from which we calculated the amplitude of the NAO in total ozone as $(\text{maximum ozone} - \text{minimum ozone})/2$. The amplitude of the NAO over the North Atlantic region ($35\text{--}50^\circ\text{N}$, $20\text{--}50^\circ\text{W}$) was estimated to be about 16.5 DU, or 5.2 % of the annual

mean. This is about half of the amplitude of the annual cycle (which is ~ 37 DU or 11.7 % of the mean). These estimates are based on GTO-ECV data. Similar correlation and amplitude were also found with GOME-2A, the combined TOMS–OMI–OMPS satellite data, and the Oslo CTM3 model simulations.

A similar but opposite correlation is found over the southern part of the North Atlantic ($15\text{--}27^\circ\text{N}$, $30\text{--}60^\circ\text{W}$). Here, we estimate a significant correlation coefficient of the NAO of $+0.60$, amplitude of the NAO of about 7.2 DU (2.6 % of the annual mean), and amplitude of the annual cycle of about 15.8 DU (5.7 % of the mean). Again, similar estimates are found with the GOME-2A and the TOMS–OMI–OMPS satellite data and are reproduced by the model calculations as well. The annual mean total ozone and the amplitudes of the annual cycle, QBO, solar cycle, and NAO in total ozone over the studied regions in the North Atlantic are summarized in Table 6. Differences between GOME-2A and GTO-ECV data at the southern part of North Atlantic are of the order of $-0.6 \pm 0.7\%$. Differences with the TOMS–OMI–OMPS data are estimated to be $-0.9 \pm 0.8\%$ and are estimated to be $-0.1 \pm 0.7\%$ with the Oslo CTM3.

Table 6. Annual mean total ozone, amplitude of annual cycle, amplitude of QBO, amplitude of solar cycle, and amplitude of NAO in the period 1995–2016 from GOME-2A, GTO-ECV, the combined TOMS–OMI–OMPS satellite data, and Oslo CTM3 model calculations over the North Atlantic Ocean, in (a) region 35–50° N, 20–50° W, and (b) region 15–27° N, 30–60° W.

	North Atlantic Ocean							
	(a) 35–50° N, 20–50° W				(b) 15–27° N, 30–60° W			
	GOME-2A*	GTO-ECV	TOMS–OMI–OMPS	Oslo CTM3	GOME-2A*	GTO-ECV	TOMS–OMI–OMPS	Oslo CTM3
Annual mean	319.7 DU	315.9 DU	317.3 DU	311.2 DU	276.6 DU	276.4 DU	274.4 DU	282.6 DU
Amplitude of annual cycle	37.4 DU (11.7 %)	37.0 DU (11.7 %)	36.9 DU (11.6 %)	32.0 DU (10.3 %)	12.7 DU (4.6 %)	15.8 DU (5.7 %)	15.1 DU (5.5 %)	15.5 DU (5.5 %)
Amplitude of QBO	2.5 DU (0.8 %)	2.3 DU (0.7 %)	2.6 DU (0.8 %)	3.2 DU (1.0 %)	3.0 DU (1.1 %)	2.8 DU (1.0 %)	3.9 DU (1.4 %)	4.3 DU (1.5 %)
Amplitude of solar cycle	0.4 DU (0.1 %)	0.3 DU (0.1 %)	2.2 DU (0.7 %)	2.3 DU (0.7 %)	3.5 DU (1.3 %)	2.7 DU (1.0 %)	3.3 DU (1.2 %)	1.0 DU (0.3 %)
Amplitude of NAO (winter)	18.3 DU (5.7 %)	16.5 DU (5.2 %)	18.4 DU (5.8 %)	18.3 DU (5.9 %)	4.2 DU (1.5 %)	7.2 DU (2.6 %)	5.0 DU (1.8 %)	8.0 DU (2.8 %)

* Period 2007–2016.

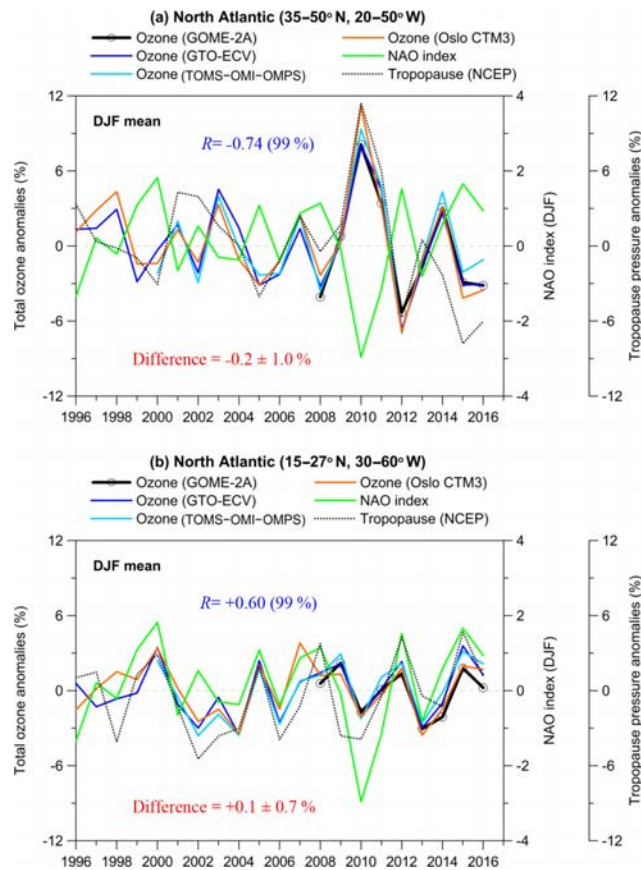


Figure 11. Example of regional time series of total ozone (%) over the North Atlantic regions (a) 35–50° N, 20–50° W, and (b) 15–27° N, 30–60° W, in winter (DJF mean) along with the NAO index. The dotted line shows the respective tropopause pressure variability from NCEP reanalysis. R is the correlation coefficient between GTO-ECV total ozone and the NAO index. The differences refer to the mean differences $\pm\sigma$ (in %) between GTO-ECV and the combined TOMS–OMI–OMPS satellite data.

The time series of total ozone anomalies and of the NAO index for the examined stations in Canada, USA, and Europe are presented in Fig. 12. Table 7 presents the respective statistics. The correlation between total ozone and the NAO index in winter after removing ozone variability related to the annual cycle, QBO, solar cycle, and ENSO is -0.40 (90 % confidence level). Again, a particular feature was the total ozone increase in 2010 by 6 % of the mean associated with the negative NAO phase. This increase is noteworthy because of the consistency with the GB measurements and the satellite SBUV overpass data and, in general, the agreement found between the variability of the tropopause pressures and total ozone. Differences between GOME-2A and GB data are -1.0 ± 1.8 %. Accordingly we estimate differences of about -1.1 ± 0.5 % between GOME-2A and GTO-ECV data and of about -1.3 ± 0.6 % between GOME-2A and SBUV data. On the basis of GTO-ECV data we estimate that in Canada and the USA, the amplitude of the NAO in total ozone in winter is about 7 DU (or 2.2 % of the mean), while it is estimated to be about 9 DU (or 2.7 % of the mean) over Europe. These numbers are slightly smaller than the GOME-2A, GB, and SBUV estimates, less than about one percent (Table 7).

The anti-correlation between total ozone column and the NAO index during winter also applies to southern Europe and the Mediterranean. Following the study of Ossó et al. (2011), who reported a reversal in the correlation pattern between the NAO and total ozone from winter to summer in southern Europe, we have looked at the correlations during summer as well. Figure 13 presents the comparisons for 21 ground-based stations located in the region bounded by latitudes 30–47° N and by longitudes 10° W–40° E. Figure 13a shows results for the summer, and Fig. 13b shows results for the winter. As can be seen, the observed anti-correlation between GB total ozone and the NAO in winter ($R = -0.43$, slope = -0.980 , t value = -2.095 , p value = 0.0499 , and $N = 21$) reverses its sign and becomes positive in the summer ($R = +0.60$, slope = 0.874 , t value = 3.309 , p value =

Table 7. Annual mean total ozone, amplitude of annual cycle, amplitude of QBO, amplitude of solar cycle, and amplitude of NAO in the period 1995–2016 from GOME-2A, GTO-ECV satellite data, ground-based observations, and SBUV (v8.6) satellite overpass data over (a) Canada and USA (11 station mean) and (b) Europe (41 station mean).

	(a) Canada and USA				(b) Europe			
	30–50° N, 60–110° W (11 station mean)				35–55° N, 10° W–40° E (41 station mean)			
	GOME-2A*	GTO-ECV	Ground	SBUV (v8.6)	GOME-2A*	GTO-ECV	Ground	SBUV (v8.6)
Annual mean	324.2 DU	320.6 DU	322.5 DU	320.9 DU	329.9 DU	325.7 DU	326.9 DU	326.8 DU
Amplitude of annual cycle	38.1 DU (11.7 %)	34.1 DU (10.6 %)	33.2 DU (10.3 %)	34.0 DU (10.6 %)	39.3 (11.9 %)	40.5 DU (12.4 %)	39.2 DU (12.0 %)	40.7 DU (12.4 %)
Amplitude of QBO	2.1 DU (0.6 %)	2.5 DU (0.8 %)	3.5 DU (1.1 %)	2.6 DU (0.8 %)	2.7 DU (0.8 %)	1.9 DU (0.6 %)	2.8 DU (0.8 %)	2.2 DU (0.7 %)
Amplitude of solar cycle	0.3 DU (0.1 %)	0.5 DU (0.2 %)	1.4 DU (0.4 %)	0.5 DU (0.2 %)	2.1 DU (0.6 %)	0.8 DU (0.2 %)	1.0 DU (0.3 %)	0.3 DU (0.1 %)
Amplitude of NAO (winter)	9.8 DU (3.0 %)	6.9 DU (2.2 %)	8.7 DU (2.7 %)	9.3 DU (2.9 %)	9.8 DU (3.0 %)	8.9 DU (2.7 %)	11.8 DU (3.6 %)	9.9 DU (3.0 %)

* Period 2007–2016.

Table 8. Statistics of the comparisons between total ozone, tropopause pressures, and NAO index in winter (DJF mean) for (a) the northern part of North Atlantic (35–50° N, 20–50° W), (b) its southern part (15–27° N, 30–60° W), (c) 11 stations in Canada and USA, and (d) 41 stations in Europe.

(a) Northern part of North Atlantic	Correlation with NAO in winter	Intercept (%)	Slope*	Error	<i>t</i> value	<i>p</i> value	<i>N</i>
GOME-2A	–0.85	0.035	–2.474	0.568	–4.355	0.0033	9
GTO-ECV	–0.74	0.412	–2.188	0.453	–4.827	0.0001	21
TOMS–OMI–OMPS	–0.74	0.734	–2.386	0.538	–4.436	0.0004	18
Oslo CTM3	–0.75	0.639	–2.457	0.498	–4.937	<0.0001	21
Tropopause	–0.83	0.665	–3.112	0.480	–6.478	<0.0001	21
(b) Southern part of North Atlantic	Correlation with NAO in winter	Intercept (%)	Slope*	Error	<i>t</i> value	<i>p</i> value	<i>N</i>
GOME-2A	+0.54	–0.132	0.661	0.386	1.712	0.1306	9
GTO-ECV	+0.60	–0.202	1.097	0.333	3.291	0.0038	21
TOMS–OMI–OMPS	+0.58	–0.334	1.138	0.402	2.832	0.0120	18
Oslo CTM3	+0.65	–0.077	1.188	0.316	3.761	0.0013	21
Tropopause	+0.59	–0.702	1.547	0.482	3.207	0.0046	21
(c) CA and USA (11 station mean)	Correlation with NAO in winter	Intercept (%)	Slope*	Error	<i>t</i> value	<i>p</i> value	<i>N</i>
GOME-2A	–0.71	–0.042	–1.305	0.493	–2.647	0.0331	9
GTO-ECV	–0.40	0.308	–0.904	0.479	–1.886	0.0746	21
SBUV overpass	–0.50	0.318	–1.209	0.476	–2.541	0.0199	21
GB (WOUDC)	–0.46	0.268	–1.046	0.477	–2.190	0.0419	20
Tropopause	–0.41	0.268	–0.739	0.377	–1.959	0.0650	21
(d) Europe (41 station mean)	Correlation with NAO in winter	Intercept (%)	Slope*	Error	<i>t</i> value	<i>p</i> value	<i>N</i>
GOME-2A	–0.46	0.089	–1.282	0.897	–1.428	0.1963	9
GTO-ECV	–0.42	0.315	–1.141	0.573	–1.992	0.0609	21
SBUV overpass	–0.47	0.389	–1.264	0.543	–2.329	0.0311	21
GB (WOUDC)	–0.48	0.625	–1.327	0.560	–2.368	0.0287	21
Tropopause	–0.40	0.048	–0.989	0.523	–1.891	0.0739	21

* The slope is in % per unit change of the explanatory variable. Error, *t* value, and *p* value refer to slope.

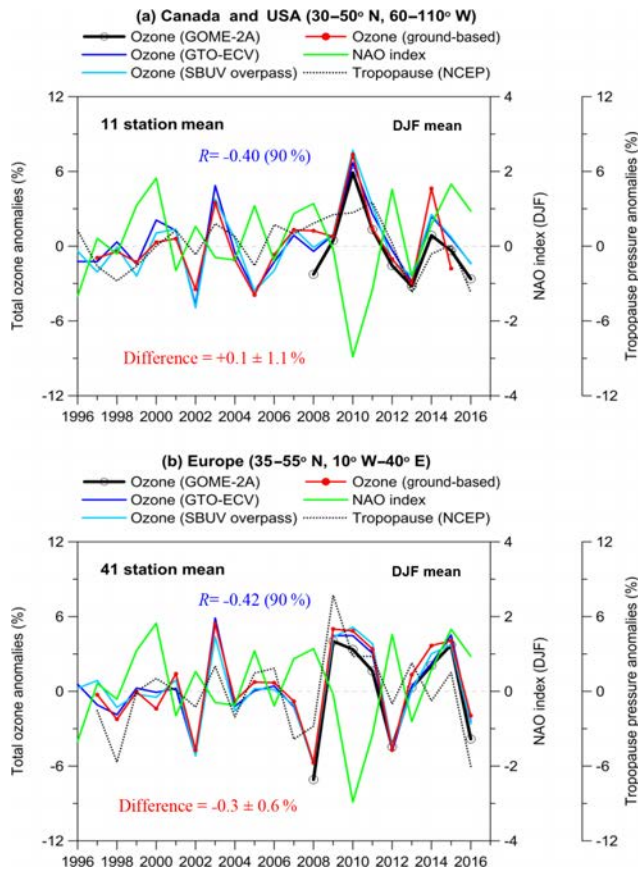


Figure 12. Comparison with GB observations over (a) Canada and USA and (b) Europe in winter (DJF mean). R is the correlation coefficient between GTO-ECV total ozone and the NAO index. The differences refer to the mean differences $\pm\sigma$ (in %) between GTO-ECV and GB data.

0.0037, and $N = 21$), indicating that the NAO explains about 36 % of ozone variability in the summer in this region. A similar picture is also seen from GOME-2A, GTO-ECV, and SBUV data.

In summary, our findings based on GOME-2A, GTO-ECV, and SBUV overpass data are in line with those found by Ossó et al. (2011) and Steinbrecht et al. (2011), who analysed TOMS and OMI satellite data and GB measurements at the Hohenpeißenberg station, respectively. During winter, total ozone variability associated with the NAO is particularly important over northern Europe, the US East Coast, and Canada, explaining up to 30 % of total ozone variance for this region (Ossó et al., 2011). Also, both studies found unusually high total ozone columns in 2010 over much of the Northern Hemisphere and related them to the negative phase of the NAO or AO (the Arctic Oscillation).

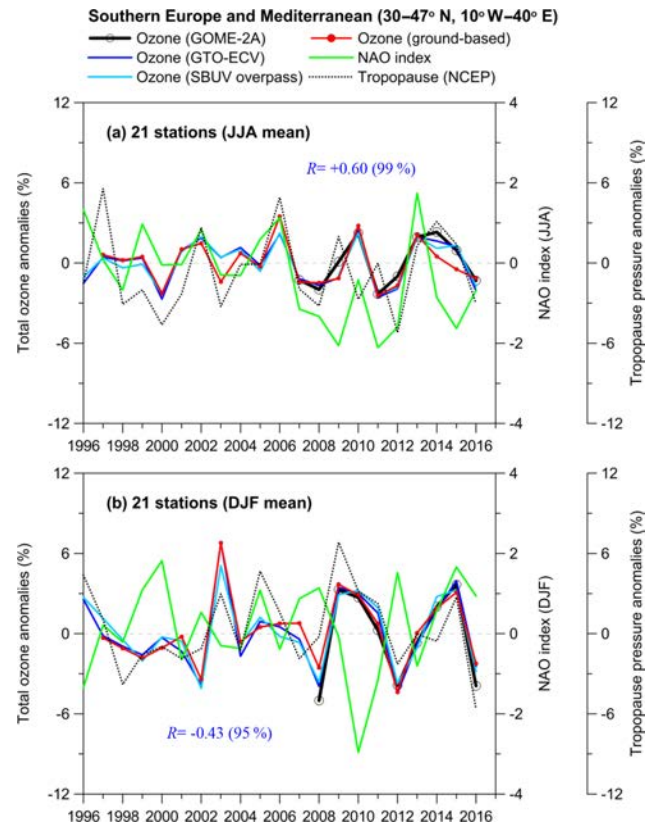


Figure 13. Relation between total ozone and the NAO index in summer (JJA mean) and winter (DJF mean) for 21 stations in southern Europe. The correlation coefficients refer to NAO index and GB total ozone after removing variability related to the seasonal cycle, QBO, solar cycle, and ENSO.

4 Conclusions

We have evaluated the ability of GOME-2–MetOp-A (GOME-2A) satellite total ozone retrievals to capture known natural oscillations such as the QBO, ENSO, and NAO. In general, GOME-2A depicts these natural oscillations in concurrence with GTO-ECV, TOMS–OMI–OMPS, and SBUV (v8.6) satellite overpass data; ground-based measurements (Brewer, Dobson, filter, and SAOZ); and chemical transport model calculations (Oslo CTM3).

Mean differences between GOME-2A and SBUV total ozone were found to be $+0.1 \pm 0.7\%$ in the tropics ($0\text{--}30^\circ$), about $+0.8 \pm 1.6\%$ in the mid-latitudes ($30\text{--}60^\circ$), about $+1.3 \pm 2.2\%$ over the northern high latitudes ($60\text{--}80^\circ\text{N}$), and about $-0.5 \pm 2.9\%$ over the southern high latitudes ($60\text{--}80^\circ\text{S}$). These differences were estimated as $(\text{GOME-2A} - \text{SBUV})/\text{SBUV}$ (%) from January 2007 to December 2016. Small differences were also found between GOME-2A and GB measurements, with standard deviations of the differences being $\pm 1.4\%$ in the tropics, $\pm 2.1\%$ in the mid-latitudes, and $\pm 3.2\%$ and $\pm 4.3\%$ over the northern and the southern high latitudes respectively.

The variability of total ozone from GOME-2A has been compared with the variability of total ozone from other examined datasets as to their agreement depicting natural atmospheric phenomena such as the QBO, ENSO, and NAO. First, we studied correlations between total ozone and the QBO after removing variability related to the seasonal cycle from the ozone datasets. Then, we examined correlations between total ozone and the ENSO after removing variability related to the QBO and the solar cycle, and we finally examined correlations with the NAO after removing variability related to the QBO, solar cycle, and ENSO. Our main results are as follows.

QBO. Total ozone from GOME-2A is well correlated with the quasi-biennial oscillation (+0.8 in the tropics) in agreement with GTO-ECV, SBUV, and GB data. The amplitude of the QBO on total ozone maximizes around the Equator, and it is estimated to be about 2.6 % of the mean. Going from low to mid-latitudes there is a phase shift in the QBO impact on total ozone. Correlation coefficients between GOME-2A total ozone and the QBO over 30–60° north and south are –0.1 and –0.5 respectively, in agreement with the correlations between GB total ozone and the QBO (–0.2 and –0.5, respectively). On the basis of GOME-2A, the amplitude of QBO in total ozone is estimated to be 0.6 % of the mean in the northern mid-latitudes and 1.4 % of the mean in the southern mid-latitudes.

ENSO. Correlation coefficients among GOME-2A total ozone and the SOI in the tropical Pacific Ocean are estimated to be about +0.6, consistent with GTO-ECV, SBUV, and GB observations. It was found that the El Niño–Southern Oscillation (ENSO) signal is evident and consistent in all examined datasets. The amplitude of ENSO in total ozone is about 6–9 DU, corresponding to about 2.5 %–3.5 % of the annual mean. Differences between GOME-2A, GTO-ECV, and GB measurements during warm (El Niño) and cold (La Niña) events are within ± 1.5 %. Similar estimates also result from the Dobson measurements in American Samoa, indicating that the Samoa station represents the greater area in the southern Pacific well for satellite evaluations as to the impact of the ENSO.

NAO. The respective results related to the impact of the North Atlantic Oscillation over the northern mid-latitudes showed a clear NAO signal in winter in all datasets, with amplitudes of about 16–19 DU (about 5 %–6 % of the annual mean) in the North Atlantic, 9–12 DU (3 %–4 % of the mean) over Europe, and 7–10 DU (2 %–3 % of the mean) over Canada and the US. Comparison with GB observations over Canada and Europe showed very good agreement between GOME-2A, GTO-ECV, and GB observations as to the influence of the NAO, with differences within ± 1 %.

In addition to the usual validation methods, which compare monthly mean and zonal mean total ozone data and analyse the differences between satellite and GB instruments, we showed here that quasi-cyclical perturbations such as the QBO, ENSO, and NAO can serve as independent proxies of spatiotemporal variation to qualitatively evaluate GOME-2A satellite total ozone against ground-based and other satellite total ozone datasets. The agreement and small differences which were found between the variability of total ozone from GOME-2A and the variability of total ozone from other satellite retrievals and ground-based measurements during these naturally occurring oscillations verify the good quality of GOME-2A satellite total ozone to be used in ozone–climate research studies.

Data availability. Satellite SBUV (v8.6) total ozone station overpass data were downloaded from https://acd-ext.gsfc.nasa.gov/Data_services/merged/index.html (last access: 8 February 2019; McPeters et al., 2013; Bhartia et al., 2013). GTO-ECV total ozone data are available at <http://www.esa-ozone-cci.org/?q=node/160> (last access: 8 February 2019; Coldewey-Egbers et al., 2015; Garane et al., 2018). Ground-based total ozone daily summaries were obtained from the World Ozone and Ultraviolet Radiation Data Centre (WOUDC) at <https://doi.org/10.14287/10000001> (WOUDC, 2018). The QBO component of total ozone was examined by using the monthly mean zonal winds in Singapore at 30 hPa. Zonal wind data at 30 hPa were provided by the Freie Universität Berlin (FU-Berlin) at <http://www.geo.fu-berlin.de/met/ag/strat/produkte/qbo/qbo.dat> (last access: 8 February 2019; Naujokat, 1986). The Southern Oscillation Index (SOI) was provided by the Bureau of Meteorology of the Australian Government at <http://www.bom.gov.au/climate/current/soi2.shtml> (Australian Government – Bureau of Meteorology, 2018). The NAO index for December, January, and February was provided by the Climate Analysis Section of NCAR in Boulder, CO, USA at <https://climatedataguide.ucar.edu/climate-data/hurrell-north-atlantic-oscillation-nao-index-pc-based> (last access: 8 February 2019; Hurrell and Deser, 2009). The tropopause pressures from the NCEP/NCAR Reanalysis 1 dataset were downloaded from <https://www.esrl.noaa.gov/psd/data/gridded/data.ncep.reanalysis.tropopause.html> (last access: 8 February 2019; Kalnay et al., 1996).

Appendix A

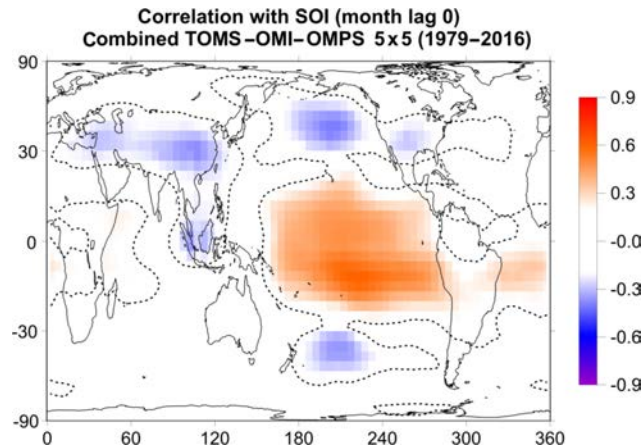


Figure A1. Map of correlation coefficients between total ozone from TOMS–OMI–OMPS satellite data and SOI for the whole period 1979–2016, after removing variability related to the seasonal cycle, QBO, and solar cycle. The dotted line binds the regions where the correlation coefficients are statistically significant at the 99 % confidence level (t test). Only correlation coefficients above or below ± 0.2 are shown. Ozone data for the period 1991–1993 after the Mt Pinatubo eruption were not used in the correlation analysis to avoid any data contamination by the volcanic aerosols.

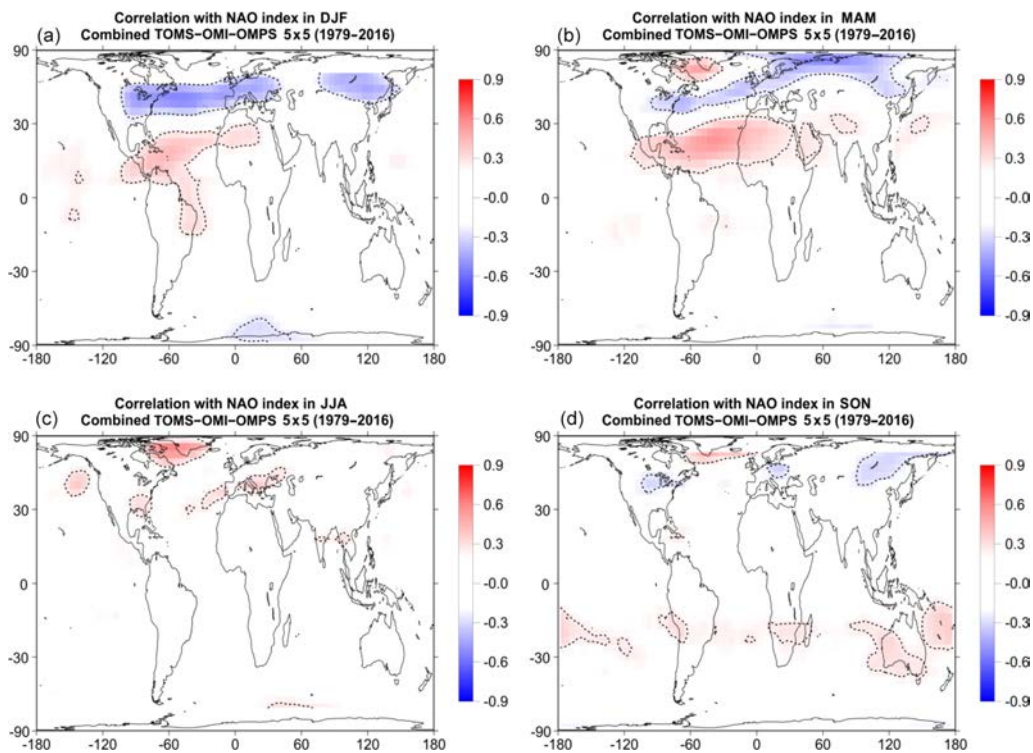


Figure A2. Map of correlation coefficients between total ozone from TOMS–OMI–OMPS satellite data and the NAO index during winter (December, January, and February – DJF; **a**), spring (March, April, and May – MAM; **b**), summer (June, July, and August – JJA; **c**), and autumn (September, October, and November – SON; **d**) for the whole period 1979–2016, after removing variability related to the seasonal cycle, QBO, solar cycle, and ENSO. The dotted line binds the regions where the correlation coefficients are statistically significant at the 99 % confidence level (t test). Only correlation coefficients above or below ± 0.2 are shown. Ozone data for the period 1991–1993 after the Mt Pinatubo eruption were not used in the correlation analysis to avoid any data contamination by the volcanic aerosols.

Supplement. The supplement related to this article is available online at: <https://doi.org/10.5194/amt-12-987-2019-supplement>.

Author contributions. KE prepared the paper based on contributions from all co-authors. CZ, DB, and MEK evaluated the results. MCE, DL, PV, CL, and SH processed GOME-2A satellite data. JK processed ground-based data. SF processed TOMS-OMI-OMPS and SBUV-2 satellite data. AH and ISAI processed Oslo CTM3 model data.

Competing interests. The authors declare that they have no conflict of interest.

Acknowledgements. Development of the GOME-2 and MetOp A total ozone products and their validation have been funded by the AC SAF project with EUMETSAT and national contributions. We acknowledge support of this work by the project “PANhellenic infrastructure for Atmospheric Composition and climatE chAnge” (MIS 5021516), which is implemented under the initiative “Reinforcement of the Research and Innovation Infrastructure”, funded by the operational programme “Competitiveness, Entrepreneurship and Innovation” (NSRF 2014–2020), and co-financed by Greece and the European Union (European Regional Development Fund). We further acknowledge the Mariolopoulos-Kanaginis Foundation for the Environmental Sciences, the ESA Ozone CCI project, and the NASA Goddard Space Flight Center. The ground-based data used in this publication were obtained as part of WMO’s Global Atmosphere Watch (GAW) and are publicly available via the World Ozone and Ultraviolet Radiation Data Centre (WOUDC). The authors would like to thank all the scientists that provide quality-assured total ozone column data on a timely basis to the WOUDC database. We acknowledge the National Oceanic and Atmospheric Administration (NOAA) for maintaining the American Samoa Dobson station. Kostas Eleftheratos and Christos S. Zerefos would like to dedicate the study to the memory of Ivar Isaksen (University of Oslo), who passed away on 16 May 2017.

Edited by: Piet Stammes

Reviewed by: two anonymous referees

References

- Australian Government – Bureau of Meteorology: Southern Oscillation Index (SOI) since 1986, available at: <http://www.bom.gov.au/climate/current/soi2.shtml>, last access: 15 June 2018.
- Baldwin, M. P., Gray, L. J., Dunkerton, T. J., Hamilton, K., Haynes, P. H., Randel, W. J., Holton, J. R., Alexander, M. J., Hirota, I., Horinouchi, T., Jones, D. B. A., Kinnersley, J. S., Marquardt, C., Sato, K., and Takahashi, M.: The quasi-biennial oscillation, *Rev. Geophys.*, 39, 179–229, <https://doi.org/10.1029/1999RG000073>, 2001.
- Bhartia, P. K., McPeters, R. D., Flynn, L. E., Taylor, S., Kramarova, N. A., Frith, S., Fisher, B., and DeLand, M.: Solar Backscatter UV (SBUV) total ozone and profile algorithm, *Atmos. Meas. Tech.*, 6, 2533–2548, <https://doi.org/10.5194/amt-6-2533-2013>, 2013.
- Brönnimann, S., Bhend, J., Franke, J., Flückiger, S., Fischer, A. M., Bleisch, R., Bodeker, G., Hassler, B., Rozanov, E., and Schraner, M.: A global historical ozone data set and prominent features of stratospheric variability prior to 1979, *Atmos. Chem. Phys.*, 13, 9623–9639, <https://doi.org/10.5194/acp-13-9623-2013>, 2013.
- Chehade, W., Weber, M., and Burrows, J. P.: Total ozone trends and variability during 1979–2012 from merged data sets of various satellites, *Atmos. Chem. Phys.*, 14, 7059–7074, <https://doi.org/10.5194/acp-14-7059-2014>, 2014.
- Chiou, E. W., Bhartia, P. K., McPeters, R. D., Loyola, D. G., Coldewey-Egbers, M., Fioletov, V. E., Van Roozendaal, M., Spurr, R., Lerot, C., and Frith, S. M.: Comparison of profile total ozone from SBUV (v8.6) with GOME-type and ground-based total ozone for a 16-year period (1996 to 2011), *Atmos. Meas. Tech.*, 7, 1681–1692, <https://doi.org/10.5194/amt-7-1681-2014>, 2014.
- Coldewey-Egbers, M., Loyola, R., D. G., Braesicke, P., Dameris, M., van Roozendaal, M., Lerot, C., and W. Zimmer, W.: A new health check of the ozone layer at global and regional scales, *Geophys. Res. Lett.*, 41, 4363–4372, <https://doi.org/10.1002/2014GL060212>, 2014.
- Coldewey-Egbers, M., Loyola, D. G., Koukoulis, M., Balis, D., Lambert, J.-C., Verhoelst, T., Granville, J., van Roozendaal, M., Lerot, C., Spurr, R., Frith, S. M., and Zehner, C.: The GOME-type Total Ozone Essential Climate Variable (GTO-ECV) data record from the ESA Climate Change Initiative, *Atmos. Meas. Tech.*, 8, 3923–3940, <https://doi.org/10.5194/amt-8-3923-2015>, 2015 (data available at: <http://www.esa-ozone-cci.org/?q=node/160>, last access: 8 February 2019).
- Dameris, M., Nodorp, D., and Sausen, R.: Correlation between Tropopause Height Pressure and TOMS-Data for the EASOE-Winter 1991/1992, *Beitr. Phys. Atmosph.*, 68, 227–232, 1995.
- de Laat, A. T. J., van Weele, M., and van der A., R. J.: Onset of stratospheric ozone recovery in the Antarctic ozone hole in assimilated daily total ozone columns, *J. Geophys. Res.-Atmos.*, 122, 11880–11899, <https://doi.org/10.1002/2016JD025723>, 2017.
- Dütsch, H. U.: The ozone distribution in the atmosphere, *Can. J. Chem.*, 52, 1491–1504, 1974.
- Eleftheratos, K., Isaksen, I. S. A., Zerefos, C. S., Tourpali, K., and Nastos, P.: Comparison of Ozone Variations from Model Calculations (OsloCTM2) and Satellite Retrievals (SBUV), 11th International Conference on Meteorology, Climatology and Atmospheric Physics (COMECAP 2012), Athens, Greece, 29 May–1 June 2012, edited by: Helmis, C. G. and Nastos, P. T., *Advances in Meteorology, Climatology and Atmospheric Physics*, Springer Atmospheric Sciences, ©Springer-Verlag Berlin Heidelberg, https://doi.org/10.1007/978-3-642-29172-2_132, 945–950, 2012.
- Eleftheratos, K., Isaksen, I., Zerefos, C., Nastos, P., Tourpali, K., and Rognerud, B.: Ozone variations derived by a chemical transport model, *Water Air Soil Pollut.*, 224, 1585, <https://doi.org/10.1007/s11270-013-1585-2>, 2013.
- Frith, S. M., Kramarova, N. A., Stolarski, R. S., McPeters, R. D., Bhartia, P. K., and Labow, G. J.: Recent changes in total column ozone based on the SBUV Version 8.6

- merged ozone data set, *J. Geophys. Res.*, 119, 9735–9751, <https://doi.org/10.1002/2014JD021889>, 2014.
- Frossard, L., Rieder, H. E., Ribatet, M., Staehelin, J., Maeder, J. A., Di Rocco, S., Davison, A. C., and Peter, T.: On the relationship between total ozone and atmospheric dynamics and chemistry at mid-latitudes – Part 1: Statistical models and spatial fingerprints of atmospheric dynamics and chemistry, *Atmos. Chem. Phys.*, 13, 147–164, <https://doi.org/10.5194/acp-13-147-2013>, 2013.
- Garane, K., Lerot, C., Coldewey-Egbers, M., Verhoelst, T., Koukouli, M. E., Zyrichidou, I., Balis, D. S., Danckaert, T., Goutail, F., Granville, J., Hubert, D., Keppens, A., Lambert, J.-C., Loyola, D., Pommereau, J.-P., Van Roozendael, M., and Zehner, C.: Quality assessment of the Ozone_cci Climate Research Data Package (release 2017) – Part 1: Ground-based validation of total ozone column data products, *Atmos. Meas. Tech.*, 11, 1385–1402, <https://doi.org/10.5194/amt-11-1385-2018>, 2018.
- Hao, N., Koukouli, M. E., Inness, A., Valks, P., Loyola, D. G., Zimmer, W., Balis, D. S., Zyrichidou, I., Van Roozendael, M., Lerot, C., and Spurr, R. J. D.: GOME-2 total ozone columns from MetOp-A/MetOp-B and assimilation in the MACC system, *Atmos. Meas. Tech.*, 7, 2937–2951, <https://doi.org/10.5194/amt-7-2937-2014>, 2014.
- Hassinen, S., Balis, D., Bauer, H., Begoin, M., Delcloo, A., Eleftheratos, K., Gimeno Garcia, S., Granville, J., Grossi, M., Hao, N., Hedelt, P., Hendrick, F., Hess, M., Heue, K.-P., Hovila, J., Jönch-Sørensen, H., Kalakoski, N., Kauppi, A., Kiemle, S., Kins, L., Koukouli, M. E., Kujanpää, J., Lambert, J.-C., Lang, R., Lerot, C., Loyola, D., Pedernana, M., Pinardi, G., Romahn, F., van Roozendael, M., Lutz, R., De Smedt, I., Stammes, P., Steinbrecht, W., Tamminen, J., Theys, N., Tilstra, L. G., Tuinder, O. N. E., Valks, P., Zerefos, C., Zimmer, W., and Zyrichidou, I.: Overview of the O3M SAF GOME-2 operational atmospheric composition and UV radiation data products and data availability, *Atmos. Meas. Tech.*, 9, 383–407, <https://doi.org/10.5194/amt-9-383-2016>, 2016.
- Heggin, M. I., Fahey, D. W., McFarland, M., Montzka, S. A., and Nash, E. R.: Twenty questions and answers about the ozone layer: 2014 update, Scientific Assessment of Ozone Depletion: 2014, 84 pp., World Meteorological Organization, Geneva, Switzerland, ISBN 978-9966-076-02-1, 2015.
- Hoinka, K. P., Claude, H., and Köhler, U.: On the correlation between tropopause pressure and ozone above Central Europe, *Geophys. Res. Lett.*, 23, 1753–1756, 1996.
- Hurrell, J. W. and Deser, C.: North Atlantic climate variability: The role of the North Atlantic Oscillation, *J. Mar. Syst.*, 78, 28–41, <https://doi.org/10.1016/j.jmarsys.2008.11.026>, 2009 (data available at: <https://climatedataguide.ucar.edu/climate-data/hurrell-north-atlantic-oscillation-nao-index-pc-based>, last access: 8 February 2019).
- Isaksen, I. S. A., Berntsen, T. K., Dalsøren, S. B., Eleftheratos, K., Orsolini, Y., Rognerud, B., Stordal, F., Søvde, O. A., Zerefos, C., and Holmes, C. D.: Atmospheric ozone and methane in a changing climate, *Atmosphere*, 5, 518–535, <https://doi.org/10.3390/atmos5030518>, 2014.
- Kalnay, E., Kanamitsu, M., Kistler, R., Collins, W., Deaven, D., Gandin, L., Iredell, M., Saha, S., White, G., Woollen, J., Zhu, Y., Chelliah, M., Ebisuzaki, W., Higgins, W., Janowiak, J., Mo, K. C., Ropelewski, C., Wang, J., Leetmaa, A., Reynolds, R., Jenne, R., and Joseph, D.: The NCEP/NCAR 40-year reanalysis project, *B. Am. Meteorol. Soc.*, 77, 437–472, [https://doi.org/10.1175/1520-0477\(1996\)077<0437:TNYRP>2.0.CO;2](https://doi.org/10.1175/1520-0477(1996)077<0437:TNYRP>2.0.CO;2), 1996 (data available at: https://www.esrl.noaa.gov/psd/data/gridded/data.ncep_reanalysis.tropopause.html, last access: 8 February 2019).
- Knibbe, J. S., van der A, R. J., and de Laat, A. T. J.: Spatial regression analysis on 32 years of total column ozone data, *Atmos. Chem. Phys.*, 14, 8461–8482, <https://doi.org/10.5194/acp-14-8461-2014>, 2014.
- Koukouli, M. E., Balis, D. S., Loyola, D., Valks, P., Zimmer, W., Hao, N., Lambert, J.-C., Van Roozendael, M., Lerot, C., and Spurr, R. J. D.: Geophysical validation and long-term consistency between GOME-2/MetOp-A total ozone column and measurements from the sensors GOME/ERS-2, SCIAMACHY/ENVISAT and OMI/Aura, *Atmos. Meas. Tech.*, 5, 2169–2181, <https://doi.org/10.5194/amt-5-2169-2012>, 2012.
- Koukouli, M. E., Lerot, C., Granville, J., Goutail, F., Lambert, J.-C., Pommereau, J.-P., Balis, D., Zyrichidou, I., Van Roozendael, M., Coldewey-Egbers, M., Loyola, D., Labow, G., Frith, S., Spurr, R., and Zehner, C.: Evaluating a new homogeneous total ozone climate data record from GOME/ERS-2, SCIAMACHY/Envisat and GOME-2/MetOp-A, *J. Geophys. Res.-Atmos.*, 120, 12296–12312, <https://doi.org/10.1002/2015JD023699>, 2015.
- Kuttippurath, J. and Nair, P. J.: The signs of Antarctic ozone hole recovery, *Sci. Rep.*, 7, 585, <https://doi.org/10.1038/s41598-017-00722-7>, 2017.
- Labow, G. J., McPeters, R. D., Bhartia, P. K., and Kramarova, N.: A comparison of 40 years of SBUV measurements of column ozone with data from the Dobson/Brewer network, *J. Geophys. Res.-Atmos.*, 118, 7370–7378, <https://doi.org/10.1002/jgrd.50503>, 2013.
- Lerot, C., Van Roozendael, M., Spurr, R., Loyola, D., Coldewey-Egbers, M., Kochenova, S., van Gent, J., Koukouli, M., Balis, D., Lambert, J.-C., Granville, J., and Zehner, C.: Homogenized total ozone data records from the European sensors GOME/ERS-2, SCIAMACHY/Envisat, and GOME-2/MetOp-A, *J. Geophys. Res.-Atmos.*, 119, 1639–1662, <https://doi.org/10.1002/2013JD020831>, 2014.
- Loyola, D. G., Koukouli, M. E., Valks, P., Balis, D. S., Hao, N., Van Roozendael, M., Spurr, R. J. D., Zimmer, W., Kiemle, S., Lerot, C., and Lambert, J.-C.: The GOME-2 total column ozone product: retrieval algorithm and ground-based validation, *J. Geophys. Res.*, 116, D07302, <https://doi.org/10.1029/2010JD014675>, 2011.
- McPeters, R. D., Bhartia, P. K., Haffner, D., Labow, G. J., and Flynn, L.: The version 8.6 SBUV ozone data record: An overview, *J. Geophys. Res.*, 118, 8032–8039, <https://doi.org/10.1002/jgrd.50597>, 2013.
- McPeters, R. D., Frith, S., and Labow, G. J.: OMI total column ozone: extending the long-term data record, *Atmos. Meas. Tech.*, 8, 4845–4850, <https://doi.org/10.5194/amt-8-4845-2015>, 2015 (data available at: https://acd-ext.gsfc.nasa.gov/Data_services/merged/index.html, last access: 8 February 2019).
- Naujokat, B.: An update of the observed quasi-biennial oscillation of the stratospheric winds over the tropics, *J. Atmos. Sci.*, 43, 1873–1877, [https://doi.org/10.1175/1520-0469\(1986\)043<1873:AUOTOQ>2.0.CO;2](https://doi.org/10.1175/1520-0469(1986)043<1873:AUOTOQ>2.0.CO;2), 1986 (data available at: <http://www.geo.fu-berlin.de/met/ag/strat/produkte/qbo/qbo.dat>, last access: 8 February 2019).

- Oman, L., Douglass, A., Ziemke, J., Rodriguez, J., Waugh, D., and Nielsen, J.: The ozone response to ENSO in Aura satellite measurements and a chemistry-climate simulation, *J. Geophys. Res.*, 118, 965–976, <https://doi.org/10.1029/2012JD018546>, 2013.
- Ossó, A., Sola, Y., Bech, J., and Lorente, J.: Evidence for the influence of the North Atlantic Oscillation on the total ozone column at northern low latitudes and midlatitudes during winter and summer seasons, *J. Geophys. Res.*, 116, D24122, <https://doi.org/10.1029/2011JD016539>, 2011.
- Pawson, S. and Steinbrecht, W., Charlton-Perez, A. J., Fujiwara, M., Karpechko, A. Yu., Petropavlovskikh, I., Urban, J., and Weber, M.: Update on global ozone: Past, present, and future, edited by: Violetov, V. E. and Langematz, U., Chapter 2 in *Scientific Assessment of Ozone Depletion: 2014, Global Ozone Research and Monitoring Project – Report No. 55*, World Meteorological Organization, Geneva, Switzerland, 2014.
- Pazmiño, A., Godin-Beekmann, S., Hauchecorne, A., Claud, C., Khaykin, S., Goutail, F., Wolfram, E., Salvador, J., and Quel, E.: Multiple symptoms of total ozone recovery inside the Antarctic vortex during austral spring, *Atmos. Chem. Phys.*, 18, 7557–7572, <https://doi.org/10.5194/acp-18-7557-2018>, 2018.
- Prather, M. J.: Photolysis rates in correlated overlapping cloud fields: Cloud-J 7.3c, *Geosci. Model Dev.*, 8, 2587–2595, <https://doi.org/10.5194/gmd-8-2587-2015>, 2015.
- Randel, W. J. and Thompson, A. M.: Interannual variability and trends in tropical ozone derived from SAGE II satellite data and SHADOZ ozonesondes, *J. Geophys. Res.*, 116, D07303, <https://doi.org/10.1029/2010JD015195>, 2011.
- Rieder, H. E., Frossard, L., Ribatet, M., Staehelin, J., Maeder, J. A., Di Rocco, S., Davison, A. C., Peter, T., Weihs, P., and Holawe, F.: On the relationship between total ozone and atmospheric dynamics and chemistry at mid-latitudes – Part 2: The effects of the El Niño/Southern Oscillation, volcanic eruptions and contributions of atmospheric dynamics and chemistry to long-term total ozone changes, *Atmos. Chem. Phys.*, 13, 165–179, <https://doi.org/10.5194/acp-13-165-2013>, 2013.
- Sander, S. P., Abbatt, J., Barker, J. R., Burkholder, J. B., Friedl, R. R., Golden, D. M., Huie, R. E., Kolb, C. E., Kurylo, M. J., Moortgat, G. K., Orkin, V. L., and Wine, P. H.: *Chemical Kinetics and Photochemical Data for Use in Atmospheric Studies, Evaluation No. 17, JPL Publication 10-6*, Jet Propulsion Laboratory, Pasadena, 2011, available at: <http://jpldataeval.jpl.nasa.gov> (last access 15 June 2018), 2011.
- Sioris, C. E., McLinden, C. A., Fioletov, V. E., Adams, C., Zawodny, J. M., Bourassa, A. E., Roth, C. Z., and Degenstein, D. A.: Trend and variability in ozone in the tropical lower stratosphere over 2.5 solar cycles observed by SAGE II and OSIRIS, *Atmos. Chem. Phys.*, 14, 3479–3496, <https://doi.org/10.5194/acp-14-3479-2014>, 2014.
- Solomon, S., Ivy, D. J., Kinnison, D., Mills, M. J., Neely III, R. R., and Schmidt, A.: Emergence of healing in the Antarctic ozone layer, *Science*, 30, 269–274, <https://doi.org/10.1126/science.aae0061>, 2016.
- Søvde, O. A., Prather, M. J., Isaksen, I. S. A., Berntsen, T. K., Stordal, F., Zhu, X., Holmes, C. D., and Hsu, J.: The chemical transport model Oslo CTM3, *Geosci. Model Dev.*, 5, 1441–1469, <https://doi.org/10.5194/gmd-5-1441-2012>, 2012.
- Steinbrecht, W., Claude, H., Köhler, U., and Hoinka, K. P.: Correlations between tropopause height and total ozone: Implications for long-term changes, *J. Geophys. Res.*, 103, 19183–19192, 1998.
- Steinbrecht, W., Claude, H., Köhler, U., and Winkler, P.: Interannual changes of total ozone and Northern Hemisphere circulation patterns, *Geophys. Res. Lett.*, 28, 1191–1194, 2001.
- Steinbrecht, W., Köhler, U., Claude, H., Weber, M., Burrows, J. P., and van der A, R. J.: Very high ozone columns at northern mid-latitudes in 2010, *Geophys. Res. Lett.*, 38, L06803, <https://doi.org/10.1029/2010GL046634>, 2011.
- Stone, K. A., Solomon, S., and Kinnison, D. E.: On the identification of ozone recovery, *Geophys. Res. Lett.*, 45, 5158–5165, <https://doi.org/10.1029/2018GL077955>, 2018.
- Strahan, S. E. and Douglass, A. R.: Decline in Antarctic Ozone Depletion and Lower Stratospheric Chlorine Determined From Aura Microwave Limb Sounder Observations, *Geophys. Res. Lett.*, 45, 382–390, <https://doi.org/10.1002/2017GL074830>, 2018.
- Tourpali, K., Zerefos, C. S., Balis, D. S., and Bais, A. F.: The 11-year solar cycle in stratospheric ozone: Comparison between Umkehr and SBUVv8 and effects on surface erythemal irradiance, *J. Geophys. Res.*, 112, D12306, <https://doi.org/10.1029/2006JD007760>, 2007.
- Van Roozendaal, M., Spurr, R. J. D., Loyola, D., Lerot, C., Balis, D. S., Lambert, J. C., Zimmer, W., van Gent, J., van Geffen, J., Koukoulis, M., Doicu, A., and Zehner, C.: Sixteen years of GOME/ERS-2 total ozone data: The new direct-fitting GOME Data Processor (GDP) version 5 – Algorithm description, *J. Geophys. Res.*, 117, D03305, <https://doi.org/10.1029/2011JD016471>, 2012.
- World Meteorological Organization (WMO): *Scientific Assessment of Ozone Depletion: 2014, Global Ozone Research and Monitoring Project–Report No. 55*, 416 pp., Geneva, Switzerland, 2014.
- World Ozone and Ultraviolet Radiation Data Centre (WOUDC): *Ozone*, <https://doi.org/10.14287/10000001>, 2018.
- Zerefos, C., Contopoulos, G., and G. Skalkas G. (Eds.): *Twenty Years of Ozone Decline, Proceedings of the Symposium for the 20th Anniversary of the Montreal Protocol*, Springer, Netherlands, Part of Springer Science + Business Media B. V, 470 pp., ISBN 978-90-481-2468-8, 2009.
- Zerefos, C., Kapsomenakis, J., Eleftheratos, K., Tourpali, K., Petropavlovskikh, I., Hubert, D., Godin-Beekmann, S., Steinbrecht, W., Frith, S., Sofieva, V., and Hassler, B.: Representativeness of single lidar stations for zonally averaged ozone profiles, their trends and attribution to proxies, *Atmos. Chem. Phys.*, 18, 6427–6440, <https://doi.org/10.5194/acp-18-6427-2018>, 2018.
- Zerefos, C. S.: On the quasi-biennial oscillation in stratospheric temperatures and total ozone, *Adv. Space Res.*, 2, 177–181, 1983.
- Zerefos, C. S., Bais, A. F., and Ziomas, I. C.: On the Relative Importance of Quasi-Biennial Oscillation and El Niño/Southern Oscillation in the Revised Dobson Total Ozone Records, *J. Geophys. Res.*, 97, 10135–10144, 1992.
- Zerefos, C. S., Tourpali, K., and Bais, A. F.: Further studies on possible volcanic signal to the ozone layer, *J. Geophys. Res.*, 99, 25741–25746, 1994.

Zerefos, C. S., Tourpali, K., Isaksen, I. S. A., and Schuurmans, C. J. E.: Long term solar induced variation in total ozone, stratospheric temperatures and the tropopause, *Adv. Space Res.*, *27*, 1943–1948, 2001.

Article

Possible Effects of Greenhouse Gases to Ozone Profiles and DNA Active UV-B Irradiance at Ground Level

Kostas Eleftheratos ^{1,2,*}, John Kapsomenakis ³, Christos S. Zerefos ^{2,3,4}, Alkiviadis F. Bais ⁵ , Ilias Fountoulakis ^{5,6} , Martin Dameris ⁷, Patrick Jöckel ⁷ , Amund S. Haslerud ⁸, Sophie Godin-Beekmann ⁹, Wolfgang Steinbrecht ¹⁰, Irina Petropavlovskikh ¹¹, Colette Brogniez ¹², Thierry Leblanc ¹³, J. Ben Liley ¹⁴ , Richard Querel ¹⁴ and Daan P. J. Swart ¹⁵ 

¹ Department of Geology and Geoenvironment, National and Kapodistrian University of Athens, 15784 Athens, Greece

² Center for Environmental Effects on Health, Biomedical Research Foundation of the Academy of Athens, 11527 Athens, Greece; zerefos@geol.uoa.gr

³ Research Centre for Atmospheric Physics and Climatology, Academy of Athens, 10680 Athens, Greece; johnkaps@geol.uoa.gr

⁴ Navarino Environmental Observatory (N.E.O), 24001 Messinia, Greece

⁵ Department of Physics, Aristotle University of Thessaloniki, 54124 Thessaloniki, Greece; abais@auth.gr (A.F.B.); iliasnf@auth.gr (I.F.)

⁶ Aosta Valley Regional Environmental Protection Agency (ARPA), 11020 Saint-Christophe, Italy

⁷ Deutsches Zentrum für Luft- und Raumfahrt, Institut für Physik der Atmosphäre, 82234 Oberpfaffenhofen, Germany; Martin.Dameris@dlr.de (M.D.); Patrick.Joeckel@dlr.de (P.J.)

⁸ Cicero Center for International Climate Research (CICERO), 0318 Oslo, Norway; meteorologen@gmail.com

⁹ Laboratoire Atmosphère Milieux Observations Spatiales, Centre National de la Recherche Scientifique, Université de Versailles Saint-Quentin-en-Yvelines, Université Pierre et Marie Curie, 78284 Guyancourt, France; sophie.godin-beekmann@latmos.ipsl.fr

¹⁰ Deutscher Wetterdienst, 82383 Hohenpeißenberg, Germany; Wolfgang.Steinbrecht@dwd.de

¹¹ Cooperative Institute for Research in Environmental Sciences, University of Colorado, Boulder, CO 80301, USA; irina.petro@noaa.gov

¹² Univ. Lille, CNRS, UMR 8518 - Laboratoire d'Optique Atmosphérique, F-59000 Lille, France; colette.brogniez@univ-lille.fr

¹³ Jet Propulsion Laboratory, California Institute of Technology, Wrightwood, CA 92397, USA; thierry.leblanc@jpl.nasa.gov

¹⁴ National Institute of Water & Atmospheric Research (NIWA), 9377 Lauder, New Zealand; Ben.Liley@niwa.co.nz (J.B.L.); Richard.Querel@niwa.co.nz (R.Q.)

¹⁵ Center for Environmental Quality, National Institute for Public Health and the Environment (RIVM), 3720 BA Bilthoven, The Netherlands; daan.swart@rivm.nl

* Correspondence: kelef@geol.uoa.gr; Tel.: +30-210-7274133

Received: 1 February 2020; Accepted: 18 February 2020; Published: 26 February 2020



Abstract: In this paper, we compare model calculations of ozone profiles and their variability for the period 1998 to 2016 with satellite and lidar profiles at five ground-based stations. Under the investigation is the temporal impact of the stratospheric halogen reduction (chemical processes) and increase in greenhouse gases (i.e., global warming) on stratospheric ozone changes. Attention is given to the effect of greenhouse gases on ultraviolet-B radiation at ground level. Our chemistry transport and chemistry climate models (Oslo CTM3 and EMAC CCM) indicate that (a) the effect of halogen reduction is maximized in ozone recovery at 1–7 hPa and observed at all lidar stations; and (b) significant impact of greenhouse gases on stratospheric ozone recovery is predicted after the year 2050. Our study indicates that solar ultraviolet-B irradiance that produces DNA damage would increase after the year 2050 by +1.3% per decade. Such change in the model is driven by a significant

decrease in cloud cover due to the evolution of greenhouse gases in the future and an insignificant trend in total ozone. If our estimates prove to be true, then it is likely that the process of climate change will overwhelm the effect of ozone recovery on UV-B irradiance in midlatitudes.

Keywords: ozone; UV-B irradiance; halogens; greenhouse gases; effects

1. Introduction

Depletion and recovery of stratospheric ozone and climate change affect solar ultraviolet (UV) radiation [1]. Changes in stratospheric ozone depend strongly on the evolution of ozone-depleting substances (ODS). ODS are anthropogenic halogen-source gases composed of chlorine and bromine atoms that are entrained in the stratosphere in the tropics, transported through Brewer–Dobson circulation to the middle and high latitudes. They destroy stratospheric ozone globally [2]. The emissions of anthropogenic halogens are controlled by the Montreal Protocol, which was adopted on 15 September 1987, with the aim to eliminate the anthropogenic substances that deplete the ozone layer. The effectiveness of the protocol, 30 years after the agreement, is summarized in the recent ozone assessment report [3]. The total chlorine and bromine amounts (natural and anthropogenic) peaked in 1993 and 1998, respectively, and had declined in 2016 by 10% and 11%, respectively.

Apart from changes in stratospheric ozone due to anthropogenic ODS, other important factors that may impact the future UV radiation levels are alteration in cloudiness, aerosols and surface reflectivity due to climate change. In the long-term, 1/3 of the observed UV-B trend in midlatitudes is attributed to the total column ozone change; the remaining 2/3 is attributed to the combined effects of cloudiness and aerosol changes [4,5]. Changes in aerosols are expected to dominate changes in UV radiation over highly polluted areas in the future. Over snow- and ice-covered areas, changes in UV radiation will depend on changes in albedo. The estimate of future UV radiation levels is uncertain, because of the assumptions in defining the development of these variables over time [6].

It is well-known that stratospheric ozone was decreasing since the 1980s, until the reverse of the trend emerged in the late 1990s that marks a turning point in the four-decade history of stratospheric ozone [7,8]. It has been shown in recent literature, e.g., [7,9–11], that ozone in the upper stratosphere follows an upward trend, in contrast to negative, but smaller trends are seen in the lower stratosphere. The behavior of stratospheric ozone after the mid-1990s is dependent on (a) reduction in atmospheric halogens and (b) the slowing of ozone-depleting chemical processes due to the cooling of the stratosphere, which is associated with increases in GHGs. In the lower stratosphere, ozone modulations are strongly affected by the dynamical transport processes.

In this study, we provide observational and modeling results about ozone trends in different stratospheric layers. We present vertical ozone trends from measurements (lidar and solar backscatter ultraviolet radiometer, SBUV) in middle and low latitudes, after 1997, and we evaluate the performance of state-of-the-art chemistry transport and chemistry climate model simulations to reproduce the observed ozone profile trends. The analysis includes the impact of stratospheric halogen reduction on stratospheric ozone trends with the Oslo chemistry transport model (CTM) and the impact of increasing GHGs on stratospheric ozone changes with the European Centre for Medium-Range Weather Forecasts–Hamburg (ECHAM)/Modular Earth Submodel System (MESSy) Atmospheric Chemistry (EMAC) chemistry climate model (CCM). The chemistry transport simulations with the Oslo CTM3 are available for the present, while the chemistry climate simulations with the EMAC CCM are available for the past, present and future. Use was made of the latest simulations of EMAC with emphasis at individual lidar stations. Worth noting are the similarities of the two different models as to their results for the present, which contributes to the novelty of our work.

The EMAC simulations are also used to determine the impact of increasing GHGs on solar ultraviolet-B irradiance that produce DNA damage. So far, the results of these EMAC simulations

have not been used for such an exercise. In the past, results of the old EMAC simulations were used for a similar study (see Bais et al., 2011), which attempted to project UV irradiance in the future with the inclusion of effects from clouds. They showed that the annually mean surface erythemal solar irradiance in the 2090s will be on average ~3% lower at midlatitudes and marginally higher (~1%) in the tropics. Here, we revisit the issue of trends in UV in the future, using the most recent CCM simulations of the EMAC model. We estimate a possible increase in UV-B irradiance in midlatitudes in the future, which was not estimated by Bais et al. [12]. The results of a possible increase in surface UV-B irradiance in midlatitudes after the middle of this century is what makes results of this study different from previous ones about the same topic. Previous estimates showed that UV will continue to decrease toward 2100, particularly in the Northern Hemisphere, because of continuing increases in total ozone due to circulation changes induced by the increasing GHG concentrations [12]. Here, we show that total ozone will not continue to increase as we reach the end of this century and that surface UV-B irradiance will likely increase because of cloud decrease induced by climate change. If our estimates prove to be true, then it is likely that the process of climate change will overwhelm the effect of ozone recovery on UV-B irradiance in midlatitudes.

2. Data and Modeling

2.1. Lidar

Monthly mean ozone profiles from lidar instruments were obtained by averaging daily profiles from the Network for the Detection of Atmospheric Composition Change (NDACC, www.ndacc.org) database at <ftp://ftp.cpc.ncep.noaa.gov/ndacc/station/> (last access: 12 September 2018) [13–15]. For all stations, the profiles from the (monthly) NASA-Ames files are used. The lidar measurements are given as number density (molecules cm^{-3}) versus altitude [16]. From these measurements the column densities in matm cm (DU) were calculated for 3 layers (3–7, 7–30 and 30–100 hPa), representing the upper stratosphere, middle stratosphere and lower stratosphere, respectively, according to the methodology described by Zerefos et al. [7]. The list of 5 lidar stations analyzed in this study is given in Table 1. The period of analysis is January 1998 to December 2016.

Table 1. Geographical data of stations with long-term ozone profile measurements from lidars analyzed in this study.

Station	Latitude	Longitude	Elevation	Starting Year
Hohenpeissenberg (HHP)	47.8° N	11.0° E	975 m	1987
Haute Provence (OHP)	43.9° N	5.7° E	674 m	1985
Table Mountain (TMO)	34.4° N	117.7° W	2285 m	1989
Mauna Loa (MLO)	19.5° N	155.6° W	3391 m	1993
Lauder (LAU)	45.0° S	169.7° E	370 m	1994

2.2. SBUV/2

In our analysis, the daily solar backscatter ultraviolet radiometer 2 (SBUV/2) ozone profile data, selected to match the lidar stations' locations, are used for the post-Pinatubo period, 1998–2016. Stratospheric ozone data are grouped into 3 layers: upper (1–7 hPa), middle (7–30 hPa) and lower stratosphere (30–100 hPa). In addition, we analyzed total ozone data from SBUV records selected over the five lidar stations. Total ozone changes were analyzed in relation to variability in the tropopause pressure (TPP), where TPP data were selected from the National Center for Environmental Prediction (NCEP) reanalysis data [17] matched to the station location. During the period under study, data are available from the following SBUV instruments: NOAA-9 SBUV/2 (02/1985–01/1998), NOAA-11 SBUV/2 (01/1989–03/2001), NOAA-14 SBUV/2 (03/1995–09/2006), NOAA-16 SBUV/2 (10/2000–05/2014), NOAA-17 SBUV/2 (08/2002–3/2013), NOAA-18 SBUV/2 (07/2005–11/2012) and NOAA-19 SBUV/2

(03/2009–present). For every day of analyses, a daily value is calculated by averaging the measurements from all available SBUV instruments, and then the monthly mean is calculated from the daily values [7].

2.3. Oslo Chemistry Transport Model (CTM3)

The Oslo CTM3 is a global chemistry transport model with comprehensive tropospheric and stratospheric chemistry [18]. The model has traditionally been driven by 3-hourly meteorological forecast data from the European Centre for Medium-Range Weather Forecasts (ECMWF) Integrated Forecast System (IFS) model, whereas, in this study, we applied the output of the OpenIFS model to drive the CTM (<https://software.ecmwf.int/wiki/display/OIFS/>), cycle 38r1, which is an improvement from Søvde et al. [18]. Photochemistry was calculated, using Fast-JX version 6.7c [19] and chemical kinetics from the Jet Propulsion Laboratory (JPL) 2011 [20]. The horizontal resolution of the model is $2.25^\circ \times 2.25^\circ$, and it has a 60-layer vertical resolution, spanning from the surface up to 0.1 hPa. The main simulation is denoted FULL, updating emissions and winds from the ECMWF-driven meteorology. We note here that the emissions database used as input to the model has not been updated since the year 2011, and therefore the model retains constant halogens and bromine at 2011 levels after 2011, with monthly variation. We also apply a perturbation simulation, using fixed halogens at 1998 levels, namely HAL98. The period of CTM simulations is January 1998 to December 2016.

2.4. EMAC Chemistry Climate Model (CCM)

The EMAC CCM is the European Centre for Medium-Range Weather Forecasts–Hamburg (ECHAM)/Modular Earth Submodel System (MESSy) Atmospheric Chemistry (EMAC) model used to study the chemistry and dynamics of the atmosphere [21]. We analyzed the hindcast simulations with specified dynamics, i.e., the model is operated with sea-surface temperatures and sea-ice concentrations taken from ERA-Interim reanalysis data. In addition, the model-simulated vorticity, divergence, temperature and the logarithm of the surface pressure are “nudged” by Newtonian relaxation toward the ERA-Interim data. The used resolution is $2.8^\circ \times 2.8^\circ$ in latitude and longitude, with 90 model levels reaching up to 0.01 hPa (about 80 km). The model employs two scenarios for estimating the uncertainties of the precursor emissions/boundary conditions after the year 2011, known as representative concentration pathways (RCPs), the RCP-8.5 and RCP-6.0 pathways (RCP-6.0 assumes that GHG emissions will peak around 2080; RCP-8.5 assumes no peak before 2100). We used the ozone simulation built upon the RCP-6.0 pathway, namely the SC1SD-base-02 simulation. The period of simulations is January 2000 to July 2018.

The effect of increasing GHGs on long-term ozone and UV-B radiation trends was studied by comparing two free-running hindcasts and projection simulations: a reference simulation with background GHGs mixing ratios, as embedded in the simulated sea-surface temperatures and sea-ice concentrations, which were used as input to the model (RC2-base-04) [17], and the same simulation with fixed GHGs at 1960 levels (SC2-fGHG-01) [22]. The UV-B radiation calculated by the photolysis scheme (JVAL) [23] was weighted by DNA damage potential [24]. Total cloud cover was determined for the RC2-base-04 and SC2-fGHG-01 simulations by summing the cloud-cover data for model levels from 1000 to 200 hPa.

2.5. NDACC UV Irradiance Data

The DNA-active UV-B irradiance data from the EMAC model were evaluated against ground-based measurements from the NDACC database. The NDACC data repository, <ftp://ftp.cpc.ncep.noaa.gov/ndacc/station/>, provides UV spectral irradiance data for three of five stations under study, namely Haute Provence, Mauna Loa and Lauder. We analyzed the DNA-weighted UV irradiance data at these three stations. These sites are among those possessing high-quality long-term measurements of UV irradiance [25]. We calculated monthly mean irradiances from noon averages for these three stations (average of measurements ± 45 min around local noon), and compared them with the DNA UV-B irradiances from the SC1SD-base-02 simulation. We found that the Pearson’s correlation coefficients

between the modeled and the ground-based data are all highly statistically significant (>99%). We report here the results from the regression analyses between the modeled and observed deseasonalized DNA UV data, as follows: (a) Haute Provence: $R = +0.574$, slope = +0.452, error = 0.065, t -value = 6.978, p -value < 0.0001, $N = 101$ (monthly data pairs between January 2009 and July 2018), (b) Mauna Loa: $R = +0.576$, slope = +0.646, error = 0.063, t -value = 10.227, p -value < 0.0001, $N = 213$ (monthly data pairs between January 2000 and December 2017), (c) Lauder: $R = +0.527$, slope = +0.324, error = 0.036, t -value = 8.978, p -value < 0.0001, $N = 212$ (monthly data pairs between January 2000 and December 2017).

2.6. Methodology

We use multivariate linear regression (MLR) analysis to remove known natural and dynamical variability from ozone variability. The MLR statistical model includes QBO, SOLAR, ENSO, AO/AAO, tropopause and AOD terms, as described by Zerefos et al. [7]. The seasonal cycle was removed from the data before applying the MLR analysis, by subtracting the long-term monthly mean (1998–2016) pertaining to the same calendar month (i.e., (monthly value–long-term monthly mean)/long-term monthly mean $\times 100$). These values form the deseasonalized data in percent, which were used in the MLR model. The residuals from the MLR model, free from natural fluctuations (seasonal, QBO, SOLAR, etc.) are used to calculate the stratospheric and total ozone trends for the period of 1998–2016. All trends were calculated by using percentages, so that the results at each atmospheric layer and site are comparable to each other. First, we did the regression for each lidar station separately, and then we calculated the average of anomaly percentages from the regression residuals. In all figures, a low-pass filter with weights 1-4-6-4-1 is applied to the residuals.

3. Results and Discussion

3.1. Stratospheric Ozone Trends

Trends in the vertical distribution of ozone were compared for the period of 1998–2016, from observations and model simulations. Results are presented in Table 2 and were selected to spatially match the individual lidar stations featured in this study. Trends from CTM3 simulations show excellent agreement with those measured by SBUV and lidars in the upper stratosphere, except at Mauna Loa, where the lidar data show negative trends. In the middle stratosphere, most trends are statistically insignificant. In the lower stratosphere, most datasets reveal negative ozone trends, except for analyses of the lidar data at Hohenpeissenberg, which show positive but statistically insignificant trends.

Examples of the different trends observed in the upper stratosphere (positive trends) and lower stratosphere (negative trends) are presented in Figure 1. The upper panel shows ozone anomalies over Hohenpeissenberg (HHP), Haute Provence (OHP) and Table Mountain (TMO), and the lower panel shows anomalies at Mauna Loa (MLO) and Lauder (LAU). We remind the reader that natural variability was removed from the data, as described in Section 2.6. As can be seen from Figure 1, the model simulations indicate an increase in ozone in the upper stratosphere, above 7 hPa, and a decrease in the lower stratosphere, between 30 and 100 hPa, in very good agreement with results from the SBUV satellite data. A look into 5° zonal averages from model and satellite data encompassing the stations under study reveals a similar picture too (not shown).

Table 2. Estimated trends (%/decade) in the vertical distribution of ozone for the period of 1998–2016 from observations and model simulations at (a) Hohenpeissenberg, (b) Haute Provence, (c) Table Mountain, (d) Mauna Loa, (e) Lauder and (f) 5 station mean, after removing the seasonal and known natural variability. FULL refers to the main simulation; HAL98 refers to the simulation with fixed halogens at 1998 levels. For lidars, the upper stratospheric layers are confined between 3 and 7 hPa. Asterisks denote statistical significance at the 99% confidence level.

(a) Hohenpeissenberg (47.8° N, 11.0° E)					
Layer	Oslo CTM3 ¹		SBUV (v8.6) ²	EMAC CCM ³ (SC1SD_02)	Lidar
	FULL	HAL98			
1–7 hPa	1.2 ± 0.3 *	0.6 ± 0.3	1.9 ± 0.3 *	1.5 ± 0.3 *	1.7 ± 0.5 *
7–30 hPa	−0.3 ± 0.4	−0.1 ± 0.4	0.4 ± 0.4	0.5 ± 0.4	1.8 ± 0.6 *
30–100 hPa	−1.3 ± 0.5	−1.8 ± 0.5 *	−1.0 ± 0.5	1.0 ± 0.6	0.7 ± 0.7
(b) Haute Provence (43.9° N, 5.7° E)					
Layer	Oslo CTM3		SBUV (v8.6)	EMAC CCM (SC1SD_02)	Lidar
	FULL	HAL98			
1–7 hPa	1.2 ± 0.3 *	0.7 ± 0.3	1.7 ± 0.3 *	1.6 ± 0.3 *	0.4 ± 0.5
7–30 hPa	−0.6 ± 0.4	−0.4 ± 0.4	0.0 ± 0.4	−0.1 ± 0.4	0.3 ± 0.5
30–100 hPa	−1.3 ± 0.5	−1.8 ± 0.5 *	−1.0 ± 0.5	0.4 ± 0.7	−0.1 ± 0.7
(c) Table Mountain (34.4° N, 117.7° W)					
Layer	Oslo CTM3		SBUV (v8.6)	EMAC CCM (SC1SD_02)	Lidar
	FULL	HAL98			
1–7 hPa	1.3 ± 0.3 *	0.8 ± 0.3 *	1.6 ± 0.2 *	2.0 ± 0.3 *	0.5 ± 0.8
7–30 hPa	−0.9 ± 0.3 *	−0.8 ± 0.3 *	−0.7 ± 0.3	−0.4 ± 0.3	0.8 ± 0.7
30–100 hPa	−3.6 ± 0.6 *	−4.0 ± 0.6 *	−1.4 ± 0.5 *	−0.9 ± 0.8	−2.1 ± 1.6
(d) Mauna Loa (19.5° N, 155.6° W)					
Layer	Oslo CTM3		SBUV (v8.6)	EMAC CCM (SC1SD_02)	Lidar
	FULL	HAL98			
1–7 hPa	0.8 ± 0.2 *	0.4 ± 0.2	1.6 ± 0.2 *	1.5 ± 0.2 *	−0.6 ± 0.3
7–30 hPa	−0.7 ± 0.3	−0.7 ± 0.3	−0.7 ± 0.3	0.0 ± 0.3	−1.0 ± 0.4
30–100 hPa	−4.3 ± 0.8 *	−4.7 ± 0.8 *	−1.1 ± 0.4	−1.1 ± 0.9	−3.4 ± 0.8 *
(e) Lauder (45.0° S, 169.7° E)					
Layer	Oslo CTM3		SBUV (v8.6)	EMAC CCM (SC1SD_02)	Lidar
	FULL	HAL98			
1–7 hPa	−0.1 ± 0.3	−0.5 ± 0.3	0.4 ± 0.2	0.5 ± 0.3	0.6 ± 0.5
7–30 hPa	−0.4 ± 0.3	−0.3 ± 0.3	0.0 ± 0.4	0.4 ± 0.4	0.7 ± 0.7
30–100 hPa	−0.1 ± 0.5	−0.5 ± 0.5	−0.2 ± 0.4	−1.1 ± 0.5	0.5 ± 0.9
(f) 5 Station Mean					
Layer	Oslo CTM3		SBUV (v8.6)	EMAC CCM (SC1SD_02)	Lidar
	FULL	HAL98			
1–7 hPa	0.9 ± 0.2 *	0.4 ± 0.2	1.4 ± 0.2 *	1.4 ± 0.2 *	0.4 ± 0.2
7–30 hPa	−0.6 ± 0.2 *	−0.5 ± 0.2	−0.2 ± 0.2	0.1 ± 0.2	0.1 ± 0.3
30–100 hPa	−2.1 ± 0.3 *	−2.6 ± 0.3 *	−1.0 ± 0.3 *	−0.3 ± 0.4	−1.3 ± 0.4 *

¹ Oslo chemistry transport model 3; ² Solar backscatter ultraviolet radiometer (version 8.6); ³ EMAC chemistry climate model.

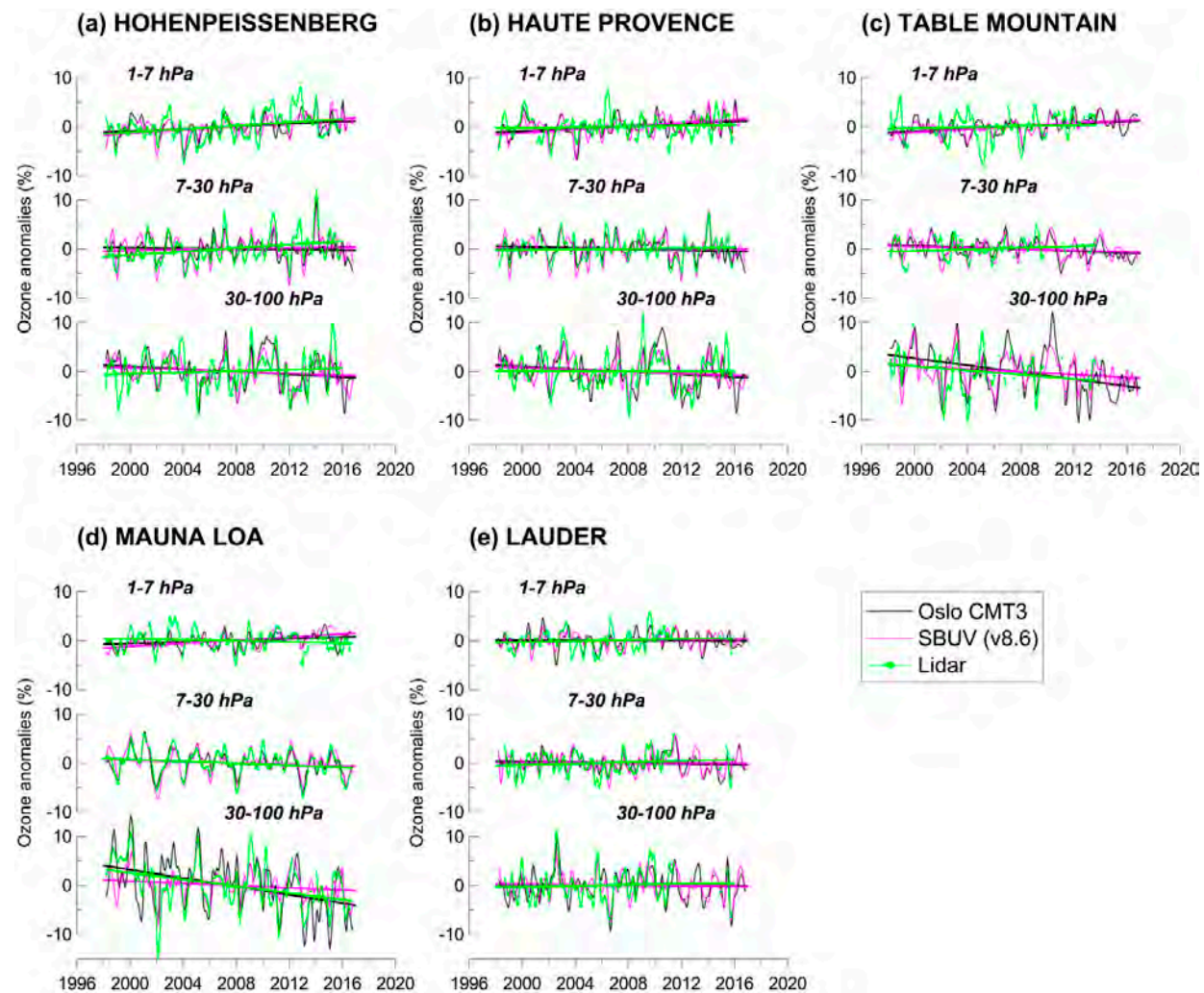


Figure 1. Ozone trends in the upper stratosphere (1–7 hPa), middle stratosphere (7–30 hPa) and lower stratosphere (30–100 hPa), from lidar measurements, SBUV (v8.6) satellite data and Oslo CTM3 simulations over (a) Hohenpeissenberg, (b) Haute Provence and (c) Table Mountain (upper panel), and over (d) Mauna Loa and (e) Lauder (lower panel). Seasonal and natural proxies are removed. For lidars, the upper stratospheric layers are confined between 3 and 7 hPa.

Figure 2 summarizes the comparison of model simulations (Oslo CTM3 and EMAC CCM) with satellite and lidar residuals averaged at all stations under study. The figure shows results for the upper, middle and lower stratosphere for the period of 1998 to 2016. The correlation coefficients (Pearson product-moment correlation), R , between the four datasets are shown in Table 3 for the five stations' mean. Results for each station separately are provided in Supplementary Tables S1–S5. Statistical significance of R was determined by using the t -test formula for the correlation coefficient, with $n-2$ degrees of freedom, as by Zerefos et al. [7]. All R are found to be statistically significant at the 99% confidence level or greater. There are higher correlations at some stations, and lower at others, but the general picture of correlations is given in Table 3.

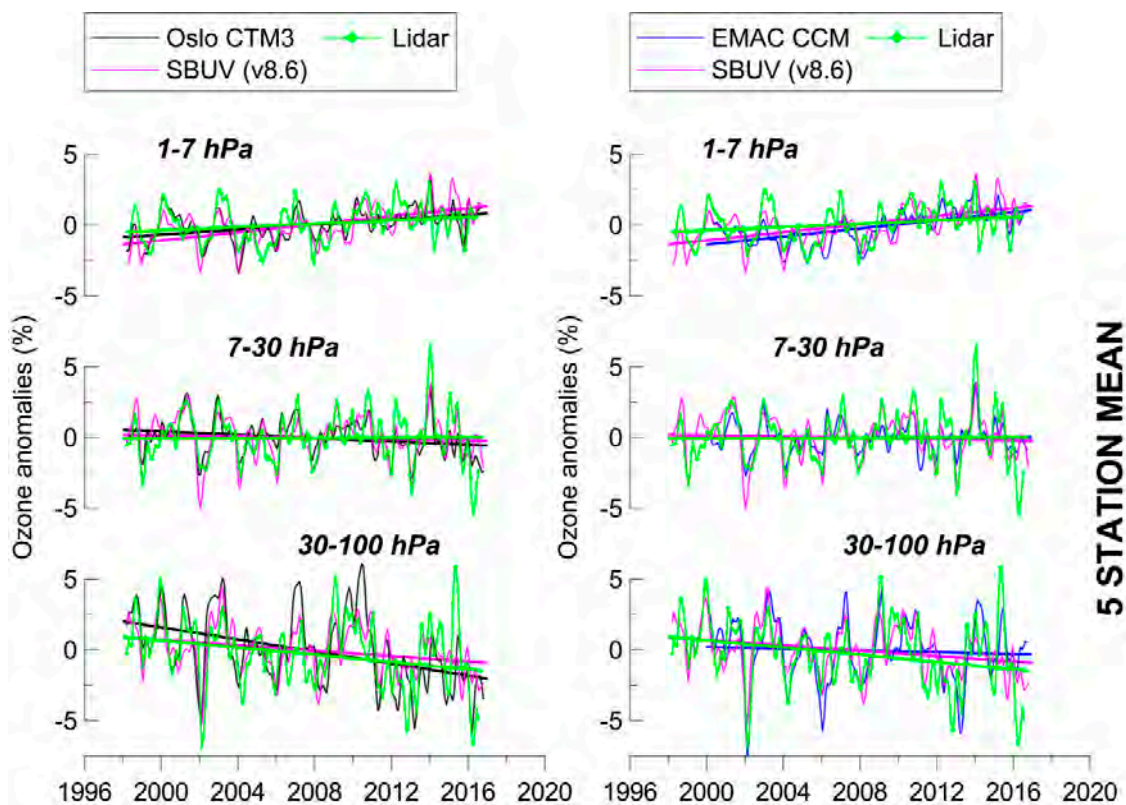


Figure 2. Comparison of CTM ozone simulations (left) and CCM (SC1SD-base-02) ozone simulations (right) with SBUV observations and lidar measurements. Shown are ozone anomalies averaged at five lidar stations (HHP–OHP–TMO–MLO–LAU), after removing seasonal and other known natural variability. For lidars, the upper stratospheric layers are confined between 3 and 7 hPa.

We assessed the effect of natural variability on ozone variability. As can be seen from Figure 2, the highest ozone variability is observed in the lower stratosphere, indicative of the strong dynamical influences in that part of the atmosphere related to the QBO, SOLAR, ENSO, AO, tropopause and AOD proxies. The upper stratosphere is much less affected by dynamics, and this fact is evident in both the model and SBUV data. We analyzed the ozone variability in the upper stratosphere, both with and without removing the dynamical proxies. We found that the two estimates do not statistically significantly differ. For example, the 1σ of ozone variability in the upper stratosphere at HHP–OHP–TMO is estimated to be 2.3% after removing the seasonal variability, and 2.2% after removing both the seasonal and dynamical variability related to the QBO, SOLAR, ENSO, AO, tropopause and AOD proxies. In Mauna Loa, ozone variability is estimated to be 1.9% (1σ) after removing the seasonal cycle, and 1.6% after removing both the seasonal and dynamical proxies, while in Lauder, the respective numbers are 2.5% and 2.0%. In all cases, the differences were small, i.e., less than 0.5%. On the other hand, the 1σ of ozone variability is higher in the lower stratosphere than

in the upper stratosphere. Indicative values are 3.1% at HHP–OHP–TMO, 3.7% at MLO and 3.5% at LAU after removing the seasonal cycle and dynamical proxies, respectively, compared to 3.9% at HHP–OHP–TMO, 4.4% at MLO and 4.8% at Lauder without removing the dynamical proxies.

Table 3. Statistics of correlations between ozone from Oslo CTM3, EMAC CCM (SC1SD-base-02), SBUV (v8.6) and average lidar data anomalies at five stations in the: (a) upper stratosphere (1–7 hPa), (b) middle stratosphere (7–30 hPa) and (c) lower stratosphere (30–100 hPa). Seasonal and other known natural variability were removed from the data. For lidars, the upper stratospheric layers are confined between 3 and 7 hPa.

(a) 1–7 hPa	Correlation Coefficient	Intercept (%)	Slope	Error *	t-Value	p-Value	N
CTM3 and SBUV	0.78	0.002	0.700	0.038	18.500	<0.0001	227
CTM3 and Lidar	0.51	−0.040	0.395	0.044	8.912	<0.0001	225
CTM3 and CCM	0.74	0.230	0.715	0.045	15.857	<0.0001	204
CCM and SBUV	0.72	−0.251	0.682	0.047	14.571	<0.0001	203
CCM and Lidar	0.48	−0.207	0.369	0.048	7.688	<0.0001	201
SBUV and Lidar	0.41	−0.038	0.350	0.053	6.640	<0.0001	224
(b) 7–30 hPa							
CTM3 and SBUV	0.81	0.0007	0.706	0.034	20.560	<0.0001	227
CTM3 and Lidar	0.77	0.026	0.523	0.029	18.064	<0.0001	225
CTM3 and CCM	0.88	0.018	1.008	0.039	26.015	<0.0001	204
CCM and SBUV	0.81	0.016	0.643	0.033	19.707	<0.0001	203
CCM and Lidar	0.77	−0.024	0.459	0.027	16.788	<0.0001	201
SBUV and Lidar	0.71	0.033	0.558	0.037	15.120	<0.0001	224
(c) 30–100 hPa							
CTM3 and SBUV	0.70	0.008	0.975	0.066	14.859	<0.0001	227
CTM3 and Lidar	0.55	0.179	0.501	0.051	9.834	<0.0001	225
CTM3 and CCM	0.62	−0.155	0.706	0.063	11.129	<0.0001	204
CCM and SBUV	0.67	0.056	0.841	0.066	12.758	<0.0001	203
CCM and Lidar	0.55	0.142	0.450	0.049	9.255	<0.0001	201
SBUV and Lidar	0.62	0.131	0.407	0.035	11.673	<0.0001	224

* Error, *t*-value and *p*-value refer to slope.

Interestingly, the opposite trends seen in the vertical distribution of ozone have resulted in insignificant trends in total ozone after 1997. Reanalysis data from NCEP reveal insignificant trends in tropopause pressures as well. The results are presented in Figure 3, which shows total ozone and tropopause pressure variability at the five stations under study. The respective linear trends are presented in Table 4. Total ozone in the period of 1998–2016 shows small negative statistically insignificant trends.

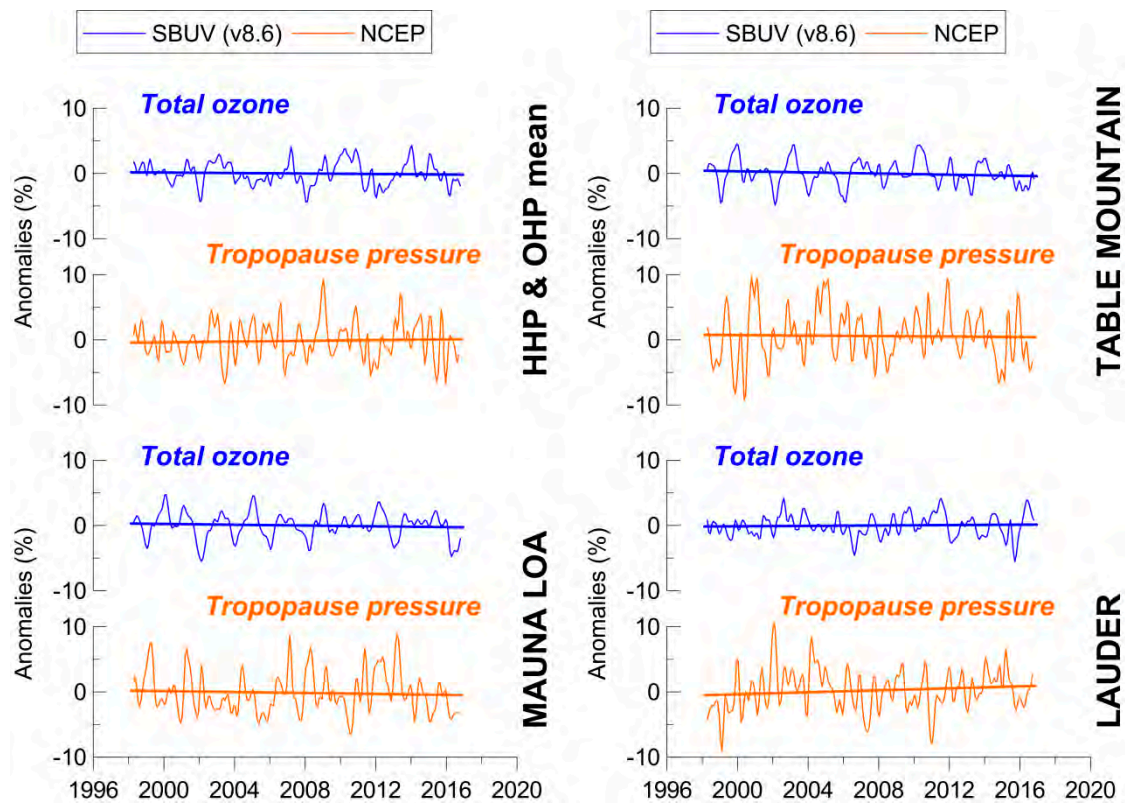


Figure 3. Time series of total ozone and tropopause pressure anomalies at lidar stations: Hohenpeissenberg and Haute Provence (**upper left**), Table Mountain (**upper right**), Mauna Loa (**lower left**) and Lauder (**lower right**).

Table 4. Trends (% per decade) in total ozone from SBUV data and tropopause pressure from NCEP reanalysis data for the period 1998–2016, at five lidar stations, after removing variability related to the seasonal cycle and dynamical proxies.

	Total Ozone (SBUV v8.6)			Tropopause Pressure (NCEP)		
	Trend (% dec ⁻¹)	<i>t</i> -Value	N	Trend (% dec ⁻¹)	<i>t</i> -Value	N
HHP	-0.16 ± 0.33	-0.482	228	-0.06 ± 0.67	-0.089	228
OHP	-0.22 ± 0.32	-0.696	228	0.65 ± 0.67	0.964	228
TMO	-0.42 ± 0.31	-1.349	228	-0.17 ± 0.79	-0.211	228
MLO	-0.26 ± 0.28	-0.954	228	-0.46 ± 0.58	-0.796	228
LAU	0.15 ± 0.30	0.502	228	0.77 ± 0.62	1.247	228

We note here the correlation between the vertical ozone distribution and the total column ozone. The largest R between the layer-mean ozone and the total column ozone is found in the middle and lower stratosphere, which contain the highest ozone concentrations. We indicate here the contribution of each layer to total ozone in terms of partial ozone columns, based on model simulations, as follows: (a) upper stratosphere (1–7 hPa); average ozone amount 33 DU (10% of total ozone), (b) middle stratosphere (7–30 hPa); average ozone amount 120 DU (36% of total ozone), (c) lower stratosphere (30–100 hPa); average ozone amount 109 DU (33% of total ozone), (d) upper troposphere/lower stratosphere (100–300 hPa); average ozone amount 36 DU (11% of total ozone), and (e) troposphere (300–1000 hPa); average ozone amount 33 DU (10% of total ozone).

The results from the correlation analyses are presented in Table 5, which shows the correlation coefficients, R , between layer-mean ozone and total ozone, at the stations under study from SBUV satellite data and Oslo CTM3 simulations. The magnitude of correlations gives a measure of the influence of variability of each stratospheric layer to the variability of total ozone. The smaller the correlation, the smaller the influence is. As expected, the upper part of the stratosphere has a small contribution to the short-term fluctuations of total ozone compared to its middle and lower parts, which contribute the most to total ozone. We remind the reader that the correlations are based on residual data, i.e., data after removing seasonal variability and dynamical proxies, but not the trend component. Long-term trends contribute to the correlations of Table 5, and therefore the differences between results based on SBUV and CTM total ozone data may be related to differences in their long-term trends.

Table 5. Correlation coefficients between layer-mean ozone and total ozone from model (Oslo CTM3) and satellite (SBUV v8.6) data in (a) the upper stratosphere, (b) middle stratosphere and (c) the lower stratosphere at 5 lidar stations, after removing seasonal and known natural variability. Significance at 99.9% is denoted by asterisks.

Correlation Coefficients 1998–2016				
(a) Upper Stratosphere (1–7 hPa) and Total Ozone Correlation				
	1–7 hPa (CTM3)		1–7 hPa (SBUV)	
	Total ozone (SBUV)	Total ozone (CTM3)	Total ozone (SBUV)	Total ozone (CTM3)
Hohenpeissenberg	0.24 *	0.28 *	0.31 *	0.31 *
Haute Provence	0.22 *	0.23 *	0.30 *	0.28 *
Table Mountain	0.34 *	0.19	0.33 *	0.13
Mauna Loa	0.15	0.09	0.14	−0.04
Lauder	0.04	0.04	0.28 *	0.26 *
(b) Middle Stratosphere (7–30 hPa) and Total Ozone Correlation				
	7–30 hPa (CTM3)		7–30 hPa (SBUV)	
	Total ozone (SBUV)	Total ozone (CTM3)	Total ozone (SBUV)	Total ozone (CTM3)
Hohenpeissenberg	0.58 *	0.65 *	0.57 *	0.57 *
Haute Provence	0.55 *	0.64 *	0.60 *	0.60 *
Table Mountain	0.50 *	0.59 *	0.70 *	0.64 *
Mauna Loa	0.67 *	0.67 *	0.89 *	0.73 *
Lauder	0.65 *	0.66 *	0.75 *	0.69 *
(c) Lower Stratosphere (30–100 hPa) and Total Ozone Correlation				
	30–100 hPa (CTM3)		30–100 hPa (SBUV)	
	Total ozone (SBUV)	Total ozone (CTM3)	Total ozone (SBUV)	Total ozone (CTM3)
Hohenpeissenberg	0.81 *	0.87 *	0.90 *	0.75 *
Haute Provence	0.76 *	0.86 *	0.90 *	0.72 *
Table Mountain	0.73 *	0.88 *	0.92 *	0.77 *
Mauna Loa	0.53 *	0.79 *	0.85 *	0.73 *
Lauder	0.66 *	0.85 *	0.91 *	0.74 *

3.2. Effect of Chemistry on Ozone Trends

With CTM3, we were able to quantify the effect of reducing halogen emissions on the upper- and the lower-stratospheric ozone trends. Simulations with the Oslo CTM3 model (black line) indicate that ozone in the upper stratosphere increased slowly from 1998 to 2016, by about 1% per decade, in agreement with SBUV satellite data. A separate simulation using fixed halogen emissions at 1998 levels (orange line) was performed to evaluate the effect of reducing ozone-depleting substances on the vertical ozone trends. The results are presented in Figure 4. The trends from the two model simulations (full vs. fixed halogens) were found to differ by 0.5% per decade. This difference is attributed to the reduction of halogen emissions in the atmosphere. In the lower stratosphere, the model reveals statistically significantly negative ozone trends of about -2% per decade. Here, the difference in trends between the two model simulations is also 0.5% per decade; however, we can easily infer that the reduction of halogens after 1997 explains about 55% of the upward trend in the upper stratospheric ozone (1–7 hPa) and about 24% of the trend in the lower stratospheric ozone (30–100 hPa).

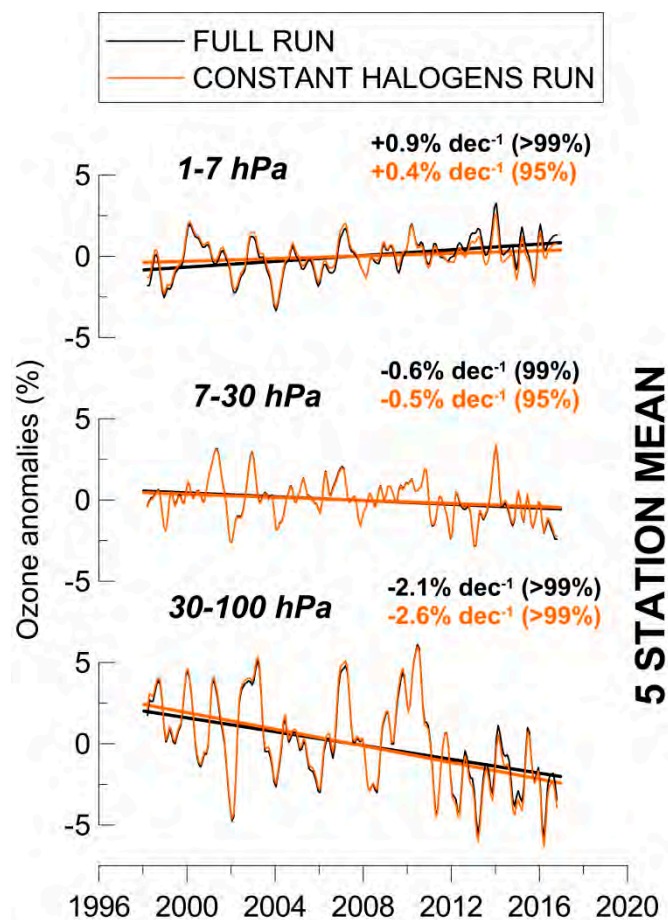


Figure 4. Oslo CTM3 simulations of stratospheric ozone. Black line shows trends derived from the main simulation (FULL); orange line shows trends derived from the simulation with constant halogens at 1998 levels. Values in parentheses refer to statistical significance of each trend. Five stations are HHP–OHP–TMO–MLO–LAU. Variability related to the seasonal cycle and dynamical proxies is removed from the data.

More analytically, in the case of upper stratospheric ozone, we estimate that the trend would have decreased from 0.9% to 0.4% per decade if halogens had remained constant at 1998 levels after 1998, and in the case of the lower stratospheric ozone, from -2.1% to -2.6% per decade, respectively. We applied a paired t-test to determine whether the differences between the paired observations (full versus fixed halogen simulations) are significant at the 0.05 level. In both layers, we found that the two means become significantly different after 2001 (upper stratosphere: $t = 2.47516$, $p = 0.01425$, $N = 180$; lower stratosphere: $t = 2.19451$, $p = 0.02949$, $N = 180$). We note that the difference in trends between the two model simulations is almost zero in the middle stratosphere.

3.3. Effect of GHGs on Ozone Trends

With the CCM simulations, we were able to look into the effect of GHGs increase on long-term ozone trends. Figure 5 compares two free-running simulations: a reference simulation with background GHGs mixing ratios (RC2-base-04) [21] and the same simulation with fixed GHGs at 1960 levels (SC2-fGHG-01) [22]. Blue dots show ozone observations from SBUV (v8.6) satellite data. The right panel shows the differences between the two model simulations (RC2-base-04 minus SC2-fGHG-01) as a measure of the effect of global warming on the vertical ozone profiles. The figure refers to the average of five lidar stations. The model reproduces very well the ozone turning point in the upper stratosphere during the 1990s, where the sign of the trends reversed to positive. Good agreement with the satellite observations exists in other layers as well.

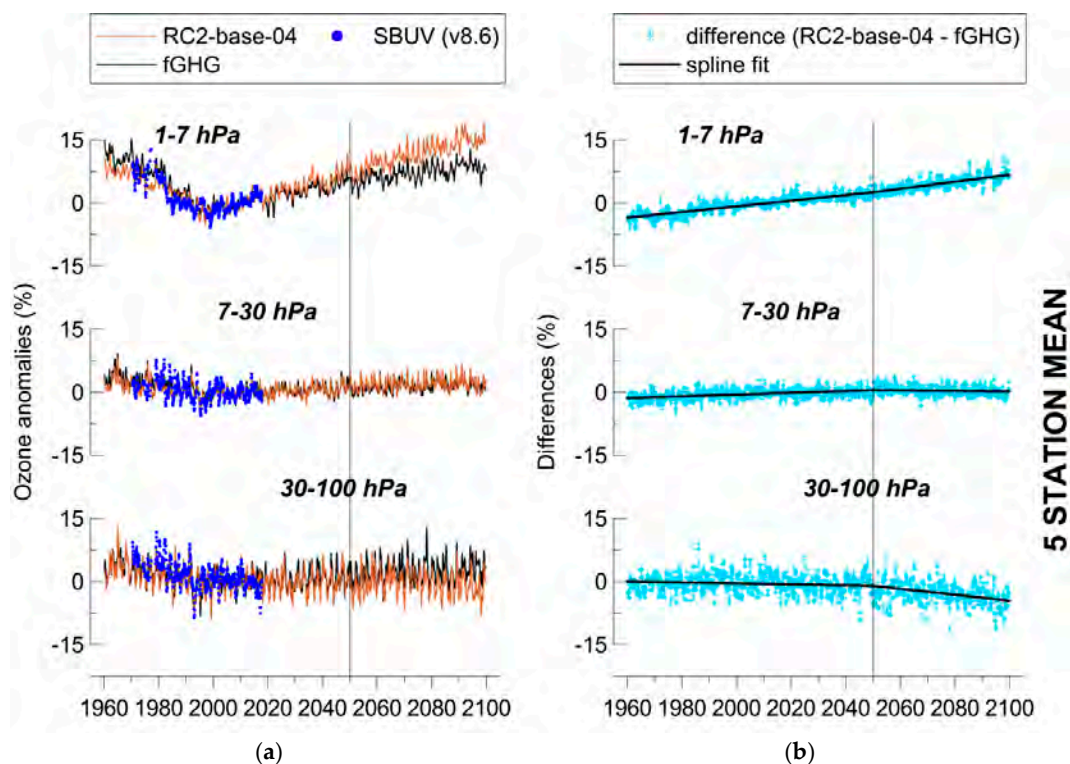


Figure 5. (a) Observed and simulated ozone changes. Model simulations refer to two free-running CCM simulations, a reference simulation with increasing GHGs emissions according to RCP-6.0 (RC2-base-04) and the same simulation with fixed GHGs emissions at 1960 levels (SC2-fGHG-01). (b) Differences (in %) between the two model simulations. The anomalies are deseasonalized data averaged at five stations: HHP–OHP–TMO–MLO–LAU.

In the long-term, the differences between the two model simulations show a positive trend in the upper stratosphere, no trend in the middle stratosphere and a negative trend in the lower stratosphere, which becomes evident after the 2040s. The upward trend in the upper stratosphere is explained by the fact that increases in GHGs lead to cooling of the upper stratosphere, which slows down temperature-dependent odd-oxygen loss processes and increases upper-stratospheric ozone [22]. On the contrary, lower-stratospheric ozone is decreasing due to the evolution of GHGs.

In the short-term, the isolation of the effect of GHGs cannot be identified in the short period from 1998 to 2016, because the signal is too noisy due to internal variability. We conclude that the differences between the two model simulations do not reveal any trend in the period of 1998–2016 due to GHGs. This is in line with the tropopause variability, which shows insignificant trends for the same period (Figure 3). The effect of GHGs on stratospheric ozone trends can be found after 2050, in the RC2-base-04 simulation. The mechanism for the change after 2050 is the strengthening in the meridional (Brewer–Dobson) circulation under enhanced GHGs concentrations. It is most obvious in the tropical region, where we identify stronger upwelling, which can be clearly identified in ozone signatures (i.e., lower ozone values in the tropical lower stratosphere and higher values in the tropical upper troposphere), but also in water vapor and methane, as well as in the temperature field. We note here that the dynamic change can be larger compared to the radiation of GHGs because of feedback mechanisms. Regarding the EMAC model, the complete dynamic feedback of EMAC is in line with other CCM studies. However, it is difficult (so far) to determine (quantitatively) the individual mechanisms regarding the complete dynamic signature, as there are also possible interactions with chemical changes (e.g., feedback with ozone).

3.4. Effect of GHGs on Surface DNA Active UV-B Irradiance

We further studied the impact of GHGs evolution on surface UV-B irradiance active for DNA damage at the five lidar stations, using CCM simulations (Figure 6). The model simulations are the same as above, i.e., the free-running simulation with increasing GHGs according to RCP-6.0 (RC2-based-04) and the sensitivity simulation with constant GHGs at 1960 levels (SC2-fGHG-01). The green dots show the deseasonalized DNA-weighted UV irradiance data from NDACC averaged at Haute Provence, Mauna Loa and Lauder, around local noon, indicating the agreement between the variances in the simulations and the ground-based measurements. The difference between the two simulations indicates the impact of increased GHGs on DNA active UV-B irradiance at ground level in the middle- and low-latitude lidar stations.

The differences show that DNA active UV-B irradiance tends to increase by +1.3% per decade after the year 2050, while the respective difference for total ozone does not show any trend after 2050. We find that the trend in UV-B irradiance is associated with cloud-cover decrease. The bottom panel shows cloud-cover variations from the two model simulations for total clouds (1000–200 hPa). The differences between the two simulations (shown on the right) reveal a decreasing trend in total cloud cover of −1.4% per decade after 2050, which is in accordance with the estimated increase in DNA active UV-B irradiance at ground level. Increased UV-B irradiance active for DNA damage in the future will have adverse effects on humans and the environment [26].

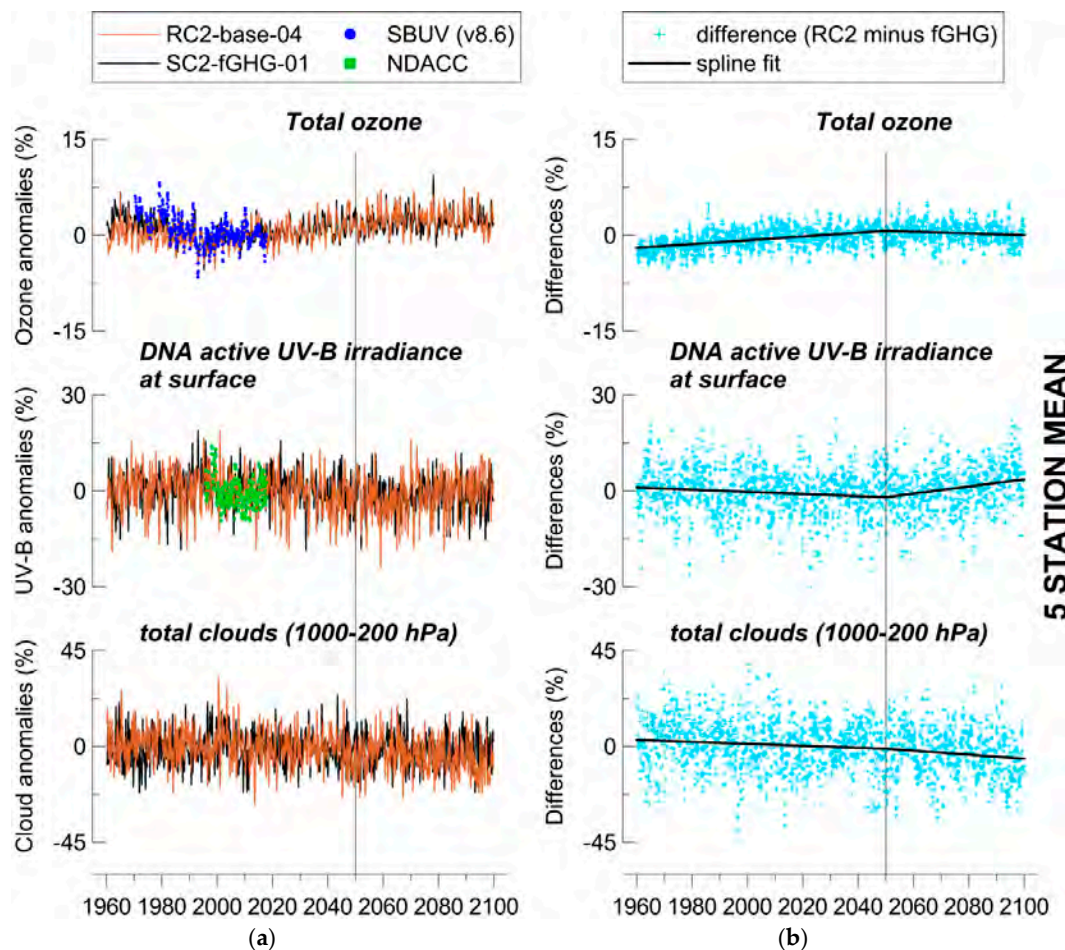


Figure 6. (a) Impact of GHGs on total ozone, UV-B irradiance and clouds based on simulations with increasing and fixed GHGs mixing ratios. RC2-base-04 is the simulation with increasing GHGs according to RCP-6.0; SC2-fGHG-01 is the simulation with fixed GHGs emissions at 1960 levels. The anomalies are deseasonalized data averaged at five lidar stations (HHP–OHP–TMO–MLO–LAU). Green dots show deseasonalized DNA-weighted UV data averaged at OHP, MLO and LAU from the Network for the Detection of Atmospheric Composition Change (NDACC). (b) Difference between the two model simulations.

4. Conclusions

We have analyzed the impact of stratospheric halogen reduction and increase in greenhouse gases on stratospheric ozone changes with the Oslo chemistry transport model and the EMAC chemistry climate model. In addition, we also looked at the effect of increase in greenhouse gases on DNA active UV-B radiation at ground level. The main results can be summarized as follows:

- Measurements and CTM simulations with the Oslo model after 1997 for the selected five lidar stations' locations show a statistically significant increasing trend in ozone in the upper stratosphere, above 7 hPa, an insignificant decreasing trend in the middle stratosphere, between 7 and 30 hPa, and a significant decreasing trend in the lower stratosphere, between 30 and 100 hPa.
- This interchange of positive and negative trends in the vertical ozone profile has resulted in insignificant trends, both in the total ozone column and the tropopause pressure, during the period of study (1998–2016).
- As expected from the Oslo CTM3 simulations, the effect of halogen reduction on ozone is maximized at 1–7 hPa at all locations. Comparison between CTM simulations, with fixed and without fixed halogens at 1998 levels, showed that the reduction of halogen-mixing ratios after

1997 explains about 55% of the observed upward trend in the upper stratospheric ozone (1–7 hPa) (i.e., trend from main simulation: +0.9% per decade, trend from simulation with fixed halogens: +0.4% per decade) and about 24% of the trend in the lower stratospheric ozone (30–100 hPa) (i.e., trend from main simulation: –2.1% per decade, trend from simulation with fixed halogens: –2.6% per decade).

- The effect of GHGs increase on stratospheric profile ozone trends cannot be identified in the short period 1998–2016. As expected from the EMAC CCM calculations, the effect of GHGs becomes evident after the middle of this century.
- The EMAC CCM projections indicate significant positive trends in the upper stratosphere after the year 2050, insignificant trends in the middle stratosphere and significant negative trends in the lower stratosphere (e.g., [27,28]). Total ozone does not show significant trends after the year 2050 (–0.1% per decade).
- Solar UV-B irradiance active for DNA damage at the five lidar stations is estimated to increase on average by +1.3% per decade after the year 2050, associated with a significant decrease in cloud cover of –1.4% per decade due to the evolution of GHGs. In that case, the adverse effects of excessive UV-B irradiation at these locations are expected to increase due to future global warming.
- Our estimates regarding the long-term changes of modeled UV are strongly determined by the cloud behavior in the specific model simulation, and as such, our conclusions about the future behavior of UV are subjected to uncertainties induced by the uncertainties in modeling future clouds. It is beyond the scope of this paper to resolve the issues with clouds in the model.

Supplementary Materials: The following are available online at <http://www.mdpi.com/2073-4433/11/3/228/s1>. Table S1: Statistics of correlations between ozone from Oslo CTM3, EMAC CCM (SC1SD-base-02), SBUV (v8.6) and Lidar data anomalies in **Hohenpeissenberg**, in the: (a) upper stratosphere (1-7 hPa), (b) middle stratosphere (7-30 hPa) and (c) lower stratosphere (30-100 hPa). Seasonal and other known natural variability has been removed from the data. For lidars the upper stratospheric layers are confined between 3 and 7 hPa, Table S2: Statistics of correlations between ozone from Oslo CTM3, EMAC CCM (SC1SD-base-02), SBUV (v8.6) and Lidar data anomalies in **Haute Provence**, in the: (a) upper stratosphere (1-7 hPa), (b) middle stratosphere (7-30 hPa) and (c) lower stratosphere (30-100 hPa). Seasonal and other known natural variability has been removed from the data. For lidars the upper stratospheric layers are confined between 3 and 7 hPa, Table S3: Statistics of correlations between ozone from Oslo CTM3, EMAC CCM (SC1SD-base-02), SBUV (v8.6) and Lidar data anomalies in **Table Mountain**, in the: (a) upper stratosphere (1-7 hPa), (b) middle stratosphere (7-30 hPa) and (c) lower stratosphere (30-100 hPa). Seasonal and other known natural variability has been removed from the data. For lidars the upper stratospheric layers are confined between 3 and 7 hPa, Table S4: Statistics of correlations between ozone from Oslo CTM3, EMAC CCM (SC1SD-base-02), SBUV (v8.6) and Lidar data anomalies in **Mauna Loa**, in the: (a) upper stratosphere (1-7 hPa), (b) middle stratosphere (7-30 hPa) and (c) lower stratosphere (30-100 hPa). Seasonal and other known natural variability has been removed from the data. For lidars the upper stratospheric layers are confined between 3 and 7 hPa, Table S5: Statistics of correlations between ozone from Oslo CTM3, EMAC CCM (SC1SD-base-02), SBUV (v8.6) and Lidar data anomalies in **Lauder**, in the: (a) upper stratosphere (1-7 hPa), (b) middle stratosphere (7-30 hPa) and (c) lower stratosphere (30-100 hPa). Seasonal and other known natural variability has been removed from the data. For lidars the upper stratospheric layers are confined between 3 and 7 hPa.

Author Contributions: Conceptualization, K.E., J.K. and C.S.Z.; data curation, S.G.-B., W.S., C.B., T.L., J.B.L., R.Q. and D.P.J.S.; formal analysis, K.E. and J.K.; methodology, K.E. and C.S.Z.; resources, M.D., P.J. and A.S.H.; software, J.K. and I.F.; writing—original draft preparation, K.E.; writing—review and editing, C.S.Z., A.F.B., I.P., S.G.-B., P.J., M.D., A.S.H., I.F., T.L. and J.B.L. All authors have read and agreed to the published version of the manuscript.

Funding: We acknowledge support of this work by the project “PANhellenic infrastructure for Atmospheric Composition and climatE change” (MIS 5021516), which is implemented under the action “Reinforcement of the Research and Innovation Infrastructure”, funded by the Operational Programme “Competitiveness, Entrepreneurship and Innovation” (NSRF 2014-2020) and co-financed by Greece and the European Union (European Regional Development Fund).

Acknowledgments: We acknowledge the Long-term Ozone Trends and Uncertainties in the Stratosphere (LOTUS) activity, supported by SPARC (Stratosphere-Troposphere Processes And their Role in Climate), WMO and the International Ozone Commission. Also, the Mariolopoulos-Kanaginis Foundation for the Environmental Sciences. Lidar measurements are performed in the frame of the Network for the Detection of Atmospheric Composition Change (NDACC). Lidar measurements at OHP are funded by the French Centre National de la Recherche Scientifique (CNRS). We acknowledge the work of personnel at the lidar stations. The EMAC simulations have

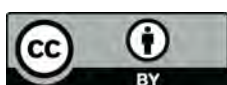
been performed at the German Climate Computing Centre (DKRZ) through support from the Bundesministerium für Bildung und Forschung (BMBF). DKRZ and its scientific steering committee are gratefully acknowledged for providing the HPC and data archiving resources for this consortial project ESCiMo (Earth System Chemistry Integrated Modelling). We acknowledge the SBUV science team for providing the satellite ozone profiles. NIWA UV spectrometer systems, serial numbers UV3 (Mauna Loa, HI) and UV5 (Boulder, CO) in the USA are owned and operated by NOAA/ESRL/Global Monitoring Division, Boulder, CO. They are maintained, calibrated and operated by NOAA. The final data from both of these instruments are quality controlled and produced by NIWA-Lauder, New Zealand. The data are archived at the NDACC data repository, <ftp://ftp.cpc.ncep.noaa.gov/ndacc/station/>. We thank NIWA and NOAA for the use of their data in this publication. The study is dedicated to the memory of Ivar Isaksen.

Conflicts of Interest: The authors declare no conflict of interest.

References

1. Bais, A.F.; McKenzie, R.L.; Bernhard, G.; Aucamp, P.J.; Ilyas, M.; Madronich, S.; Tourpali, K. Ozone depletion and climate change: Impacts on UV radiation. *Photochem. Photobiol. Sci.* **2015**, *14*, 19–52. [[CrossRef](#)] [[PubMed](#)]
2. Molina, M.J.; Rowland, F.S. Stratospheric sink for chlorofluoromethanes: Chlorine atom catalysed destruction of ozone. *Nature* **1974**, *249*, 810–812. [[CrossRef](#)]
3. WMO. *Executive Summary: Scientific Assessment of Ozone Depletion: 2018*; Global Ozone Research and Monitoring Project—Report No. 58; World Meteorological Organization: Geneva, Switzerland, 2018; p. 67.
4. den Outer, P.N.; Slaper, H.; Kaurola, J.; Lindfors, A.; Kazantzidis, A.; Bais, A.F.; Feister, U.; Junk, J.; Janouch, M.; Josefsson, W. Reconstructing of erythemal ultraviolet radiation levels in Europe for the past 4 decades. *J. Geophys. Res.* **2010**, *115*, D10102. [[CrossRef](#)]
5. WMO. *Scientific Assessment of Ozone Depletion: 2010*; Global Ozone Research and Monitoring Project—Report No. 52; World Meteorological Organization: Geneva, Switzerland, 2011; p. 516.
6. Bais, A.F.; Bernhard, G.; McKenzie, R.L.; Aucamp, P.J.; Young, P.J.; Ilyas, M.; Jöckel, P.; Deushi, M. Ozone-climate interactions and effects on solar ultraviolet radiation. *Photochem. Photobiol. Sci.* **2019**, *18*, 602–640. [[CrossRef](#)] [[PubMed](#)]
7. Zerefos, C.; Kapsomenakis, J.; Eleftheratos, K.; Tourpali, K.; Petropavlovskikh, I.; Hubert, D.; Godin-Beekmann, S.; Steinbrecht, W.; Frith, S.; Sofieva, V.; et al. Representativeness of single lidar stations for zonally averaged ozone profiles, their trends and attribution to proxies. *Atmos. Chem. Phys.* **2018**, *18*, 6427–6440. [[CrossRef](#)]
8. Petropavlovskikh, I.; Godin-Beekmann, S.; Hubert, D.; Damadeo, R.; Hassler, B.; Sofieva, V. (Eds.) *SPARC/IO3C/GAW Report on Long-Term Ozone Trends and Uncertainties in the Stratosphere*; SPARC Report No. 9, GAW Report No. 241, WCRP-17/2018. Available online: www.sparc-climate.org/publications/sparc-reports (accessed on 24 February 2020). [[CrossRef](#)]
9. Harris, N.R.P.; Hassler, B.; Tummon, F.; Bodeker, G.E.; Hubert, D.; Petropavlovskikh, I.; Steinbrecht, W.; Anderson, J.; Bhartia, P.K.; Boone, C.D.; et al. Past changes in the vertical distribution of ozone—Part 3: Analysis and interpretation of trends. *Atmos. Chem. Phys.* **2015**, *15*, 9965–9982. [[CrossRef](#)]
10. Ball, W.T.; Alsing, J.; Mortlock, D.J.; Staehelin, J.; Haigh, J.D.; Peter, T.; Tummon, F.; Stübi, R.; Stenke, A.; Anderson, J.; et al. Evidence for a continuous decline in lower stratospheric ozone offsetting ozone layer recovery. *Atmos. Chem. Phys.* **2018**, *18*, 1379–1394. [[CrossRef](#)]
11. Wargan, K.; Orbe, C.; Pawson, S.; Ziemke, J.R.; Oman, L.D.; Olsen, M.A.; Coy, L.; Knowland, K.E. Recent decline in extratropical lower stratospheric ozone attributed to circulation changes. *Geophys. Res. Lett.* **2018**, *45*, 5166–5176. [[CrossRef](#)]
12. Bais, A.F.; Tourpali, K.; Kazantzidis, A.; Akiyoshi, H.; Bekki, S.; Braesicke, P.; Chipperfield, M.P.; Dameris, M.; Eyring, V.; Garny, H.; et al. Projections of UV radiation changes in the 21st century: Impact of ozone recovery and cloud effects. *Atmos. Chem. Phys.* **2011**, *11*, 7533–7545. [[CrossRef](#)]
13. Leblanc, T.; Sica, R.J.; van Gijsel, J.A.E.; Godin-Beekmann, S.; Haeefele, A.; Trickl, T.; Payen, G.; Liberti, G. Proposed standardized definitions for vertical resolution and uncertainty in the NDACC lidar ozone and temperature algorithms—Part 2: Ozone DIAL uncertainty budget. *Atmos. Meas. Tech.* **2016**, *9*, 4051–4078. [[CrossRef](#)]

14. Steinbrecht, W.; Froidevaux, L.; Fuller, R.; Wang, R.; Anderson, J.; Roth, C.; Bourassa, A.; Degenstein, D.; Damadeo, R.; Zawodny, J.; et al. An update on ozone profile trends for the period 2000 to 2016. *Atmos. Chem. Phys.* **2017**, *17*, 10675–10690. [[CrossRef](#)]
15. De Mazière, M.; Thompson, A.M.; Kurylo, M.J.; Wild, J.D.; Bernhard, G.; Blumenstock, T.; Braathen, G.O.; Hannigan, J.W.; Lambert, J.-C.; Leblanc, T.; et al. The Network for the Detection of Atmospheric Composition Change (NDACC): History, status and perspectives. *Atmos. Chem. Phys.* **2018**, *18*, 4935–4964. [[CrossRef](#)]
16. Godin-Beekmann, S.; Porteneuve, J.; Garnier, A. Systematic DIAL lidar monitoring of the stratospheric ozone vertical distribution at Observatoire de Haute-Provence (43.92° N, 5.71° E). *J. Environ. Monit.* **2003**, *5*, 57–67. [[CrossRef](#)] [[PubMed](#)]
17. Kalnay, E.; Kanamitsu, M.; Kistler, R.; Collins, W.; Deaven, D.; Gandin, L.; Iredell, M.; Saha, S.; White, G.; Woollen, J.; et al. The NCEP/NCAR 40-Year Reanalysis Project. *B. Am. Meteor. Soc.* **1996**, *77*, 437–471. [[CrossRef](#)]
18. Søvde, O.A.; Prather, M.J.; Isaksen, I.S.A.; Berntsen, T.K.; Stordal, F.; Zhu, X.; Holmes, C.D.; Hsu, J. The chemical transport model Oslo CTM3. *Geosci. Model Dev.* **2012**, *5*, 1441–1469. [[CrossRef](#)]
19. Prather, M.J. Photolysis rates in correlated overlapping cloud fields: Cloud-J 7.3c. *Geosci. Model Dev.* **2015**, *8*, 2587–2595. [[CrossRef](#)]
20. Sander, S.P.; Abbatt, J.; Barker, J.R.; Burkholder, J.B.; Friedl, R.R.; Golden, D.M.; Huie, R.E.; Kolb, C.E.; Kurylo, M.J.; Moortgat, G.K.; et al. *Chemical Kinetics and Photochemical Data for Use in Atmospheric Studies*; Evaluation No. 17; JPL Publication: Jet Propulsion Laboratory, Pasadena, CA, USA, 2011. Available online: <http://jpldataeval.jpl.nasa.gov> (accessed on 12 September 2018).
21. Jöckel, P.; Tost, H.; Pozzer, A.; Kunze, M.; Kirner, O.; Brenninkmeijer, C.A.M.; Brinkop, S.; Cai, D.S.; Dyroff, C.; Eckstein, J.; et al. Earth System Chemistry integrated Modelling (ESCiMo) with the Modular Earth Submodel System (MESSy) version 2.51. *Geosci. Model Dev.* **2016**, *9*, 1153–1200. [[CrossRef](#)]
22. Dhomse, S.S.; Kinnison, D.; Chipperfield, M.P.; Salawitch, R.J.; Cionni, I.; Hegglin, M.I.; Abraham, N.L.; Akiyoshi, H.; Archibald, A.T.; Bednarz, E.M.; et al. Estimates of ozone return dates from Chemistry-Climate Model Initiative simulations. *Atmos. Chem. Phys.* **2018**, *18*, 8409–8438. [[CrossRef](#)]
23. Sander, R.; Jöckel, P.; Kirner, O.; Kunert, A.T.; Landgraf, J.; Pozzer, A. The photolysis module JVAL-14, compatible with the MESSy standard, and the JVal PreProcessor (JVPP). *Geosci. Model Dev.* **2014**, *7*, 2653–2662. [[CrossRef](#)]
24. Brühl, C.; Crutzen, P.J. On the disproportionate role of tropospheric ozone as a filter against solar UV-B radiation. *Geophys. Res. Lett.* **1989**, *16*, 703–706. [[CrossRef](#)]
25. McKenzie, R.; Bernhard, G.; Liley, B.; Disterhoft, P.; Rhodes, S.; Bais, A.; Morgenstern, O.; Newman, P.; Oman, L.; Brogniez, C.; et al. Success of Montreal Protocol Demonstrated by Comparing HighQuality UV Measurements with “World Avoided” Calculations from Two Chemistry-Climate Models. *Sci. Rep.* **2019**, *9*, 12332. [[CrossRef](#)] [[PubMed](#)]
26. Lucas, R.M.; Yazar, S.; Young, A.R.; Norval, M.; de Gruijl, F.R.; Takizawa, Y.; Rhodes, L.E.; Sinclair, C.A.; Neale, R.E. Human health in relation to exposure to solar ultraviolet radiation under changing stratospheric ozone and climate. *Photochem. Photobiol. Sci.* **2019**, *18*, 641–680. [[CrossRef](#)] [[PubMed](#)]
27. Braesicke, P.; Neu, J.; Fioletov, V.; Godin-Beekmann, S.; Hubert, D.; Petropavlovskikh, I.; Shiotani, M.; Sinnhuber, B.-M. Update on Global Ozone: Past, Present, and Future. In *Scientific Assessment of Ozone Depletion: 2018*; Global Ozone Research and Monitoring Project–Report No. 58; World Meteorological Organization: Geneva, Switzerland, 2018; Chapter 3.
28. Langematz, U.; Tully, M.; Calvo, N.; Dameris, M.; de Laat, A.T.J.; Klekociuk, A.; Müller, R.; Young, P. Polar Stratospheric Ozone: Past, Present, and Future. In *Scientific Assessment of Ozone Depletion: 2018*; Global Ozone Research and Monitoring Project–Report No. 58; World Meteorological Organization: Geneva, Switzerland, 2018; Chapter 4.



Article

The Combined Effect of Ozone and Aerosols on Erythemal Irradiance in an Extremely Low Ozone Event during May 2020

Ioannis-Panagiotis Raptis ^{1,*}, Kostas Eleftheratos ^{2,3}, Stelios Kazadzis ⁴, Panagiotis Kosmopoulos ¹, Kyriakoula Papachristopoulou ^{2,5} and Stavros Solomos ⁶

- ¹ Institute for Environmental Research and Sustainable Development, National Observatory of Athens, GR15236 Athens, Greece; pkosmo@noa.gr
- ² Faculty of Geology and Geoenvironment, National and Kapodistrian University of Athens, GR15236 Athens, Greece; kelef@geol.uoa.gr
- ³ Biomedical Research Foundation, Academy of Athens, GR11527 Athens, Greece
- ⁴ Physicalisch-Meteorologisches Observatorium Davos, World Radiation Center, CH-7260 Davos, Switzerland; Stelios.Kazadzis@pmodwrc.ch
- ⁵ Institute for Astronomy, Astrophysics, Space Applications and Remote Sensing (IAASARS), National Observatory of Athens, GR15236 Athens, Greece; kpapachr@noa.gr
- ⁶ Research Centre for Atmospheric Physics and Climatology, Academy of Athens, GR15236 Athens, Greece; ssolomos@academyofathens.gr
- * Correspondence: piraptis@noa.gr

Abstract: In this study we focus on measurements and modeled UV index in the region of Athens, Greece, during a low ozone event. During the period of 12–19 May 2020, total ozone column (TOC) showed extremely low values, 35–55 Dobson Units (up to 15%) decrease from the climatic mean (being lower than the -2σ). This condition favors the increase of UV erythemal irradiance, since stratospheric ozone is the most important attenuator at the UVB spectral region. Simultaneously, an intrusion of Saharan dust aerosols in the region has masked a large part of the low ozone effect on UV irradiance. In order to investigate the event, we have used spectral solar irradiance measurements from the Precision Solar Radiometer (PSR), TOC from the Brewer spectrophotometer, and Radiative Transfer Model (RTM) calculations. Model calculations of the UV Index (UVI) showed an increase of ~30% compared to the long-term normal UVI due to the low TOC while at the same time and for particular days, aerosols masked this effect by ~20%. The RTM has been used to investigate the response in the UV spectral region of these variations at different solar zenith angles (SZAs). Spectra simulated with the RTM have been compared to measured ones and an average difference of ~2% was found. The study points out the importance of accurate measurements or forecasts of both ozone and aerosols when deriving UVI under unusual low ozone–high aerosol conditions.

Keywords: ultraviolet; ozone; aerosol; UV Index; erythemal; PSR



Citation: Raptis, I.-P.; Eleftheratos, K.; Kazadzis, S.; Kosmopoulos, P.; Papachristopoulou, K.; Solomos, S. The Combined Effect of Ozone and Aerosols on Erythemal Irradiance in an Extremely Low Ozone Event during May 2020. *Atmosphere* **2021**, *12*, 145. <https://doi.org/10.3390/atmos12020145>

Received: 20 October 2020

Accepted: 19 January 2021

Published: 24 January 2021

Publisher's Note: MDPI stays neutral with regard to jurisdictional claims in published maps and institutional affiliations.



Copyright: © 2021 by the authors. Licensee MDPI, Basel, Switzerland. This article is an open access article distributed under the terms and conditions of the Creative Commons Attribution (CC BY) license (<https://creativecommons.org/licenses/by/4.0/>).

1. Introduction

Ultraviolet (UV) radiation is a small part (~3% [1]) of the incoming solar radiation at Earth's surface but has a number of biological effects when absorbed by human skin, which can be either harmful or beneficial [2,3]. Harmful effects, linked to UV overexposure, include skin erythema, the increased risk of skin cancer, and multiple eye diseases (snow blindness, cataract). On the other hand, UVB radiation is extremely important for the human body, as it is crucial for synthesizing Vitamin D [4,5]. The effect of UV radiation on living cells is estimated by biological effective irradiances and doses [6]. Effective irradiances are retrieved by weighting actual spectral irradiances using the relative action spectrum. Doses are derived afterwards, when weight functions are integrated by time. UV Index (UVI) is a unitless variable that was introduced by the World Meteorological Organization (WMO) in 1994, aiming to better inform the general public about the dangers of UV radiation [7]. UVI is a scaled version of erythemally weighted UV, which is interpreted

in an easily understandable scale of 0–20 and characterizes the safe exposure according to skin type [8,9]. There is a growing concern in the scientific community on the variation of UV radiation in response to climate change [10–12]. Bais et al. [11] showed that higher values of UV are expected by the end of the 21st century in tropical areas and a decrease in mid-latitudes, but these estimations still hold high uncertainties. Eleftheratos et al. [13] showed that solar UVB irradiance that produces deoxyribonucleic acid (DNA) damage would increase after the year 2050. Such change is driven by a significant decrease in cloud cover due to the evolution of greenhouse gases in the future, suggesting that the process of climate change will overwhelm the effect of ozone recovery on UVB irradiance in the mid-latitudes.

UV irradiance reaching Earth's ground level is related to a number of factors and it is crucial to investigate them in order to monitor and predict it. In the UVB region, O₃ and SO₂[−] are the main absorbers, while NO₂[−] is the dominant absorber in the UVA [14]. Significant UV increase had been reported in the past decades due to ozone depletion [15]. Signs of recovering ozone, since the Montreal Protocol was applied, has been recorded [16,17]. Nevertheless, extremely low values, which result in high UV, are measured occasionally.

Aerosols in the atmosphere also play a crucial role in UV irradiance reaching Earth's surface. Aerosol optical depth (AOD) is a parameter that quantifies the attenuation of irradiance when passing from an aerosol layer and is wavelength dependent [18]. Different aerosol types have various effects in the UV, causing a spectral dependence of the extinction. Dust of desert origin has been reported as having the most significant extinction in the UV spectral region, which could have a major influence on the received UV irradiance, even eliminating the influence of low ozone, during severe events [19]. Additionally, Roman [20] has reported that desert dust could add an attenuation of up to 50% in direct UV irradiance, while diffuse irradiance could increase up to 40%. Other aerosol types that have a significant role in the UV spectral region are black [21] and brown carbon [22]. Dust intrusions in the Eastern Mediterranean, including the Athens area, have been presented in several studies [23–25].

The attenuators described above are less important when clouds are present, since clouds strongly attenuate all radiation, including UV. The increase of sun elevation proportionally increases the UV intensity. Two other factors that influence the UVI are the solar zenith angle (SZA) [26] and the altitude [27]. SZA is the most common parametrization of the sun elevation, which is defined by astronomical calculations, indicating the air mass the light passes through [26].

A number of studies have focused on the UV trends over the last decades which are affected by trends in gases (O₃, NO₂), aerosols, and cloud coverage. Increase of UV has been reported in south and central Europe and decrease at higher latitudes [28]. Zerefos et al. [17] showed that the increase of total O₃ over the 1995–2006 period at mid-latitudes was not sufficient to reverse UVB increase, which was masked by decreasing aerosols, while Eleftheratos et al. [29] showed that at high latitudes, stratospheric ozone increase and UVB decrease were in agreement in the absence of large aerosol variations.

UVI is also routinely forecasted by a number of services and the output is provided to the general public for protection from harmful UV doses. For example, the Tropospheric Emission Monitoring Internet Service (TEMIS), by the Royal Netherlands Meteorological Institute, provides a daily clear sky UVI forecast for Europe, for eight days ahead, using the algorithm of Allart et al. [30], which takes into account total ozone column (TOC) and SZA and uses an empirical aerosol correction, which leads to overestimations when high aerosol loads are present [31].

In this study, we focus on measurements and modeled UV index in the region of Athens, Greece, during a period of an extremely low ozone event. During this period, TOC was much lower than the long-term mean (in the range of 35–55 Dobson Units, DU), reaching values as low as the -2σ values of the climatological average. A co-occurring invasion of Saharan dust in the region counteracted a large part of the low ozone effect on the UV irradiance. In order to investigate the event, we have used the measurements

from the Precision Solar Radiometer (PSR) and Brewer spectrophotometer (BRS) along with the Radiative Transfer Model (RTM) simulations of the atmospheric conditions. The coincidence of increased aerosols and extremely low ozone during the week of 12–19 May 2020 motivated us to study this peculiar event and to better quantify the roles of dust aerosols and ozone in UVB irradiance.

Besides the description of the observed extremely low ozone–high UVI–high aerosol Saharan dust event which we target in this study, it is important to highlight the motivation of this study and its difference from other works. The observed low ozone concentrations that occurred during May 2020 in Athens is a rare phenomenon, as May is largely characterized by high amounts of ozone transported from the tropics to higher latitudes by the Brewer–Dobson circulation. These low ozone amounts contributed to high amounts of UVB irradiance in May, the magnitude of which is typically measured during July under cloudless conditions [32]. It might be that such low ozone events become more frequent in the future during spring [10,11]. In this respect it is important to know how much change in UVB radiation can be caused so that we can use this information to evaluate future calculations of UVB variability. While UVB models predicted high levels of ultraviolet radiation in Athens during the low ozone week, the measured UVI levels were lower than expected. The reason for this was the increased dust aerosols that attenuated the incoming solar radiation reaching the ground. Model calculations for forecasting UVI currently used to inform the authorities and the general public do not take into account the nature of aerosols and the expected loads (e.g., TEMIS). It is shown that the occurrence of increased aerosols during the study period balanced the effect of low ozone amounts on UVB irradiance, thus mitigating the enhanced UVB levels.

The paper is organized as follows. The data sources (ground-based instruments, satellite data, modeling) and methodology are described in Section 2. The abnormal ozone, UVI, and AOD measurements during the exceptional week of May 2020 in Athens and the respective climatological values are presented in Section 3, alongside some modeled examples for spectral sensitivity in the UV region. Finally, Section 4 summarizes the main results.

2. Instruments and Methods

Data used in this study were recorded at two different locations in Athens, Greece, by PSR and BRS instruments. The two locations are 5 km apart. The BRS is installed at the roof of Biomedical Research Foundation of the Academy of Athens, which is located in a green area at a distance of about 4 km from the city center and is partly influenced by urban emissions. The PSR is installed at the Actinometric Station of National Observatory of Athens, in a green area in the city center. Aerosols in Athens can consist of sea-salt aerosols, dust from the Sahara Desert, smoke particles from forest fires, and small particles typical of urban and industrialized environments [33,34].

UVI is currently monitored by about 160 stations from 25 countries around Europe [35]. Instruments operating at these stations are separated into three types, according to the technique of measurement, as broadband, narrow-band filter, and narrow-band spectral radiometers. The estimated relative uncertainty for these UV irradiance radiometric measurements is 4.6% [36], which propagates an uncertainty of 0.61 (at 1σ) for retrieved UVI [37]. Additionally, UV is monitored through satellite retrievals, which are covering the whole globe [38]. Satellite measurements are usually used for climatological studies [39] and for monitoring UV irradiance in areas with no ground-based measurements. For this study we use spectral measurements of irradiance in the UV spectrum to retrieve UVI.

2.1. PSR

The Precision Solar Spectroradiometer has been designed and manufactured by Physicalisch-Meteorologisches Observatorium Davos, World Radiation Center (PMOD/WRC), Davos, Switzerland, for high precision and accuracy of solar spectral measurements. It measures irradiance at 1024 channels in the spectral range of 300–1020 nm with an average

step of ~0.7 nm, spectral resolution in the range of 1.5–6 nm (depending on the measured wavelength) [40,41]. PSR 007 is installed in Athens (37.9 N, 23.7 E, 130 m above sea level) and it was last calibrated on June 2019 at the World Radiation Center using a calibrated standard 1000 W tungsten–halogen FEL lamp. Uncertainty of the measurements has been estimated in the range of 1.7–2.0% in the UVA with higher uncertainties recorded at the UVB spectral region, due to lower signal and stray light [42]. PSR 007 has a global sensor mounted on the auxiliary port and by using the built-in shutter of the instrument, global horizontal irradiance (GHI) and direct irradiance can be measured by the same spectrometer. Thus, the same calibration and uncertainty budget is applied. The spectral measurement frequency is 1 min, when five spectral measurements are averaged and saved.

UVI is the parameter retrieved from the PSR measurements, used in this study. The formula for the calculation is:

$$\text{UVI} = k_{\text{er}} \int_{\lambda_1}^{\lambda_2} E(\lambda) S_{\text{er}}(\lambda) d\lambda \quad (1)$$

where k_{er} is a constant equal to 40 W/m², $E(\lambda)$ is the recorded solar spectral irradiance at wavelength λ in W/m²/nm, $S_{\text{er}}(\lambda)$ is the erythema action spectrum [43], and λ_1 and λ_2 are the limits of the UV spectral region. For our case, the integrated spectral region is 300 to 400 nm. This approach has an advantage, compared to broadband-based measured UVIs, since the whole spectrum of the region 300–400 nm is recorded, and no additional corrections are needed [32].

2.2. The Brewer Spectrophotometer

In this study we analyze TOC and AOD retrievals from a BRD MkIV spectrophotometer (number #001) operating at the roof of the Biomedical Research Foundation of the Academy of Athens in Greece (38.0 N, 23.8 E, 180 m a.s.l) since 2004. The BRS is an automated, diffraction-grating spectrometer that provides observations of the sun's intensity in the near UV range. The instrument measures the intensity of radiation in the UV absorption spectrum of ozone at five wavelengths (306.3, 310.1, 313.5, 316.8, and 320.1 nm) with a resolution of 0.5 nm. These data are used to derive columnar ozone and sulfur dioxide amounts and the aerosol optical depth [44].

Measurements with the BRS #001 have been exploited in several studies analyzing columnar ozone, sulfur dioxide, and aerosol optical depth [45–48]. TOC analyzed in this study is calculated from a combination of the direct sun (DS) measurements at UV wavelengths that experience different absorption by ozone passing through the atmosphere (310.1, 313.5, 316.8, and 320.1 nm), weighted with a predefined set of constants chosen to minimize the influence of SO₂ and linearly varying absorption features from, for example, clouds or aerosols [49]. TOC was retrieved using the differential absorption method [50].

The BRS #001 was regularly recalibrated against the traveling standard BRS instrument #017 in 2002 in Thessaloniki and in 2004, 2007, 2010, 2013, and 2019 on site in Athens. Internal standard lamp tests are performed on a daily basis to detect possible instrumental drifts. Ozone data were recalculated after standard lamp test corrections and were analyzed using the O3BREWERS data management software [51].

Finally, the AOD analyzed in this study was retrieved from the direct sun (DS) measurements at five standard wavelengths (306.3, 310.1, 313.5, 316.8, 320.1 nm) using the O3baod software package developed by Martin Stanek (<http://www.o3soft.eu/o3baod.html>). The setup of the software for the Athens BRS was done with the assistance of M. Stanek (private communication). AOD at 320.1 nm is reported here.

2.3. Satellite Data

Satellite data have been used in order to provide further evidence on the range of TOC. The Ozone Monitoring Instrument (OMI), which is a nadir-viewing UV/visible backscatter spectrometer on board NASA's satellite Aura, the ozone product algorithm, and the TOC retrieving process are described in Bhartia and Wellemeyer [52]. The main

procedures include a fitting of ozone absorption cross-section to the measured spectrum, an estimation of air mass factor, and corrections for cloud effects. Data processing and quality assurance of the TOC product were analytically outlined by Veefkind et al. [53]. Different studies [54,55] had found average biases less than 3% when comparing TOC retrievals from BRS and OMI, while McPeters et al. [56] showed that in mid-latitudes, the biases are SZA dependent. Satellite-retrieved UVI has large uncertainties, while aerosol loads have been recognized as a major source of errors, causing differences of up to 25% [57]. Comparison of OMI surface UV irradiance estimates with ground-based measurements [31] showed that OMI irradiances overestimate surface observations for UVB wavelengths from ~1.5% to 13.5% in contrast to underestimated satellite values for UVA wavelengths.

OMI TOC retrieval has one overpass above Athens per day in a distance of less than 50 km since 2002, which could be used to create an almost two-decade-long timeseries. Copernicus Atmospheric Service (CAM5) provides a reanalysis database of TOC, which we also used to detect the general ozone circulation at the area at the time of the event. This database is assimilating data from different satellites (Solar Backscatter Ultraviolet Radiometer—SBUV/2, OMI, Scanning Imaging Absorption Spectrometer for Atmospheric Chartography—SCIAMACHY, Global Ozone Monitoring Experiment—GOME and GOME2) alongside chemical transport modeling to provide TOC at $0.4^\circ \times 0.4^\circ$ spatial grid [53]. In [45] authors have compared the Athens BRS and OMI satellite TOC and reported a good agreement between the BRS and the satellite total ozone, which is of the order of 2.7% with a standard deviation of 4%. Analyzing OMI and BRS data for 2017–2020, we found a difference of 4.6% with a standard deviation of 5%.

2.4. Radiative Transfer Model

Radiative transfer calculations using the LibRadtran package [58,59] have been performed, aiming to simulate the atmospheric conditions and evaluate forecasts using different input variables. Using the pseudospherical disort radiative transfer equation solver [60], radiative transfer calculations every 1 nm were performed at 300–400 nm, for cloud-free conditions and including the absorption cross-sections of various species of this spectral region. The extraterrestrial solar spectrum with resolution of 1.0 nm provided by [61] was used as input, with summer mid-latitude standard atmospheric profiles [62] and the default aerosol model [63]. A triangular slit function with FWHM of 2.0 nm was used. Also, a correction for the sun–earth distance and the altitude of the instrument was included in order for the atmospheric parameters to be scaled accordingly. Finally, a climatological value of 0.03 for surface albedo at the UV spectral region was used. The single-scattering albedo (SSA) was set to the climatological value of 0.9, but during the dust event, the SSA was set to the more representative value of 0.86 for this type of aerosol in the UV spectral region based on the results of previous publications for the area under study [64,65]. The Ångström exponent was set to the climatological value of 1.2 [34] and for the period of the dust intrusion, it was set to 0.5. SZA was determined by astronomical calculations. Corresponding UVI was calculated by applying the erythema action spectrum to the output spectra using Equation (1).

3. Results and Discussion

Figure 1 shows the long-term variability of TOC in Athens, as retrieved from the BRS instrument for the period 2004–2019. Ranges of 1 and 2 σ around the mean daily value are highlighted. TOC measurements for 2020 are also shown and the period of the extremely low ozone event is found between 12 and 19 May. The mean TOC for the region for May is 346 ± 16 DU, while for this week in 2020, it dropped down to 280–295 DU. The seasonal TOC variation in Athens follows the mid-latitude behavior of stratospheric ozone, having maximum values during late winter–early spring and lower values at the end of summer and in autumn. As a threshold to characterize an extreme event, we have used the 2 σ of the TOC climatology. In a theoretical normal distribution, 95.5% of the values would have been in this range. This corresponds to ~1 day per month outside these limits. Thus, a period of

9 consecutive days below the limit has a very low possibility of occurring. Although the actual distribution of the values has some deviation from a theoretical normal distribution, it is safe to characterize this period as a very rare low ozone event for the region.

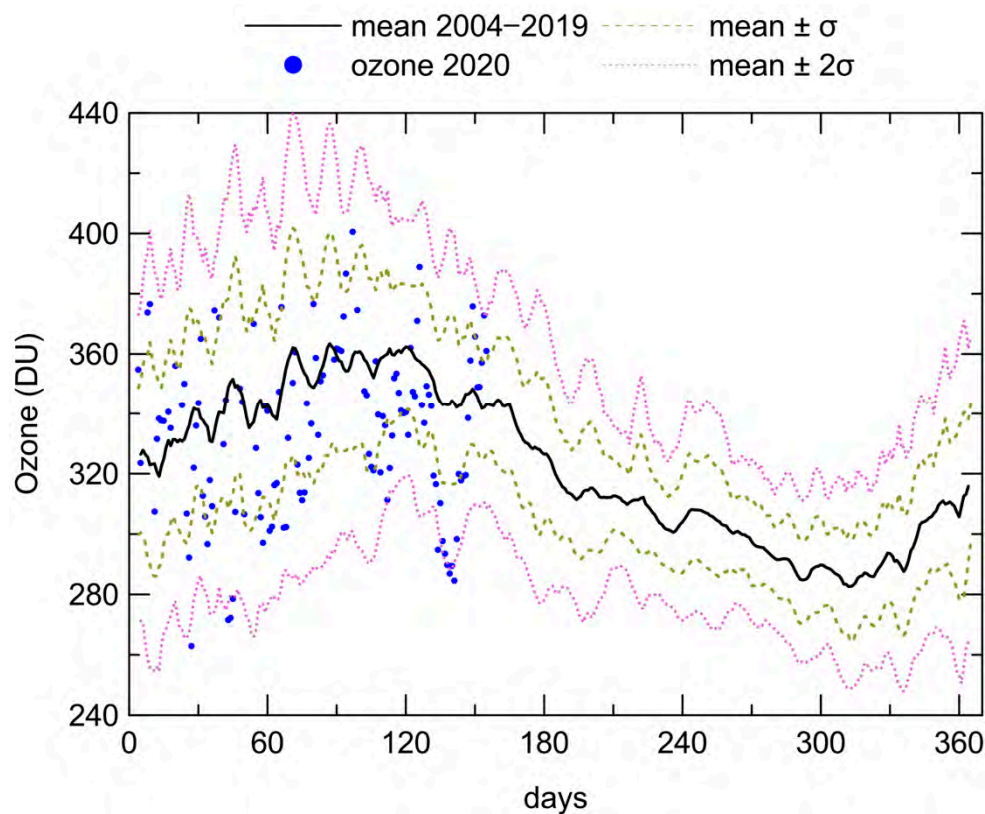


Figure 1. Daily average TOC at Athens, retrieved by BRS, for the period 2004–2019; 1 and 2 σ variations along with 2020 measured TOC values are also shown.

In order to understand the negative anomaly of TOC, maps of the Eastern Mediterranean, for 12–17 May, are presented in Figure 2. The anomaly could be triggered either by a local tropospheric air mass ascending in the stratosphere or the intrusion of a tropical stratospheric air mass. The picture of TOC in the area, during the event, shows that the zonal spatial distribution scheme [66] is broken by an intrusion from lower latitudes, which makes the transport of tropical air the most probable cause. These intrusions are mainly generated by gravitational and Rossby waves [67,68].

A synoptic analysis is performed with the use of Weather Research and Forecasting (WRF) model simulations at 12 km \times 12 km, driven by the National Centers for Environmental Prediction (NCEP) GFS global data. The regional atmospheric circulation during the reporting period is governed by the combination of a cut-off low over the western parts of Europe and a high-pressure ridge extending from the Sahara towards the eastern parts of Europe (Figure 3a). This type of weather favors the transport of dusty air masses from Africa towards Italy and the Balkans. The meridional intrusion of warmer air masses and the associated upwelling are evident from the increase in tropopause heights as shown, for example, in Figure 3b for 16 May 2020, explaining also the depletion of ozone in these areas that is evident in Figure 2.

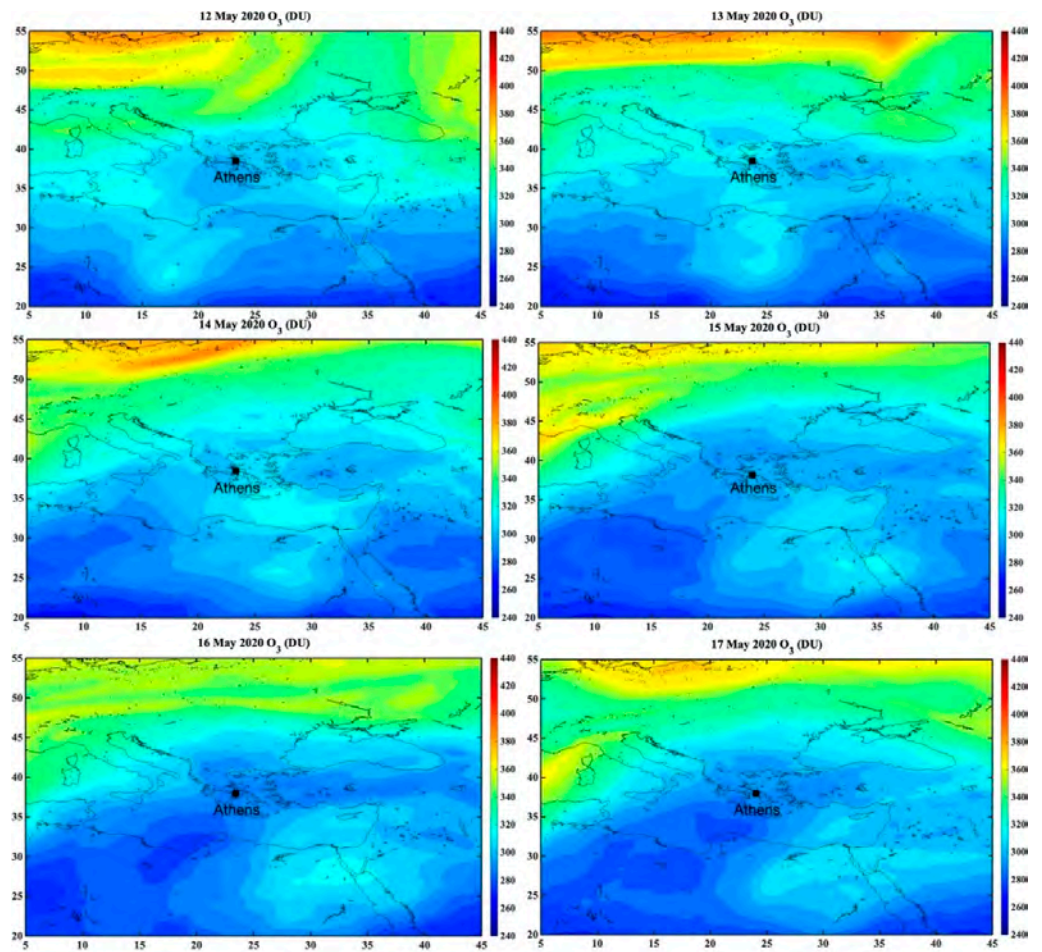


Figure 2. Spatial variability of TOC in the Eastern Mediterranean for 12–17 May 2020, as retrieved by the Copernicus Atmospheric Monitoring Service (CAMS).

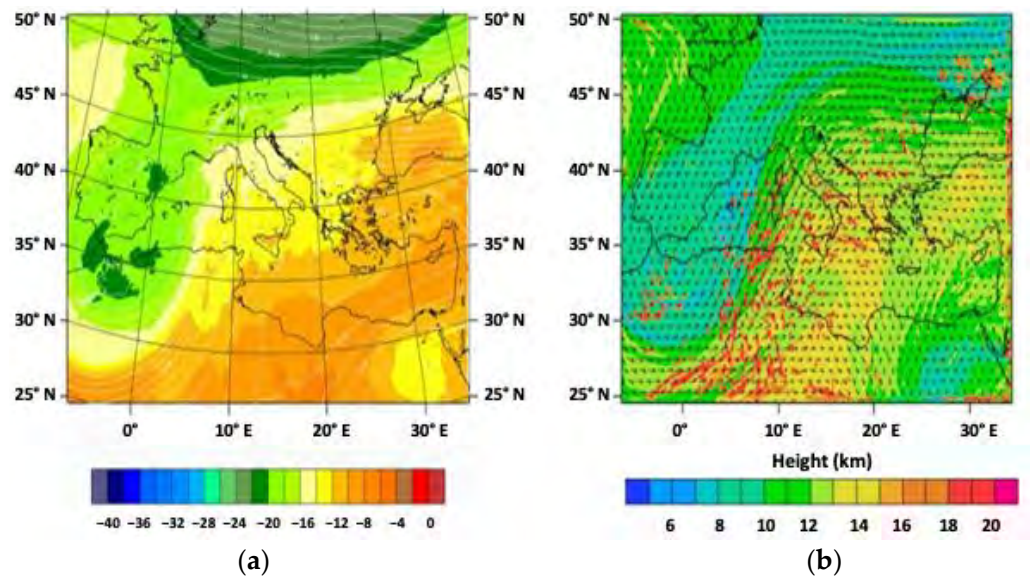


Figure 3. (a) Temperature and geopotential height at 500 mb on 16 May 2020, 12:00 UTC, by WRF. (b) Geopotential height and wind at tropopause on 16 May 2020, 18:00 UTC, by WRF.

Figure 4 shows the variation of UVI, TOC, and AOD during 12–19 May, 2020, as retrieved by the corresponding instruments. UVI was retrieved from the PSR measurements.

The higher UVI was recorded on the 19th of May, when the maximum value was 9.2. All the days after the 13th of May had a maximum UVI higher than 7.9. On the 12th of May, there were frequent overcast cloud conditions, which appear in the form of broken curves in the UVI. TOC from both BRS and OMI was constantly below the 2σ of the climatological mean during the whole period. The lowest values were reported on the 16th and the 17th of May. AOD was well below the climatological mean on the 13th of May. Starting that evening, an intrusion of Saharan dust reached Athens and very high values were recorded from the 14th to the 17th of May. On the last days, AOD was reduced and approached the mean climatological values. For 16–19 May, the UVI time series were sporadically affected by the presence of cirrus clouds. To avoid the effects of clouds, we selected to study further days that were strictly cloud-free based on PSR observations. Such cloudless conditions appear on May 13, 14, and 15. Based on all the above conditions, the days 13 and 15 of May were selected to be more intensively studied, as representative of cloudless days of low ozone and low aerosol (13/5), and low ozone and high aerosol (15/5). Data from 14/5 are later used to simulate the effects of low ozone and high AOD on the UV spectra.

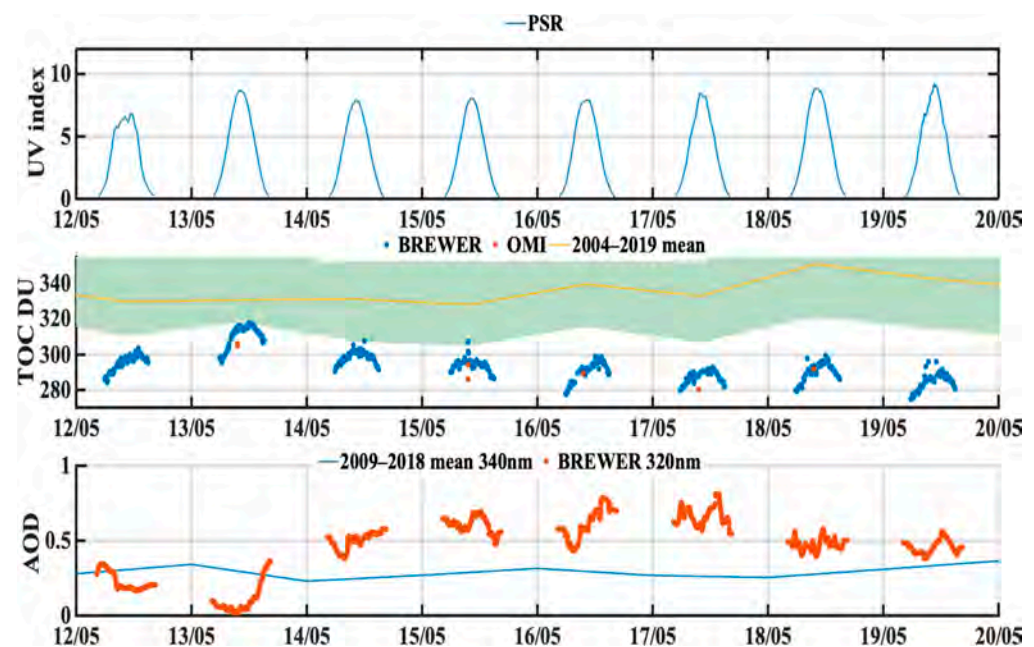


Figure 4. Variation of UVI as retrieved from the PSR measurements (**upper** plot). Variation of TOC as retrieved from BRS compared to OMI and average $\pm 2\sigma$ for the period, derived from BRS 2004–2019 data (**middle** plot). AOD at 320 nm as retrieved from BRS along with climatological average AOD at 340 nm as retrieved from AERONET for the period 2009–2018 (**lower** plot).

Figure 5 shows UVI retrieved from PSR on 13 May 2020, along with RTM simulations of UVI estimated with climatological TOC and AOD and BRS's AOD and TOC values. PSR-retrieved UVI was up to 11.2% (0.92 UVI) higher than the theoretical simulated with climatological TOC and AOD inputs. Using measured AOD and TOC, the agreement with the PSR has an $R^2 = 0.98$ and a mean bias error MBE = 0.11. Hence, the observed deviation from the theoretical climatological UVI can be explained by the variation of TOC and AOD. Mean AOD for the day was 0.22 (33.2%) lower than the climatological value and mean TOC was 32 DU lower (9.4%). Both these factors were contributing to higher UVI. Larger differences were observed around local noon, when UVI had the maximum value. For a large part of the day, absolute UVI differences were small and they started to differentiate when UVI became higher than 5. The following days, later in the week, had even lower ozone values, but not all of them were cloud-free and none of them had low AOD values. The maximum values of UVI are the ones usually reported to the general public and are

the ones with the largest differences. Modeled UVI assuming zero value for AOD show an overestimation of 8–12% (up to 0.9 UVI).

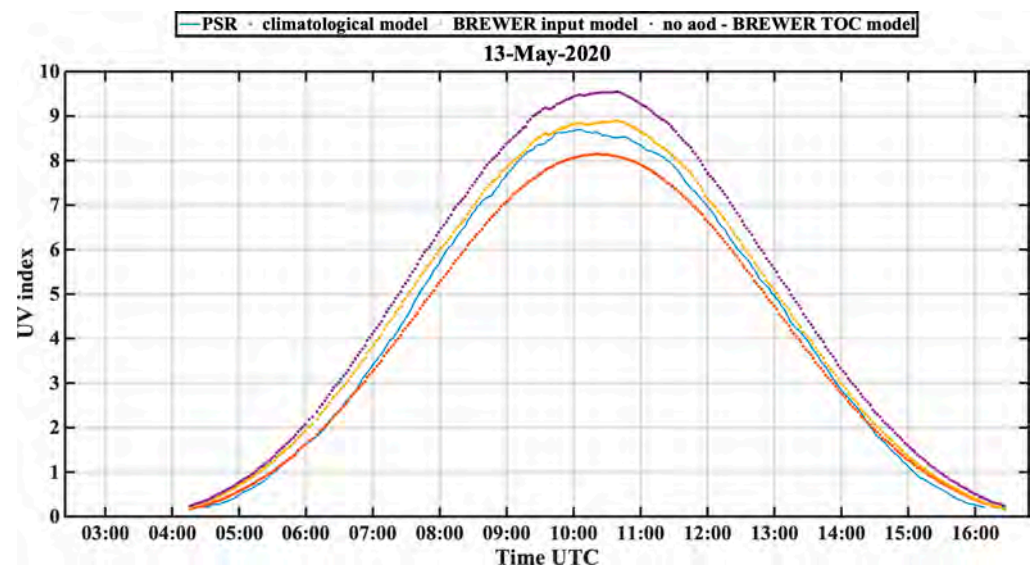


Figure 5. Diurnal variation of UVI on 13th of May 2020 as retrieved from the PSR measurements (blue curve), in comparison with modeled UVI predicted using RTM with climatological TOC and AOD inputs (orange dots) and modeled UVI using BRS AOD and TOC as input and modeled UVI using BRS TOC but zero aerosols.

On 15 May 2020, mean ozone was 43 DU lower than the climatological value. The purple curve in Figure 6 shows the theoretical UVI calculated with this TOC and without aerosols. Ozone at so low a range could lead to an increase of up to 28.5% of UVI (2.1 UVI), compared to the climatological estimations. On the other hand, mean AOD on this day was 0.31 (46.7%) higher than the climatological mean, which led to a decrease of UVI. As shown in Figure 7, simulation of UVI with climatological and measured TOC and AOD values were almost identical ($R^2 = 0.99$ and $MBE = 0.04$). PSR-retrieved UVI also agrees with these simulations ($R^2 = 0.99$ and $MBE = 0.06$). Hence, the two events had opposite effects on UVI, eliminating each other, leading to conditions similar to the climatological situation. We should conclude here that neglecting either effect of ozone or aerosols could lead to significant misestimation of UVI and erroneous recommendations to the general public.

In order to compare the spectral performance of the PSR and the model, UV spectra and their spectral ratio are shown in Figure 7 for May 15th. For this purpose, the RTM runs were set to $SSA = 0.86$ and Ångström exponent equal to 0.7. Model runs were performed for SZA in the range of 30° to 60° at 5° step, using AOD at 320 nm and TOC that corresponded to these SZAs. PSR measurements at these SZAs were averaged in a range of $\pm 0.5^\circ$. In Figure 7, the upper plots show the modeled and measured spectra that show a good agreement without any obvious absolute or spectral shifts. In Figure 7, the lower plot shows the ratio between the modeled and the measured spectra at seven different SZAs. The average ratio is 0.98 with $\sigma = 0.11$. This mean agreement of $\sim 2\%$ shows the relatively accurate use of the model inputs that simulate very well the synchronous measurements. The lowest mean ratio is observed at 60° , which is 0.94. The most variable spectral ratios are reported in the region below 305 nm, where the measured PSR irradiances are very low, including the highest uncertainties [41,42]. In this area, average ratios are from 0.76 ($SZA = 60^\circ$) to 1.12 ($SZA = 30^\circ$) with a $\sigma = 0.23$.

In Figure 8, modeled spectra at SZA of 30° and 60° are divided, from two separate RTM runs, using a constant climatological AOD (0.3) and different TOC, climatological (335 DU) and measured (292 DU as average for the 15th of May). At wavelengths higher than 330 nm, the ratio is constantly 1, where ozone has almost zero influence. At lower

spectral regions, the ratio becomes ~ 1.5 at 305 nm and towards the lower wavelength regions, the ratios become higher exponentially. It is clear from this figure that the UVA region is practically insensitive to TOC changes and UVB is highly sensitive and affects more the UVI. The average effect in the UVB region is a 32% increase in irradiance. This could lead to a 29% increase in the estimated UVI. The ratios depend on the SZA, as higher SZAs correspond to higher ozone attenuation.

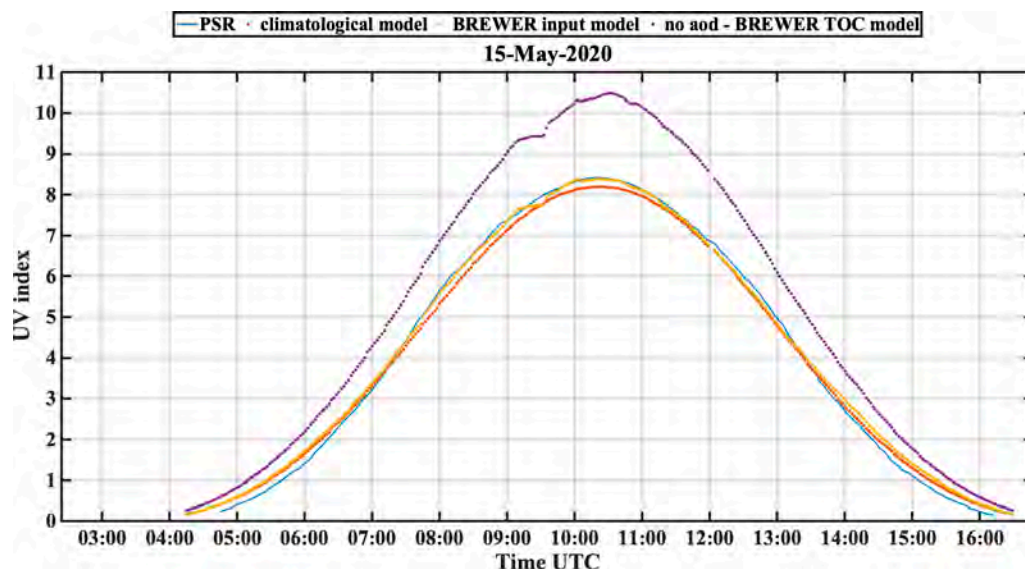


Figure 6. Diurnal variation of UVI on 15 May 2020 as retrieved from the PSR measurements, in comparison with modeled UVI predicted using: RTM with climatological TOC and AOD inputs, BRS AOD and TOC, BRS TOC without aerosols.

In Figure 9, in order to show the AOD effect, modeled spectral ratios of GHI simulated with $AOD = 0.5$ and $AOD = 0$ at $SZA = 30^\circ$ and 60° are presented. In all the above runs, TOC was set to the same climatological values (335 DU). These ratios are less spectral dependent and their absolute value depends on the AOD while their spectral change depends on the spectral characteristics of the aerosol attenuation (Ångström exponent). For these runs, an Ångström exponent of 0.7 was used, which is a representative value during dust intrusions in this area [60]. A different selection would alter the slope of the curves, as higher values result in a steeper increase of AOD with wavelength. Variation of the ratio, when SZA is 30° , is between 0.81 and 0.86 in the spectral region 300–400 nm. When SZA is higher, the attenuation due to aerosols is higher, resulting in a ratio between 0.75 and 0.77 for 60° SZA. Thus, the difference due to aerosols is very similar in UVA and UVB regions. AOD at 0.5 causes about 24% drop to the solar UV irradiance, which leads to a decrease of 28% of UVI. We should also highlight the importance of SSA in the calculations, since the type of the aerosols affects significantly the scattering/absorption characteristics of the radiative transfer simulations. The hypothesis for the UVI simulations shown earlier was that SSA during the dust event was 0.86 [64]. We also show in Figure 9 the range of the abovementioned ratios for SSA between 0.8 and 0.9. Lower limits of the range correspond to 0.8 SSA. Hence, in cases when the aerosol mixture is more absorbing, the influence of aerosol would be more effective. An erroneous assumption about the SSA could lead to deviations of the spectral ratio of $\pm 5\%$, propagating an uncertainty of 6% at UVI estimation. Also, in cases of higher AOD during dust events, the aerosol effect would be even more prominent. Finally, there is a small increase of the 60° related ratio for wavelengths below 305 nm. This is due to the fact that aerosol increase affects mainly direct irradiance so that for the specific wavelength range and solar angle, its contribution to the GHI is negligible, as diffuse irradiance is dominant. In this case, a small increase of the diffuse irradiance for higher aerosol load leads to the small increase of the ratio.

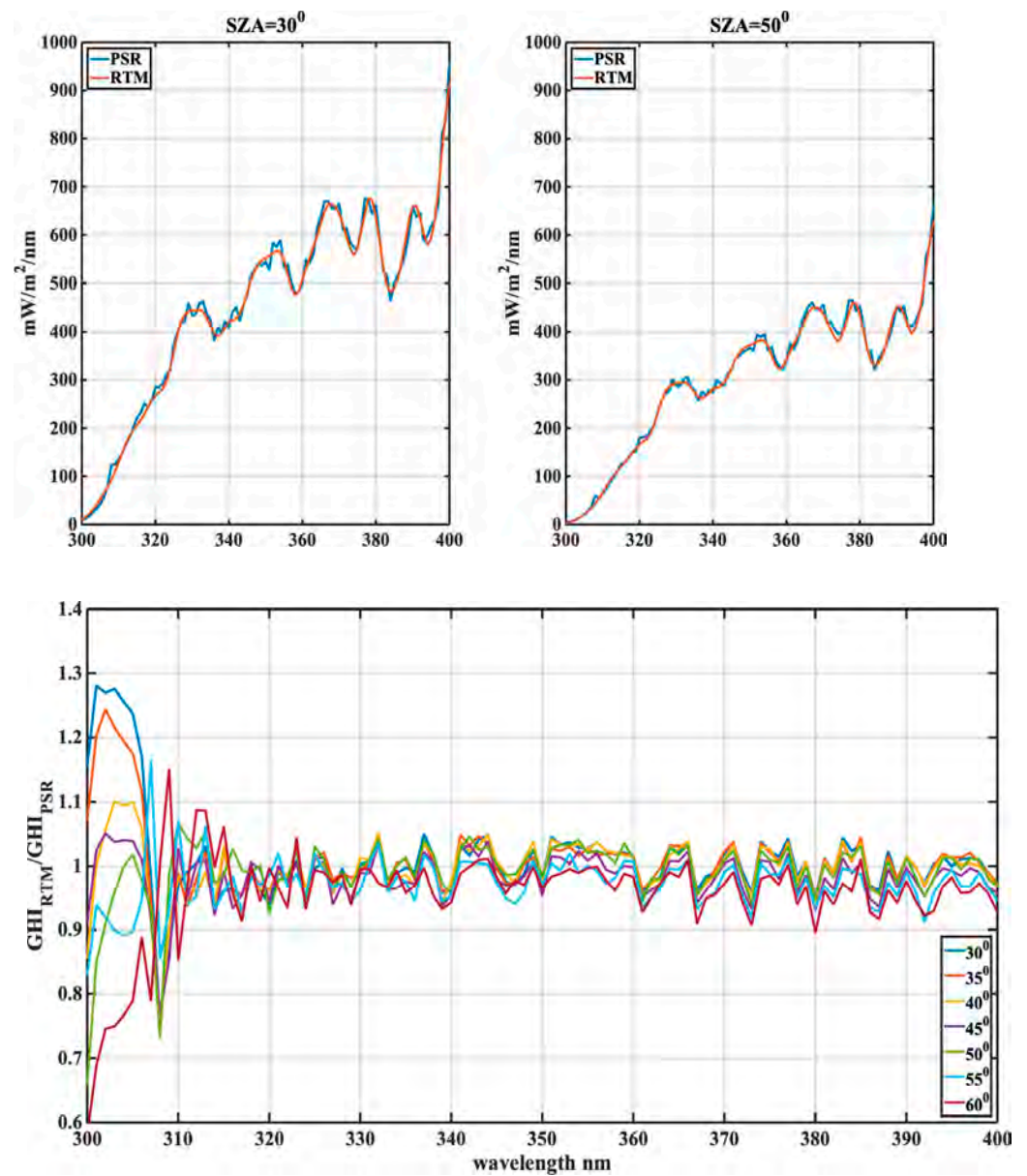


Figure 7. Upper plot modeled and measured with PSR GHI at SZA 30° and 50°. Lower plot, ratio of modeled to measured GHI, at seven different SZAs in the region 30°–60°.

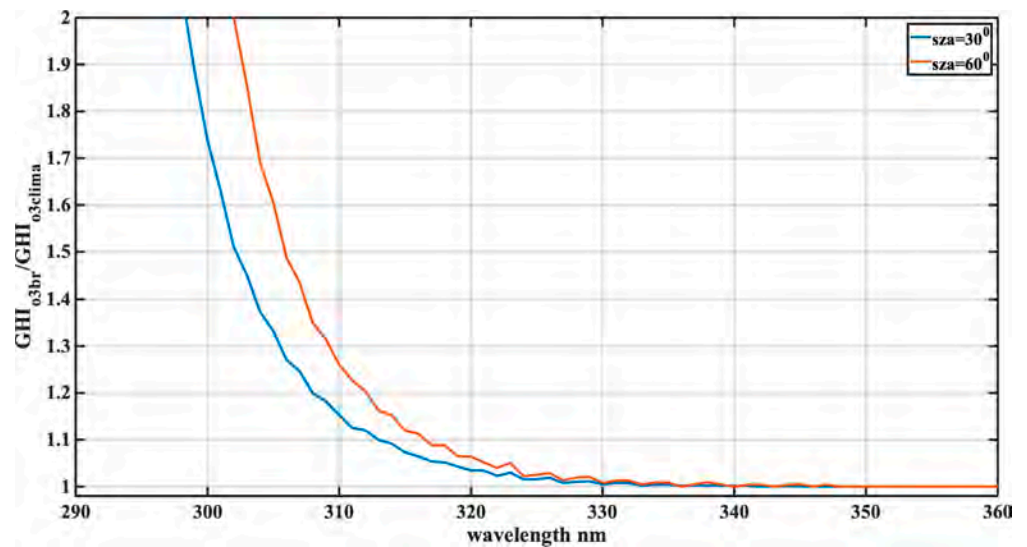


Figure 8. Ratio of modeled spectra in the UV region, as derived from RTM, with mean TOC measured by BRS on 15 May 2020, and climatological TOC, at two solar zenith angles.

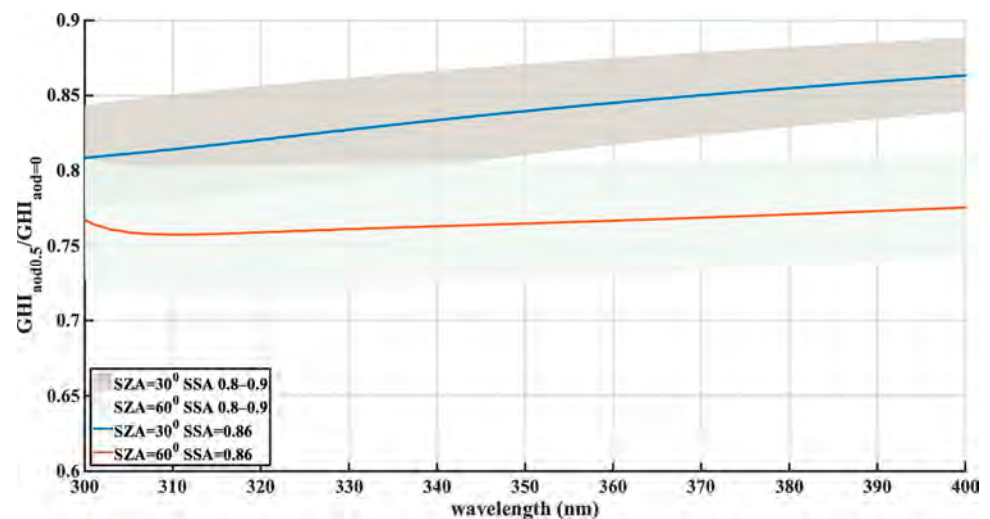


Figure 9. Ratio of modeled spectra in the UV region, as derived from RTM, with mean AOD measured by BRS on 14 May 2020 and no aerosols, at two solar zenith angles. The range of the ratios for different runs with SSA between 0.9 and 0.8 is shown.

4. Summary

During 12–19 May 2020, an extreme low TOC event was observed over the Athens area. TOC was lower than the climatological average (-2σ) for the whole week period. In addition, during some days AOD values were lower than the climatological average, while on others a dust aerosol intrusion was linked with AOD values almost double the May average for the area. Our analysis is confined to days that were strictly cloud-free in order to avoid the effect of cloudiness and study the effects of ozone and aerosols on the UV spectra and UVI.

On the 15th of May, which was a day with very low TOC and the highest AOD, theoretical calculations showed that TOC variation alone could cause an increase of $\sim 30\%$ in the UVI compared with the one retrieved using TOC climatological average. However, the aerosol presence masked this effect, contributing to a $\sim 20\%$ decrease during the dust intrusion.

Through RTM calculations, we have estimated that at 305 nm, when SZA is 30°, GHI, compared to the one with average AOD and TOC, will be 26% lower due to aerosols and 34% higher due to TOC decrease, while at 60° SZA, aerosols will attenuate GHI by 31% and ozone will increase it by 59%. Accordingly, at 325 nm, aerosols will cause 18% and 24% drop of GHI at 30° and 60° SZA, respectively, while ozone will increase it by 2% at both SZAs. We highlight that these estimates were derived using the measurements on the 14th of May 2020, a cloud-free day with AOD of 0.5 and mean daily ozone of 292 DU.

This study is investigating the parallel effects of factors affecting a health-related parameter such as the UVI. When studying the UVI dependence of TOC and AOD, it is important to focus on the different spectral regions, as ozone acts mainly in the UVB region, which also determines the largest part of UVI. Aerosols act more uniformly in the whole UV region and their spectral effect on solar irradiance is determined by the Ångström exponent. It should also be highlighted that ignoring intraday or day-to-day changes in either O₃ or aerosols when estimating UVI could lead to very high errors. Simultaneously occurring events (high/low TOC and AOD) that could mutually eliminate their effects are happening occasionally and having better knowledge on all these parameters will lead to better forecasting of UVI.

The case presented here is a demonstration of the combined effects of TOC and aerosols on a period with extremely low TOC. Changes in UVI under very low TOC events can be masked by high aerosol loads. Even if TOC is the major parameter affecting UVI, in this event, we saw that a moderate to high dust intrusion eliminated completely the very low TOC effect on the incoming UVI. Our findings demonstrate that aerosols and their optical properties (especially in the UVB) have a high impact on solar irradiance at UVB and have to be accurately known in order to simulate the UVI and inform the public objectively in the absence of accurate UV measurements.

Low ozone events might become more frequent in the future during spring, affecting UVB radiation at ground level. Butchart et al. [68] have analyzed different models and measurements for the meridional variation of ozone and concluded that under expected climatic changes, this kind of event will be more frequent. Hence, large TOC negative anomalies could be a major issue at mid-latitudes in the near future. Analyses of UVB radiation changes under extreme ozone conditions in combination with other natural events can contribute to better design of model simulations for future UVB projections.

Author Contributions: Conceptualization, I.-P.R., S.K.; Methodology, I.-P.R., S.K., K.E., S.S., K.P.; Software, P.K., I.-P.R., K.P., S.S.; Formal Analysis, I.-P.R., S.S.; Investigation, S.K., K.E.; Data Curation, I.-P.R., K.E.; Writing—Original Draft Preparation, I.-P.R., K.E.; Writing—Review & Editing, S.K., S.S., K.P.; Visualization, I.-P.R., K.E., S.S.; Funding Acquisition, S.K., K.E. All authors have read and agreed to the published version of the manuscript.

Funding: The research work was partially funded by the Hellenic Foundation for Research and Innovation (H.F.R.I.) under the “First Call for H.F.R.I. Research Projects to support Faculty members and Researchers and the procurement of high-cost research equipment grant” (Project Number: 300).

Institutional Review Board Statement: Not applicable.

Informed Consent Statement: Not applicable.

Data Availability Statement: PSR data are available on request from IPR. Brewer data are available on request from KE.

Acknowledgments: We acknowledge support and funding of this work by the project “Panhellenic Infrastructure for Atmospheric Composition and Climate Change” (MIS 5021516) which is implemented under the action “Reinforcement of the Research and Innovation Infrastructure”, funded by the Operational Program “Competitiveness, Entrepreneurship and Innovation” (NSRF 2014–2020) and co-financed by Greece and the European Union (European Regional Development Fund). S.K. and K.P. would like to acknowledge the European Commission project EuroGEO e-shape (grant agreement No 820852).

Conflicts of Interest: The authors declare no conflict of interest.

References

1. Solar Spectra by National Renewable Energy Laboratory of United States. Available online: <https://www.nrel.gov/grid/solar-resource/spectra.html> (accessed on 2 September 2020).
2. Juzeniene, A.; Brekke, P.; Dahlback, A.; Andersson-Engels, S.; Reichrath, J.; Moan, K.; Holick, M.F.; Grant, W.B.; Moan, J. Solar radiation and human health. *Rep. Prog. Phys.* **2011**, *74*, 66701. [[CrossRef](#)]
3. Lucas, R.; McMichael, T.; Smith, W.; Armstrong, B. Solar ultraviolet radiation: Global burden of disease from solar ultraviolet radiation. *Environ. Burd. Dis. Ser.* **2006**, *13*, 1–250.
4. Webb, A.R.; Kift, R.; Berry, J.L.; Rhodes, L.E. The vitamin D debate: Translating controlled experiments into reality for human sun exposure times. *Photochem. Photobiol.* **2011**, *87*, 741–745. [[CrossRef](#)]
5. Webb, A.R.; Engelsen, O. Calculated ultraviolet exposure levels for a healthy vitamin D status. *Photochem. Photobiol.* **2006**, *82*, 1697. [[CrossRef](#)] [[PubMed](#)]
6. McKenzie, R.; Blumthaler, M.; Diaz, S.; Fioletov, V.E.; Herman, J.R.; Seckmeyer, G.; Smedley, A.R.D.; Webb, A.R. *Rationalizing Nomenclature for UV Doses and Effects on Humans*; Report No. CIE 209:2014; CIE and WMO-GAW Joint Report: Geneva, Switzerland, 2014.
7. WMO Meeting of Experts on UV-B Measurements. *Data Quality and Standardization of UV Indices, 1994*; WMO: Geneva, Switzerland, 1995.
8. WHO and International Commission on Non-Ionizing Radiation Protection. *Global Solar UV Index: A Practical Guide*. Available online: <https://apps.who.int/iris/handle/10665/42459> (accessed on 23 January 2021).
9. Fioletov, V.; Kerr, J.B.; Fergusson, A. The UV index: Definition, distribution and factors affecting it. *Can. J. Public Health* **2010**, *101*, 15–19. [[CrossRef](#)]
10. Bais, A.F.; Lucas, R.M.; Bornman, J.F.; Williamson, C.E.; Sulzberger, B.; Austin, A.T.; Wilson, S.R.; Andrady, A.L.; Bernhard, G.; McKenzie, R.L.; et al. Environmental effects of ozone depletion, UV radiation and interactions with climate change: UNEP Environmental Effects Assessment Panel, update 2017. *Photochem. Photobiol. Sci.* **2018**, *17*, 127–179. [[CrossRef](#)]
11. Bais, A.F.; Bernhard, G.; McKenzie, R.L.; Aucamp, P.J.; Young, P.J.; Ilyas, M.; Jöckel, P.; Deushi, M. Ozone-climate interactions and effects on solar ultraviolet radiation. *Photochem. Photobiol. Sci.* **2019**, *18*, 602–640. [[CrossRef](#)]
12. McKenzie, R.L.; Aucamp, P.J.; Bais, A.F.; Björn, L.O.; Ilyas, M.; Madronich, S. Ozone depletion and climate change: Impacts on UV radiation. *Photochem. Photobiol. Sci.* **2011**, *10*, 182. [[CrossRef](#)]
13. Eleftheratos, K.; Kapsomenakis, J.; Zerefos, C.S.; Bais, A.F.; Fountoulakis, I.; Dameris, M.; Jöckel, P.; Haslerud, A.S.; Godin-Beekmann, S.; Steinbrecht, W.; et al. Possible effects of greenhouse gases to ozone profiles and DNA active UV-B irradiance at ground level. *Atmosphere* **2020**, *11*, 228. [[CrossRef](#)]
14. Bais, A.F.; Zerefos, C.S.; Meleti, C.; Ziomas, I.C.; Tourpali, K. Spectral measurements of solar UVB radiation and its relations to total ozone, SO₂, and clouds. *J. Geophys. Res.* **1993**, *98*, 5199–5204. [[CrossRef](#)]
15. Kerr, J.B.; McElroy, C.T. Evidence for large upward trends of ultraviolet-B radiation linked to ozone depletion. *Science* **1993**, *262*, 1032–1034. [[CrossRef](#)] [[PubMed](#)]
16. Kuttippurath, J.; Nair, P.J. The signs of Antarctic ozone hole recovery. *Sci. Rep.* **2017**, *7*, 1–8. [[CrossRef](#)] [[PubMed](#)]
17. Zerefos, C.S.; Tourpali, K.; Eleftheratos, K.; Kazadzis, S.; Meleti, C.; Feister, U.; Koskela, T.; Heikkilä, A. Evidence of a possible turning point in solar UV-B over Canada, Europe and Japan. *Atmos. Chem. Phys.* **2012**, *12*, 2469–2477. [[CrossRef](#)]
18. Kazadzis, S.; Kouremeti, N.; Bais, A.; Kazantzidis, A.; Meleti, C. Aerosol forcing efficiency in the UVA region from spectral solar irradiance measurements. *Ann. Geophys.* **2009**, *27*, 2515–2522. [[CrossRef](#)]
19. Di Sarra, A.; Cacciani, M.; Chamard, P.; Cornwall, C.; DeLuisi, J.J.; Di Iorio, T.; Disterhoft, P.; Fiocco, G.; Fua, D.; Monteleone, F. Effects of desert dust and ozone on the ultraviolet irradiance at the Mediterranean island of Lampedusa during PAUR II. *J. Geophys. Res. Atmos.* **2002**, *107*, PAU 2-1–PAU 2-14. [[CrossRef](#)]
20. Román, R.; Antón, M.; Valenzuela, A.; Gil, J.E.; Lyamani, H.; De Miguel, A.; Olmo, F.J.; Bilbao, J.; Alados-Arboledas, L. Evaluation of the desert dust effects on global, direct and diffuse spectral ultraviolet irradiance. *Tellus B Chem. Phys. Meteorol.* **2013**, *65*, 19578. [[CrossRef](#)]
21. Barnard, W.F.; Saxena, V.K.; Wenny, B.N.; DeLuisi, J.J. Daily surface UV exposure and its relationship to surface pollutant measurements. *J. Air Waste Manag. Assoc.* **2003**, *53*, 237–245. [[CrossRef](#)]
22. Mok, J.; Krotkov, N.A.; Torres, O.; Jethva, H.; Li, Z.; Kim, J.; Koo, J.H.; Go, S.; Irie, H.; Labow, G.; et al. Comparisons of spectral aerosol single scattering albedo in Seoul, South Korea. *Atmos. Meas. Tech.* **2018**, *11*, 2295–2311. [[CrossRef](#)]
23. Papayannis, A.; Mamouri, R.E.; Amiridis, V.; Kazadzis, S.; Pérez, G.; Tsaknakis, G.; Kokkalis, P. Systematic lidar observations of Saharan dust layers over Athens, Greece in the frame of EARLINET project (2004–2006). *Ann. Geophys.* **2009**, *27*, 3611–3620. [[CrossRef](#)]
24. Kosmopoulos, P.G.; Kazadzis, S.; Taylor, M.; Athanasopoulou, E.; Speyer, O.; Raptis, P.I.; Marinou, E.; Proestakis, E.; Solomos, S.; Gerasopoulos, E.; et al. Dust impact on surface solar irradiance assessed with model simulations, satellite observations and ground-based measurements. *Atmos. Meas. Tech.* **2017**, *10*, 2435–2453. [[CrossRef](#)]
25. Solomos, S.; Kalivitis, N.; Mihalopoulos, N.; Amiridis, V.; Kouvarakis, G.; Gkikas, A.; Biniotoglou, I.; Tsekeri, A.; Kazadzis, S.; Kottas, M.; et al. From tropospheric folding to khamsin and foehn winds: How atmospheric dynamics advanced a record-breaking dust episode in crete. *Atmosphere* **2018**, *9*, 240. [[CrossRef](#)]

26. Seckmeyer, G.; Pissulla, D.; Glandorf, M.; Henriques, D.; Johnsen, B.; Webb, A.; Siani, A.M.; Bais, A.; Kjeldstad, B.; Brogniez, C.; et al. Variability of UV irradiance in Europe. *Photochem. Photobiol.* **2008**, *84*, 172–179. [[CrossRef](#)] [[PubMed](#)]
27. Blumthaler, M.; Ambach, W.; Ellinger, R. Increase in solar UV radiation with altitude. *J. Photochem. Photobiol. B Biol.* **1997**, *39*, 130–134. [[CrossRef](#)]
28. Fountoulakis, I.; Diémoz, H.; Siani, A.M.; Laschewski, G.; Filippa, G.; Arola, A.; Bais, A.F.; De Backer, H.; Lakkala, K.; Webb, A.R.; et al. Solar UV irradiance in a changing climate: Trends in Europe and the significance of spectral monitoring in Italy. *Environments* **2020**, *7*, 1. [[CrossRef](#)]
29. Eleftheratos, K.; Kazadzis, S.; Zerefos, C.S.; Tourpali, K.; Meleti, C.; Balis, D.; Zyrichidou, I.; Lakkala, K.; Feister, U.; Koskela, T.; et al. Ozone and spectroradiometric UV changes in the past 20 years over high latitudes. *Atmos. Ocean* **2015**, *53*, 117–125. [[CrossRef](#)]
30. Allaart, M.; van Weele, M.; Fortuin, P.; Kelder, H. An empirical model to predict the UV-index based on solar zenith angles and total ozone. *Meteorol. Appl.* **2004**, *11*, 59–65. [[CrossRef](#)]
31. Zempila, M.M.; Koukoulis, M.E.; Bais, A.; Fountoulakis, I.; Arola, A.; Kouremeti, N.; Balis, D. OMI/Aura UV product validation using NILU-UV ground-based measurements in Thessaloniki, Greece. *Atmos. Environ.* **2016**, *140*, 283–297. [[CrossRef](#)]
32. Gerasopoulos, E.; Kokkalis, P.; Amiridis, V.; Liakakou, E.; Perez, C.; Haustein, K.; Eleftheratos, K.; Andreae, M.O.; Andreae, T.W.; Zerefos, C.S. Dust specific extinction cross-sections over the Eastern Mediterranean using the BSC-DREAM model and sun photometer data: The case of urban environments. *Ann. Geophys.* **2009**, *27*, 2903–2912. [[CrossRef](#)]
33. Amiridis, V.; Zerefos, C.; Kazadzis, S.; Gerasopoulos, E.; Eleftheratos, K.; Vrekoussis, M.; Stohl, A.; Mamouri, R.; Kokkalis, P.; Papayannis, A. Impact of the 2009 Attica wild fires on the air quality in urban Athens. *Atmos. Environ.* **2012**, *46*, 536–544. [[CrossRef](#)]
34. Raptis, I.P.; Kazadzis, S.; Amiridis, V.; Gkikas, A.; Gerasopoulos, E.; Mihalopoulos, N. A decade of aerosol optical properties measurements over Athens, Greece. *Atmosphere* **2020**, *11*, 154. [[CrossRef](#)]
35. Schmalwieser, A.W.; Gröbner, J.; Blumthaler, M.; Klotz, B.; De Backer, H.; Bolsée, D.; Werner, R.; Tomsic, D.; Metelka, L.; Eriksen, P.; et al. UV Index monitoring in Europe. *Photochem. Photobiol. Sci.* **2017**, *16*, 1349–1370. [[CrossRef](#)] [[PubMed](#)]
36. Gröbner, J.; Sperfeld, P. Direct traceability of the portable QASUME irradiance scale to the primary irradiance standard of the PTB. *Metrologia* **2005**, *42*, 134. [[CrossRef](#)]
37. Hülsen, G.; Gröbner, J.; Bais, A.; Blumthaler, M.; Diémoz, H.; Bolsée, D.; Diaz, A.; Fountoulakis, I.; Naranen, E.; Schreder, J.; et al. Second solar ultraviolet radiometer comparison campaign UVC-II. *Metrologia* **2020**, *57*, 035001. [[CrossRef](#)]
38. Verdebout, J. A European satellite-derived UV climatology available for impact studies. *Radiat. Prot. Dosimetry* **2004**, *111*, 407–411. [[CrossRef](#)] [[PubMed](#)]
39. Herman, J.R. Global increase in UV irradiance during the past 30 years (1979–2008) estimated from satellite data. *J. Geophys. Res. Atmos.* **2010**, *115*. [[CrossRef](#)]
40. Gröbner, J.; Kouremeti, N. The Precision Solar Spectroradiometer (PSR) for direct solar irradiance measurements. *Sol. Energy* **2019**, *185*, 199–210. [[CrossRef](#)]
41. Raptis, P.I.; Kazadzis, S.; Gröbner, J.; Kouremeti, N.; Doppler, L.; Becker, R.; Helmig, C. Water vapour retrieval using the Precision Solar Spectroradiometer. *Atmos. Meas. Tech.* **2018**, *11*, 1143–1157. [[CrossRef](#)]
42. Webb, A.R. Who, what, where and when—Influences on cutaneous vitamin D synthesis. *Prog. Biophys. Mol. Biol.* **2006**, *92*, 17–25. [[CrossRef](#)]
43. Kerr, J.B.; McElroy, C.T.; Olafson, R.A. Measurements of ozone with the Brewer ozone spectrophotometer. In Proceedings of the Quadrennial Ozone Symposium, Boulder, CO, USA, 4–9 August 1981; London, J., Ed.; National Center for Atmospheric Research: Boulder, CO, USA; pp. 74–79.
44. Kazantzidis, A.; Bais, A.F.; Zempila, M.M.; Meleti, C.; Eleftheratos, K.; Zerefos, C. Evaluation of ozone column measurements over Greece with NILU-UV multi-channel radiometers. *Int. J. Remote Sens.* **2009**, *30*, 4273–4281. [[CrossRef](#)]
45. Raptis, P.; Kazadzis, S.; Eleftheratos, K.; Kosmopoulos, P.; Amiridis, V.; Helmig, C.; Zerefos, C. Total ozone column measurements using an ultraviolet multifilter radiometer. *International J. Remote Sens.* **2015**, *36*, 4469–4482. [[CrossRef](#)]
46. Diémoz, H.; Eleftheratos, K.; Kazadzis, S.; Amiridis, V.; Zerefos, C.S. Retrieval of aerosol optical depth in the visible range with a Brewer spectrophotometer in Athens. *Atmos. Meas. Tech.* **2016**, *9*, 1871–1888. [[CrossRef](#)]
47. Zerefos, C.S.; Eleftheratos, K.; Kapsomenakis, J.; Solomos, S.; Inness, A.; Balis, D.; Redondas, A.; Eskes, H.; Allaart, M.; Amiridis, V.; et al. Detecting volcanic sulfur dioxide plumes in the Northern Hemisphere using the Brewer spectrophotometers, other networks, and satellite observations. *Atmos. Chem. Phys.* **2017**, *17*, 551–574. [[CrossRef](#)]
48. Gröbner, J.; Meleti, C. Aerosol optical depth in the UVB and visible wavelength range from Brewer spectrophotometer direct irradiance measurements: 1991–2002. *J. Geophys. Res.* **2004**, *109*, D09202. [[CrossRef](#)]
49. Staehelin, J.; Kerr, J.; Evans, R.; Vanicek, K. *Comparison of Total Ozone Measurements of Dobson and Brewer Spectrophotometers and Recommended Transfer Functions*; World Meteorological Organization: Geneva, Switzerland, 2003.
50. Available online: <http://www.o3soft.eu/o3Brewer.html> (accessed on 10 August 2020).
51. Bhartia, P.K.; Wellemeyer, C. TOMS-V8 total O₃ algorithm. *OMI Algorithm Theor. Basis Doc.* **2002**, *2*, 15–31.
52. Veefkind, J.P.; de Haan, J.F.; Brinksma, E.J.; Kroon, M.; Levelt, P.F. Total ozone from the Ozone Monitoring Instrument (OMI) using the DOAS technique. *IEEE Trans. Geosci. Remote. Sens.* **2006**, *44*, 1239–1244. [[CrossRef](#)]

53. Huijnen, V.; Miyazaki, K.; Flemming, J.; Inness, A.; Sekiya, T.; Schultz, M.G. An intercomparison of tropospheric ozone reanalysis products from CAMS, CAMS interim, TCR-1, and TCR-2. *Geosci. Model Dev.* **2020**, *13*, 1513–1544. [[CrossRef](#)]
54. Balis, D.; Kroon, M.; Koukouli, M.E.; Brinkma, E.J.; Labow, G.; Veefkind, J.P.; McPeters, R.D. Validation of Ozone Monitoring Instrument total ozone column measurements using Brewer and Dobson spectrophotometer ground-based observations. *J. Geophys. Res. Atmos.* **2007**, *112*, D24. [[CrossRef](#)]
55. Fioletov, V.E.; Labow, G.; Evans, R.; Hare, E.W.; Köhler, U.; McElroy, C.T.; Miyagawa, K.; Redondas, A.; Savastouk, V.; Shalamyansky, A.M.; et al. Performance of the ground-based total ozone network assessed using satellite data. *J. Geophys. Res. Atmos.* **2008**, *113*, D14. [[CrossRef](#)]
56. McPeters, R.; Kroon, M.; Labow, G.; Brinkma, E.; Balis, D.; Petropavlovskikh, I.; Veefkind, J.P.; Bhartia, P.K.; Levelt, P.F. Validation of the Aura Ozone Monitoring Instrument total column ozone product. *J. Geophys. Res.* **2008**, *113*, D15S14. [[CrossRef](#)]
57. Meloni, D.; Di Sarra, A.; Herman, J.R.; Monteleone, F.; Piacentino, S. Comparison of ground-based and Total Ozone Mapping Spectrometer erythemal UV doses at the island of Lampedusa in the period 1998–2003: Role of tropospheric aerosols. *J. Geophys. Res. Atmos.* **2005**, *110*. [[CrossRef](#)]
58. Mayer, B.; Kylling, A. Technical note: The libRadtran software package for radiative transfer calculations—Description and examples of use. *Atmos. Chem. Phys.* **2005**, *5*, 1855–1877. [[CrossRef](#)]
59. Emde, C.; Buras-Schnell, R.; Kylling, A.; Mayer, B.; Gasteiger, J.; Hamann, U.; Kylling, J.; Richter, B.; Pause, C.; Dowling, T.; et al. The libradtran software package for radiative transfer calculations (version 2.0.1). *Geosci. Model Dev.* **2016**, *9*, 1647–1672. [[CrossRef](#)]
60. Dahlback, A.; Stamnes, K. A new spherical model for computing the radiation field available for photolysis and heating at twilight. *Planet. Space Sci.* **1991**, *39*, 671–683. [[CrossRef](#)]
61. Kurucz, R.L.; Rabin, D.M.; Jefferies, J.T. Synthetic infrared spectra. In Proceedings of the IAU Symposium on Infrared Solar Physics, Kluwer Academic Norwell, MA, USA, 2–5 March 1992.
62. Anderson, G.; Clough, S.; Kneizys, F.; Chetwynd, J.; Shettle, E. *AFGL Atmospheric Constituent Profiles (0–120 km)*; Tech. Rep. AFGL-TR-86-0110; Air Force Geophysical Laboratory, Hanscom Air Force Base: Bedford, MA, USA, 1986.
63. Shettle, E. Models of aerosols, clouds and precipitation for atmospheric propagation studies. In Proceedings of the Atmospheric Propagation in the UV, Visible, IR and MM Wave Region and Related Systems and Aspects, Copenhagen, Denmark, 9–13 October 1989.
64. Raptis, P.-I.; Kazadzis, S.; Eleftheratos, K.; Amiridis, V.; Fountoulakis, I. Single scattering Albedo's spectral dependence effect on UV irradiance. *Atmosphere* **2018**, *9*, 364. [[CrossRef](#)]
65. Kazadzis, S.; Raptis, P.; Kouremeti, N.; Amiridis, V.; Arola, A.; Gerasopoulos, E.; Schuster, G.L. Aerosol absorption retrieval at ultraviolet wavelengths in a complex environment. *Atmos. Meas. Tech.* **2016**, *9*, 5997. [[CrossRef](#)]
66. Plumb, R.A.; Eluszkiewicz, J. The Brewer–Dobson circulation: Dynamics of the tropical upwelling. *J. Atmos. Sci.* **1999**, *56*, 868–890. [[CrossRef](#)]
67. Sato, K.; Hirano, S. The climatology of the Brewer–Dobson circulation and the contribution of gravity waves. *Atmos. Chem. Phys.* **2019**, *19*, 4517–4539. [[CrossRef](#)]
68. Butchart, N.; Scaife, A.A.; Bourqui, M.; De Grandpré, J.; Hare, S.H.E.; Kettleborough, J.; Langematz, U.; Manzini, E.; Sassi, F.; Shibata, K.; et al. Simulations of anthropogenic change in the strength of the Brewer–Dobson circulation. *Clim. Dyn.* **2006**, *27*, 727–741. [[CrossRef](#)]

Article

Sixteen Years of Measurements of Ozone over Athens, Greece with a Brewer Spectrophotometer

Kostas Eleftheratos ^{1,2,*} , Dimitra Kouklaki ¹ and Christos Zerefos ^{2,3,4}

¹ Department of Geology and Geoenvironment, National and Kapodistrian University of Athens, 15784 Athens, Greece; dkouklaki@geol.uoa.gr

² Biomedical Research Foundation of the Academy of Athens, 11527 Athens, Greece; zerefos@geol.uoa.gr

³ Research Centre of Atmospheric Physics and Climatology, Academy of Athens, 10680 Athens, Greece

⁴ Navarino Environmental Observatory (N.E.O.), 24001 Messenia, Greece

* Correspondence: kelef@geol.uoa.gr; Tel.: +30-210-7274133

Abstract: Sixteen years (July 2003–July 2019) of ground-based measurements of total ozone in the urban environment of Athens, Greece, are analyzed in this work. Measurements were acquired with a single Brewer monochromator operating on the roof of the Biomedical Research Foundation of the Academy of Athens since July 2003. We estimate a 16-year climatological mean of total ozone in Athens of about 322 DU, with no significant change since 2003. Ozone data from the Brewer spectrophotometer were compared with TOMS, OMI, and GOME-2A satellite retrievals. The results reveal excellent correlations between the ground-based and satellite ozone measurements greater than 0.9. The variability of total ozone over Athens related to the seasonal cycle, the quasi biennial oscillation (QBO), the El Niño Southern Oscillation (ENSO), the North Atlantic Oscillation (NAO), the 11-year solar cycle, and tropopause pressure variability is presented.

Keywords: ozone; variability; measurements; Brewer spectrophotometer; satellite data; tropopause pressure



Citation: Eleftheratos, K.; Kouklaki, D.; Zerefos, C. Sixteen Years of Measurements of Ozone over Athens, Greece with a Brewer Spectrophotometer. *Oxygen* **2021**, *1*, 32–45. <https://doi.org/10.3390/oxygen1010005>

Academic Editor: Klemens Hocke

Received: 18 May 2021

Accepted: 2 August 2021

Published: 3 August 2021

Publisher's Note: MDPI stays neutral with regard to jurisdictional claims in published maps and institutional affiliations.



Copyright: © 2021 by the authors. Licensee MDPI, Basel, Switzerland. This article is an open access article distributed under the terms and conditions of the Creative Commons Attribution (CC BY) license (<https://creativecommons.org/licenses/by/4.0/>).

1. Introduction

Ozone is a minor natural component of the clean atmosphere, found primarily in two regions. Approximately 10% of the Earth's atmospheric ozone resides in the troposphere, while 90% is found in the stratosphere (commonly referred to as the “ozone layer”) [1]. Year-to-year fluctuations in total ozone are determined by the balance between chemical processes that produce and destroy ozone and the effects of atmospheric motions that transport ozone [2]. Certain industrial processes and human activities are the root cause of the release of ozone-depleting substances (ODSs) into the atmosphere. ODSs are manufactured halogen source gases that are controlled worldwide by the Montreal Protocol.

Concern about changes in ozone abundance is an important subject, not only for the scientific community, but the general public and governments as well. The importance of observational and modeling results about ozone trends lies in its tremendous importance for the life and ecosystems at the location under investigation [3]. Changes in stratospheric ozone can change the large-scale atmospheric state, influencing the climate, both directly through radiative effects, and indirectly by affecting stratospheric and tropospheric circulation [4].

Total ozone measurements have been conducted in Athens, Greece, since 1989, with a Dobson spectrophotometer No 118, which is part of the World Ozone and UV Data Centre (WOUDC) of the WMO [5]. The authors found a correlation coefficient of 0.96 with Total Ozone Mapping Spectrometer (TOMS) data, although the TOMS values were slightly lower than the Dobson ones. The Dobson measurements were also compared with TOMS (version 6) and solar backscatter ultraviolet radiometer (SBUV) measurements, and better correlations were obtained on sunny days [6]. Long-term measurements of stratospheric

ozone in Greece have also been conducted in Thessaloniki since 1982, with a MKII Brewer spectrophotometer #005 [7].

The aim of this study was the estimation of the variability and trends of total ozone over Athens, Greece, from a Brewer spectrophotometer operating in Athens since July 2003. This research contributes to developing understanding of the processes that control ozone abundance. The ozone data set from the Brewer spectrophotometer is compared with TOMS, Ozone Monitoring Instrument (OMI), and Global Ozone Monitoring Experiment 2 (GOME-2A and GOME-2B) satellite retrievals. This is the first time we have analyzed long-term ground-based measurements of total ozone in Athens with the Brewer spectrophotometer. The measurements cover the period 2003–2019; i.e., after the ozone decline of the 1980s and 1990s [8]. Detailed information on the data sources and methods are provided in Section 2. In Section 3, daily values, correlations, and monthly mean total ozone time series, as well as the ozone variability, are presented and described in detail. Finally, Section 4 provides concluding remarks on the main findings of this study.

2. Data Sources and Methods

In this study, we used measurements of total ozone column, made using a single Brewer MKIV spectrophotometer. This Brewer #001 monochromator has measured the columnar amount of ozone in Athens on a daily basis, since July 2003. The measurements are conducted on the roof of the Biomedical Research Foundation of the Academy of Athens (37.99° N, 23.78° E) at approximately 180 m a.s.l. [9]. The institute is located in a green area at about 4 km, away from the city center. On the east side of the station is mountain Hymettus, at a distance of about 1 km, and to the north and northeast of the station we find the large mountains of the county of Attica, Parnes, and Penteli, at distances of about 15 and 20 km from the station, respectively. Finally, to the south, the Saronic Gulf is about 10 km away [10].

The Brewer is an automated, diffraction-grating spectrometer that provides observations of the sun's intensity in the near UV range. The instrument measures the intensity of radiation in the UV absorption spectrum of ozone at five wavelengths (306.3, 310.1, 313.5, 316.8, and 320.1 nm) with a resolution of 0.5 nm. These data are used to derive columnar ozone and sulfur dioxide amounts and the aerosol optical depth [11]. The total ozone column (TOC) is calculated as follows [12]:

$$\text{TOC} = \frac{F_0 - F - \Delta\beta m}{\Delta\alpha \mu} \quad (1)$$

where F is the weighted ratio of direct sun measurements at 4 spectral channels, i.e.,

$$F = \log I_{(310.1)} - 0.5 \log I_{(313.5)} - 2.2 \log I_{(316.8)} + 1.7 \log I_{(320.1)} \quad (2)$$

F_0 , $\Delta\beta$, and $\Delta\alpha$ are the same linear combinations for $\log I_{0(\lambda)}$, β_λ , and α_λ , i.e.,

$$F_0 = \log I_{0(310.1)} - 0.5 \log I_{0(313.5)} - 2.2 \log I_{0(316.8)} + 1.7 \log I_{0(320.1)} \quad (3)$$

$$\Delta\beta = \beta_{(310.1)} - 0.5 \beta_{(313.5)} - 2.2 \beta_{(316.8)} + 1.7 \beta_{(320.1)} \quad (4)$$

$$\Delta\alpha = \alpha_{(310.1)} - 0.5 \alpha_{(313.5)} - 2.2 \alpha_{(316.8)} + 1.7 \alpha_{(320.1)} \quad (5)$$

β_λ is the Rayleigh scattering coefficient at λ , m is the effective pathlength of direct radiation through air, α_λ is the ozone absorption coefficient at λ , and μ is the ratio of the effective pathlength of direct radiation through ozone to the vertical path. The extra-terrestrial constants F_0 are determined from a long series of intercomparison measurements, as well as zero air mass (μ) extrapolations.

The instrument is calibrated regularly by the travelling standard Brewer #017, which is operated by International Ozone Services Inc., Toronto, Ontario, Canada (www.io3.ca) (last access: 3 August 2021). Calibrations of the Brewer #001 were performed in Thessaloniki in July 2002 and on site in Athens in July 2004, June 2007, September 2010, October 2013, and

September 2019. Information about the stability of the instrument obtained from the results of the calibrations is presented in the Supplementary Materials of this study. Internal standard lamp tests are performed on a daily basis to detect possible instrumental drifts. Ozone data are recalculated after standard lamp test corrections and are analyzed using the O3BREWERS data management software [13]. We note here that the Brewer #001 ozone data have been used in the past to evaluate NILU–UV multi-channel radiometer ozone data [14] and ultraviolet multifilter radiometer (UV-MFR) ozone retrievals [15].

The effect of stray light [16] or the effect of temperature dependence [17] may result in errors in the Brewer UV measurements and, consequently, in ozone retrievals. It is known that ozone measurements from a single monochromator Brewer spectrophotometers suffer from non-linearity at large ozone slant column amounts, due to the presence of instrumental stray light caused by scattering within the optics of the instrument. As the light path (air mass) through ozone increases, the effect of stray light on the measurements also increases [18]. In our study, in order to avoid any possible erroneous measurements at large solar zenith angles, we processed ozone measurements up to 70 solar zenith angles. Regarding the temperature dependence effect, there is no stratospheric temperature correction of ozone absorption coefficients in the latest version of the O3Brewer software which we used. At this point, it is worth mentioning that only direct sun (DS) measurements were processed to retrieve the daily TOC values; hence, measurements in the zenith sky scattered mode have not been considered.

In this study we compare the Brewer ground-based ozone data with satellite ozone data from the Total Ozone Mapping Spectrometer (TOMS) aboard Earth Probe, Ozone Monitoring Instrument (OMI) aboard AURA, and the Global Ozone Monitoring Experiment 2 aboard MetOp A (GOME-2A) and MetOp B (GOME-2B), respectively. More specifically, we analyzed: (a) the Earth Probe TOMS version 8 ozone overpass data for Athens (OVP293_epc.txt), which were downloaded from the website https://acdsc.gsfc.nasa.gov/data/EarthProbe_TOMS_Level3/TOMSEPOVP.008/ (last access: 25 June 2021), (b) the OMI version 8.5 (collection 3) ozone overpass data from the website <https://avdc.gsfc.nasa.gov/pub/data/satellite/Aura/OMI/V03/L2OVP/OMTO3/> (last access: 25 June 2021), (c) the GOME-2A level-2 overpass data from the website <https://avdc.gsfc.nasa.gov/pub/data/satellite/MetOp/GOME2/V03/L2OVP/GOME2A/> (last access: 25 June 2021), and (d) the GOME-2B level-2 overpass data from <https://avdc.gsfc.nasa.gov/pub/data/satellite/MetOp/GOME2/V03/L2OVP/GOME2B/> (last access: 25 June 2021). We analyzed the satellite overpass ozone data for the station in Athens and, in addition, we assessed data within a 100 km radius from the Brewer site. Subsequently, we performed correlation analyses between the Brewer and the satellite ozone measurements using daily TOC values for common days between the four data pairs, Brewer and OMI, Brewer and GOME-2A, Brewer and GOME-2B, and Brewer and TOMS, which are presented in Section 3.

The Quasi Biennial Oscillation (QBO) component at 30 hPa on total ozone was examined by analyzing the monthly mean zonal winds at Singapore at 30 hPa (QBO30). For QBO at 50 hPa, we analyzed the monthly mean zonal winds at 50 hPa (QBO50). The data were provided by the Freie Universität Berlin (FU-Berlin) at <http://www.geo.fu-berlin.de/met/ag/strat/produkte/qbo/qbo.dat> (accessed on 8 May 2021) [19]. The possible impact of El Niño Southern Oscillation (ENSO) was examined by using the Southern Oscillation Index (SOI) from the Bureau of Meteorology of the Australian Government (<http://www.bom.gov.au/climate/current/soi2.shtml>) (access on 8 May 2021). The effect of the 11-year solar cycle on total ozone was investigated by analyzing the monthly sunspot number series from the World Data Center/Sunspot Index and Long-term Solar Observations (WDC/SILSO) of the Royal Observatory of Belgium, Brussels (<http://sidc.be/silso/datafiles>) (access on 8 May 2021). The monthly North Atlantic Oscillation (NAO) index was provided from the Climate Data Guide of NCAR at <https://climatedataguide.ucar.edu/climate-data/hurrell-north-atlantic-oscillation-nao-index-pc-based> (access on 8 May 2021).

Total ozone variability is also related to variability related to tropopause height, e.g., [20–22]. The impact of tropopause height variations on total ozone variability was examined by analyzing the tropopause pressure from the National Centers for Environmental Prediction/National Center for Atmospheric Research (NCEP/NCAR) reanalysis 1 data set computed on a 2.5° grid. The NCEP/NCAR reanalysis data were downloaded from the website <https://www.esrl.noaa.gov/psd/data/gridded/data.ncep.reanalysis.tropopause.html> (access on 30 April 2021) [23].

The mean annual ozone cycle was calculated for the period 2004–2018, and then the ozone time series were deseasonalized by subtracting the long-term monthly mean (2004–2018) pertaining to the same calendar month; i.e., monthly value–long-term monthly mean. Next, the deseasonalized data were used in a multivariate linear regression (MLR) model to describe influences of dynamic origin on total ozone variability. The MLR statistical model includes the QBO, SOLAR, ENSO, NAO, and trend terms, as described by Zerefos et al. [24] and later adopted by Eleftheratos et al. [25], for further analyses. Those studies, however, had a slightly different approach, as they also included the effects of aerosol optical depth (AOD) and Antarctic oscillation. Those studies examined stations in the northern and southern mid-latitudes, which justified the inclusion of the Antarctic oscillation in the MLR model. Due to the fact that our station is located in the northern and not in the southern mid-latitudes, we did not include the Antarctic oscillation proxy here. The AOD proxy was used by Zerefos et al. to account for the volcanic injections of El Chichon (1982) and Mt Pinatubo (1991) into the stratosphere, which caused large stratospheric disturbances, increasing ozone depletion. However, the AOD proxy has not been considered in this study, since the mentioned volcanic eruptions occurred in the past and should not affect the period of our analysis. The same procedure, i.e., deseasonalization and MLR analysis, was also applied to the tropopause pressure data, in order to estimate the tropopause pressure residuals (not shown here). Then, the residuals of tropopause pressure from the MLR analysis were correlated with the respective residuals of ozone, in order to determine the effect of tropopause height variations on total ozone variations. The correlation coefficient between the ozone and tropopause pressure residuals was $R = +0.448$ (t -value = 6.533, $p < 0.0001$, $N = 172$). The correlation is presented in Section 3.3.

3. Results and Discussion

3.1. Daily Values and Correlations

The daily column ozone measurements made by the Brewer spectrophotometer at the Academy of Athens from July 2003 to July 2019 are presented in Figure 1. The respective ozone columns retrieved by TOMS, OMI, GOME-2A, and GOME-2B satellite instruments agree fairly well with the ground-based Brewer measurements. The satellite overpass data were selected to be within a 100 km radius from the Brewer site. The daily values span between 250 DU and 500 DU; in full agreement with Tzanis [26], who compared daily column ozone observations from the Dobson spectrophotometer with SCIAMACHY, TOMS, and OMI satellite data. A good agreement between satellite data and a Brewer spectrophotometer has been demonstrated in other studies, for instance in Kim et al. [27], who used a Brewer spectrophotometer to evaluate the quality of the total ozone column (TOC) produced by multiple polar-orbit satellite measurements at three stations in Antarctica. As a result of their study, high correlations between the TOC from the Brewer and the TOC from TROPOMI and OMI measurements were observed, contrary to the correlations from AIRS measurements. The study confirmed the high quality of OMI TOCs.

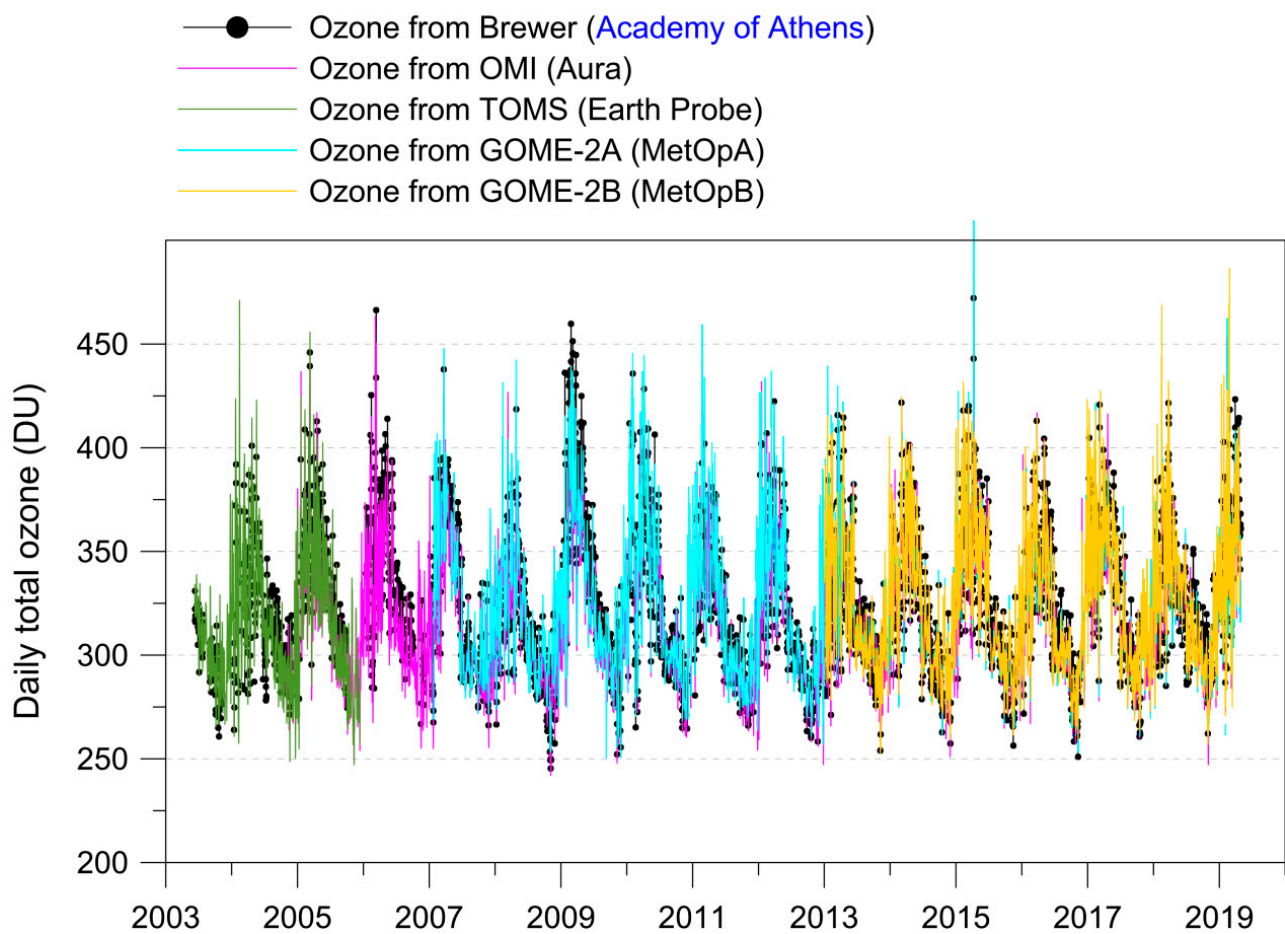


Figure 1. Daily total ozone over Athens, Greece (2003–2019) from Brewer ground-based measurements and OMI, TOMS, and GOME-2A and GOME-2B satellite measurements.

Figure 2 presents the Pearson correlation coefficients, R , the mean biases, the linear fit coefficients, and the root mean square error (RMSE) between ozone from the Brewer spectrophotometer and ozone from each of the satellite instruments. The numbers speak for themselves. The R between the Brewer and OMI, GOME-2A, GOME-2B, and TOMS ozone data are 0.962, 0.955, 0.945, and 0.953, respectively. The mean biases and RMSE between the four data pairs are: 4.4 DU and 9.2 DU (Brewer vs. OMI), -1.7 DU and 10.2 DU (Brewer vs. GOME-2A), -0.1 DU and 10.5 DU (Brewer vs. GOME-2B), and 2.2 DU and 9.0 DU (Brewer vs. TOMS). Accordingly, we provide the mean biases and RMSE between the four satellite data pairs of OMI, TOMS, GOME-2A, and GOME-2B, as follows: -5.3 DU and 7.8 DU (OMI vs. GOME-2A), -4.8 DU and 7.6 DU (OMI vs. GOME-2B), -2.7 DU and 7.7 DU (OMI vs. TOMS), and -1.5 DU and 5.2 DU (GOME-2A vs. GOME-2B). All R were tested for significance using the t -test formula for the correlation coefficient with $n - 2$ degrees of freedom [28] and were found to be statistically significant at a confidence level greater than 99%. More detailed correlation statistics between the various data pairs are provided in Table 1. It is evident that all correlation coefficients pass the significance level (p -values < 0.0001). We include here for the reader the statistical test of the correlation coefficient, which is:

$$t = R\sqrt{\frac{n-2}{1-R^2}} \quad (6)$$

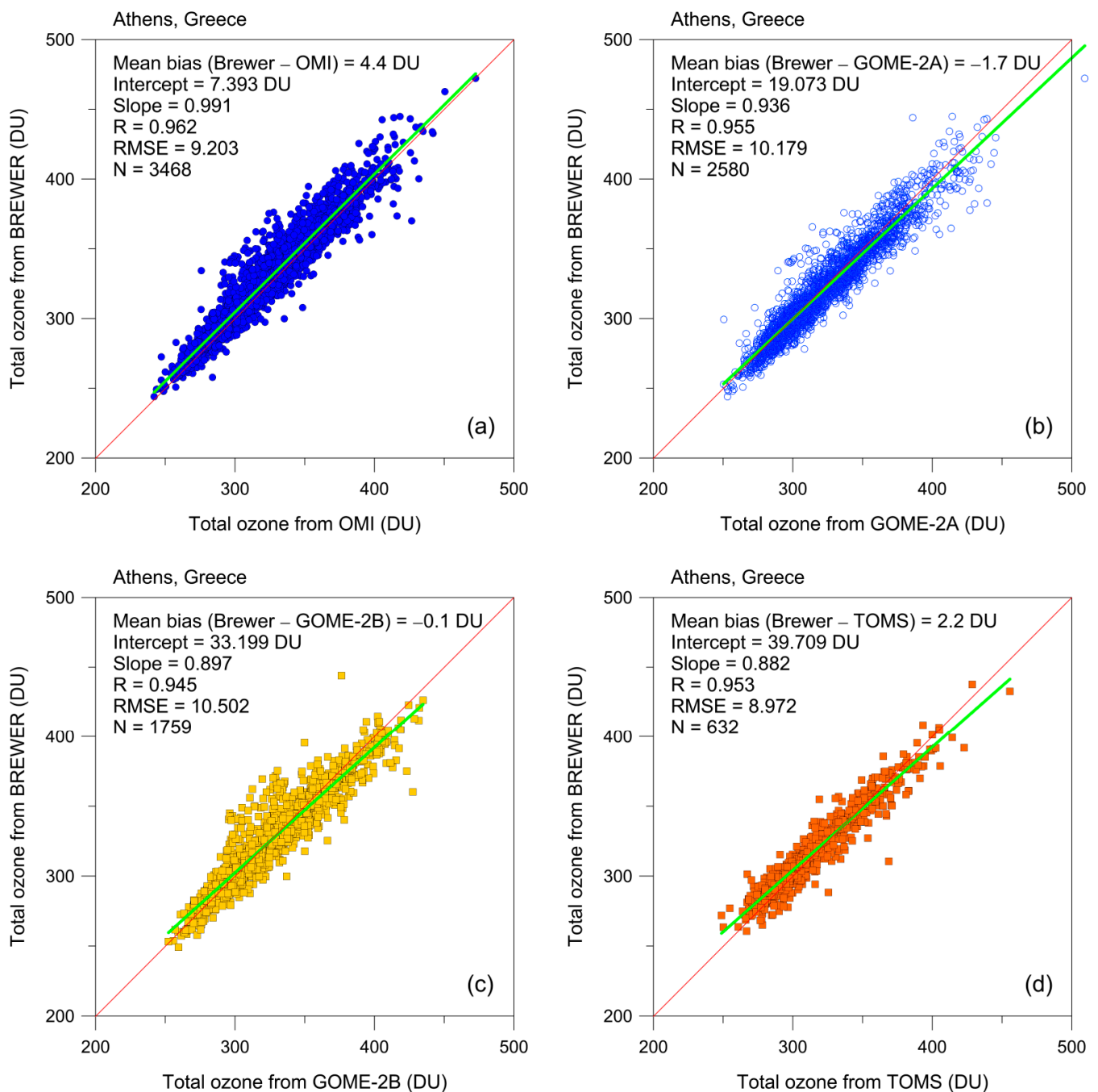


Figure 2. Correlation analysis between the Brewer and satellite ozone measurements for common days: (a) Brewer and OMI; (b) Brewer and GOME-2A; (c) Brewer and GOME-2B; (d) Brewer and TOMS.

3.2. Monthly Means and Annual Cycle

The monthly mean total ozone time series were computed from at least 14 daily averages and are shown in Figure 3 for the Brewer ground-based data in comparison to OMI, TOMS, GOME-2A, and GOME-2B satellite data. The monthly mean values range between 270 DU and 400 DU; again in agreement with results from Tzanis [18]. The long term mean $\pm 2\sigma$ of total ozone over Athens is estimated to be 322 ± 53 DU, with no significant change since 2003. The respective estimates from OMI, TOMS, GOME-2A, and GOME-2B satellite data are 318 ± 51 DU, 316 ± 46 DU, 324 ± 53 DU, and 325 ± 51 DU, accordingly.

Table 1. Statistics of correlations between the Brewer and satellite ozone data pairs.

Data Pair	R	Intercept (DU)	Slope	Error	t-Value	p-Value	RMSE	N
Brewer vs. OMI	+0.962	7.393	0.991	0.005	208.733	<0.0001	9.203	3468
Brewer vs. GOME-2A	+0.955	19.073	0.936	0.006	163.474	<0.0001	10.179	2580
Brewer vs. GOME-2B	+0.945	33.199	0.897	0.007	120.840	<0.0001	10.502	1759
Brewer vs. TOMS	+0.953	39.709	0.882	0.011	79.359	<0.0001	8.972	632
OMI vs. GOME-2A	+0.972	20.026	0.922	0.004	210.739	<0.0001	7.824	2600
OMI vs. GOME-2B	+0.972	20.283	0.923	0.005	169.102	<0.0001	7.593	1668
OMI vs. TOMS	+0.972	25.869	0.909	0.011	83.520	<0.0001	7.736	405
GOME-2A vs. GOME-2B	+0.988	2.591	0.987	0.005	218.776	<0.0001	5.158	1122

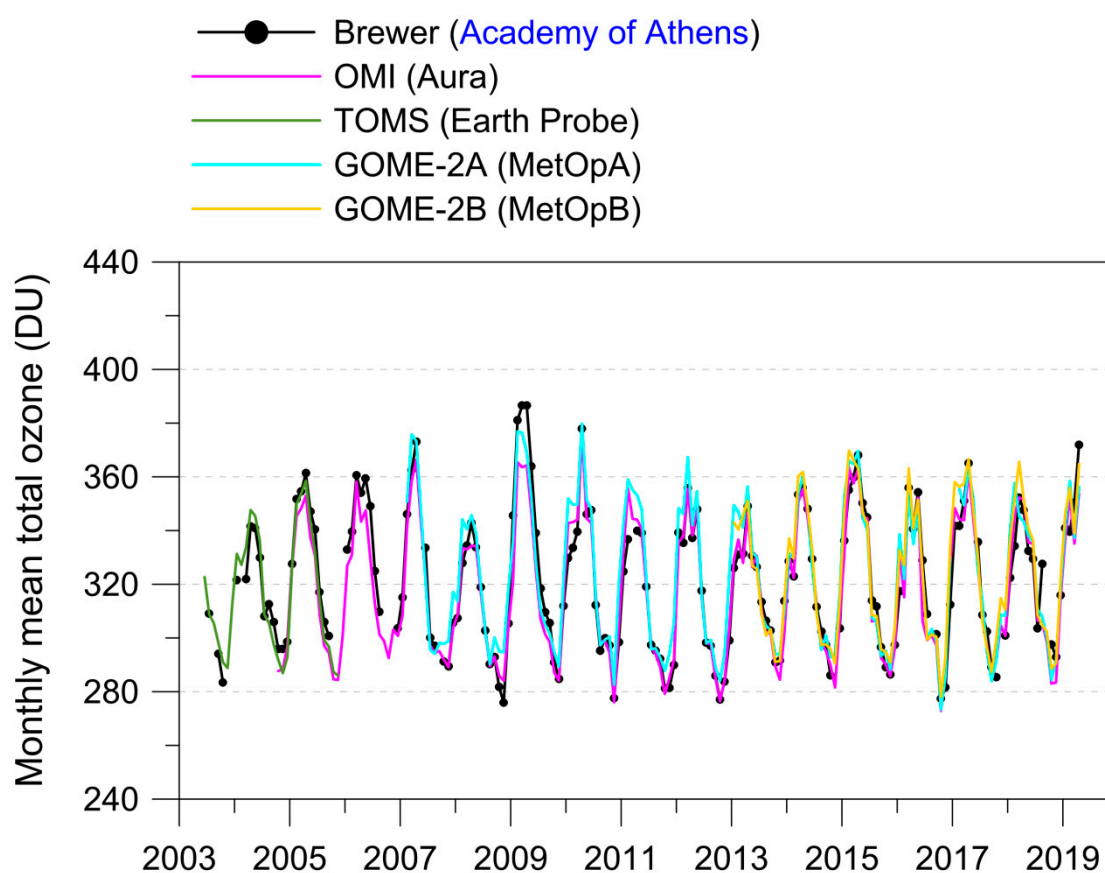
**Figure 3.** Monthly mean total ozone from July 2003 to July 2019 calculated from at least 14 daily averages from Brewer ground-based data, and OMI, TOMS, GOME-2A, and GOME-2B satellite data.

Figure 4 shows the seasonal cycle of total ozone over Athens for the period 2004–2018 from Brewer ground-based measurements and OMI and GOME-2A satellite retrievals. The highest values occurred in spring in March and April, while the lowest values occurred in autumn in October and November. This is a general and consistent feature seen in all three datasets. The explanation for the observed seasonal cycle is transport mechanisms. The spring maximums are a result of the increased transport of ozone from its source region in the tropics toward high latitudes during late autumn and winter. This poleward ozone transport is much weaker during the summer and early autumn periods and is weaker overall in the Southern Hemisphere [2]. Ozone transport from the tropics to the poles is caused by stratospheric wind patterns. In the mid-latitudes these patterns, known as the

Brewer–Dobson circulation, make the ozone layer thickest in the spring and thinnest in the fall.

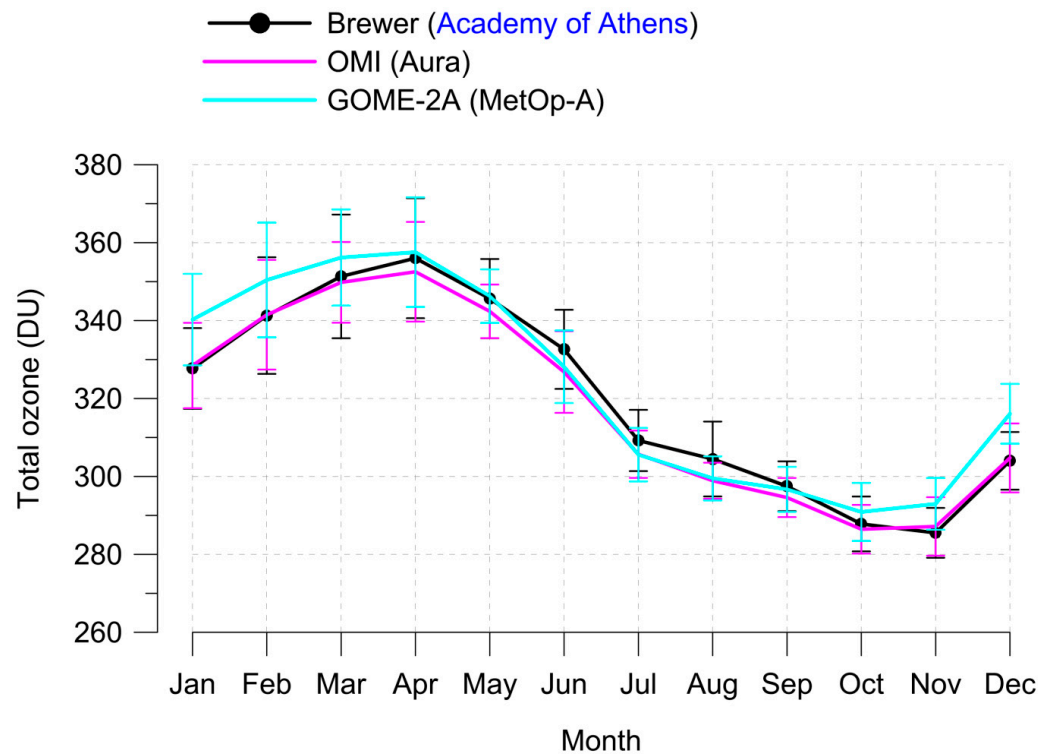


Figure 4. Mean annual cycle of total ozone over Athens, Greece (2004–2018) from Brewer ground-based data, and OMI, GOME-2A satellite data.

Table 2 summarizes the monthly mean differences between the Brewer, OMI, and GOME-2A total ozone data. The Brewer–OMI differences are within $\pm 1\%$ in all months except June, July, and August, where they are within $\pm 2\%$, but even these are considered small. We note here that a difference of 1% corresponds to about 3 DU. Differences larger than $\pm 2\%$ are found between Brewer and GOME-2A in the winter months (November, December, January, and February). Similar deviations, larger than 2%, are also found between GOME-2A and OMI satellite data.

Table 2. Mean differences between Brewer and satellite total ozone data ($1\% \cong 3$ DU).

	Brewer—OMI	Brewer—GOME-2A	GOME-2A—OMI
January	−0.2% (−1 DU)	−3.7% (−13 DU)	3.6% (12 DU)
February	−0.1% (0 DU)	−2.6% (−9 DU)	2.6% (9 DU)
March	0.4% (2 DU)	−1.4% (−5 DU)	1.8% (6 DU)
April	1.0% (3 DU)	−0.4% (−2 DU)	1.4% (5 DU)
May	1.0% (3 DU)	−0.2% (−1 DU)	1.1% (4 DU)
June	1.8% (6 DU)	1.4% (4 DU)	0.4% (1 DU)
July	1.2% (4 DU)	1.2% (4 DU)	0.0% (0 DU)
August	1.9% (6 DU)	1.7% (5 DU)	0.2% (1 DU)
September	1.0% (3 DU)	0.3% (1 DU)	0.7% (2 DU)
October	0.5% (1 DU)	−1.1% (−3 DU)	1.5% (4 DU)
November	−0.6% (−2 DU)	−2.5% (−7 DU)	2.0% (6 DU)
December	−0.2% (−1 DU)	−3.8% (−12 DU)	3.7% (11 DU)
MEAN	0.6% (2 DU)	−0.9% (−3 DU)	1.6% (5 DU)

With regard to the observed differences, we must keep in mind that the Brewer instrument is operating at ground level, while the satellite instruments are measuring from space using different retrieval algorithms than the ground based instrument. The

Brewer instrument is measuring continuously the ozone amount overhead, while the satellite instruments provide few measurements during the day, sometimes one or two measurements. In addition, the Brewer is a remote sensing instrument, while for the satellite data, we processed measurements within a 100 km radius from the Brewer site. The aforementioned issues are known to cause differences between ground measurements and satellite overpasses. However, despite the different approaches of the ground and satellite instruments, the average long-term differences between the ground and satellite measurements are small, within $\pm 1\%$, indicating the maturity of the measuring systems in achieving such small deviations in the long-term.

3.3. Ozone Variability

We estimated the contribution of different explanatory variables to ozone fluctuations using MLR analysis, as explained in Section 2. The MLR statistical model is of the following form:

$$\begin{aligned} \text{desTOC} = & 2.623 + 0.002 \cdot \text{QBO30}(i, j) + 0.111 \cdot \text{QBO50}(i, j) + (-0.093) \\ & \cdot \text{ENSO}(i, j) + 0.678 \cdot \text{NAO}(i, j) + (-0.070) \cdot \text{SOLAR}(i, j) \\ & + 0.003 \cdot \text{TREND}(i, j) + 0.378 \cdot \text{TROP}(i, j) + \text{residuals} \end{aligned} \quad (7)$$

where i denotes the month and j is the year of the deseasonalized total ozone column (desTOC) and its components; that is, the QBO at 30 and 50 hPa, the ENSO, the NAO, the solar cycle effect (SOLAR), a straight line to fit the long term trend (TREND), and finally a tropopause pressure related term (TROP). We remind here that TOC data were deseasonalized by subtracting the long-term monthly mean (2004–2018) pertaining to the same calendar month. The contribution of the individual proxy terms is shown in Figure 5. The MLR analysis was applied to the deseasonalized ozone data, which are shown on the top panel of Figure 5 (black line). The two terms representing the QBO are shown by the lines with blue colors, followed by the ENSO term (red line), the NAO term (green line), the solar cycle term (orange line), and the trend term (brown line). The bottom panel of Figure 5 shows the residuals of ozone from the MLR model (grey color), together with the respective residuals of tropopause pressure from an MLR analysis that had been applied to the tropopause data in a previous step (magenta color). The ozone residuals are well correlated with the tropopause pressure residuals, indicating the dynamical influence on ozone induced by the tropopause movement. The graph shows that whenever the tropopause pressure decreases, i.e., tropopause height increases, the amount of ozone increases, and vice versa. We estimate that the correlation coefficient between ozone and tropopause height variations in Athens is $+0.448$ (slope = 0.376, error = 0.058, t -value = 6.533, $p < 0.0001$, $N = 172$).

The MLR regression coefficients and their standard errors are presented in Table 3. It appears that the regression coefficient of the QBO50 proxy is significant at the 90% confidence level (coefficient = 0.111, error = 0.059, t -value = 1.874, p -value = 0.063). The regression coefficient of the solar proxy is more significant than the QBO50 proxy (coefficient = -0.070 , error = 0.018, t -value = -3.853 , p -value = 0.00017). The regression coefficient of the trend proxy is not statistically significant (coefficient = 0.003, error = 0.013, t -value = 0.249, p -value = 0.803). Finally, the regression coefficient of the tropopause proxy is 0.378 ± 0.059 (t -value = 6.459, p -value < 0.0001).

Figure 6 summarizes the monthly ozone data from the Brewer spectrophotometer, the seasonal cycle, the QBO (30 hPa, 50 hPa), ENSO, NAO, solar cycle and trend components joined together, and an estimated tropopause pressure related component. The amplitude of the annual cycle, calculated as ((maximum value–minimum value)/2), is about 35 DU and is estimated to contribute to about 64% to the observed ozone fluctuations. The QBO, ENSO, NAO, SOLAR, and TREND terms are estimated to together explain about 11% of the observed ozone fluctuations. Adding a tropopause pressure related term, the statistical model explains about 27% of ozone fluctuations.

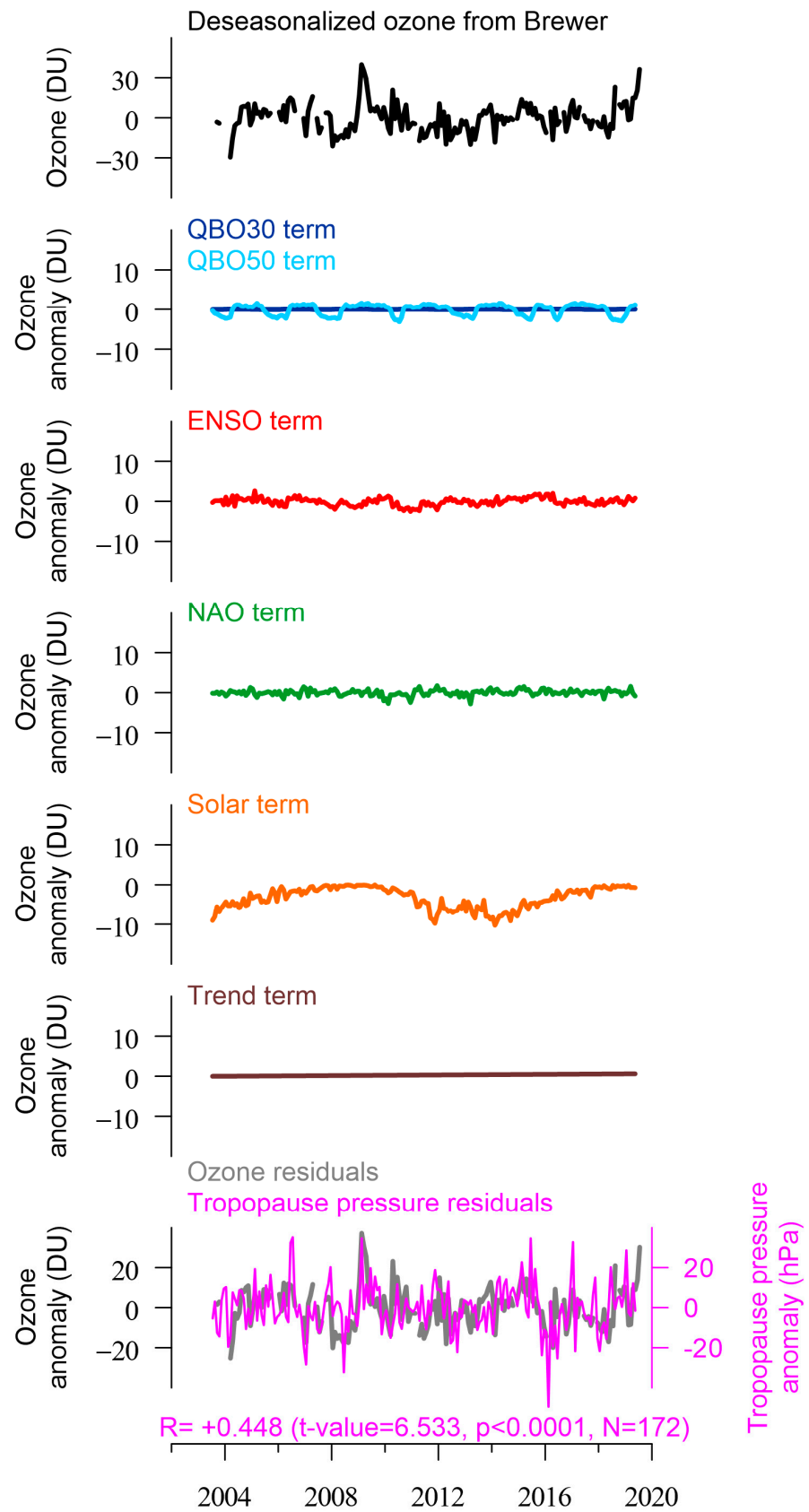
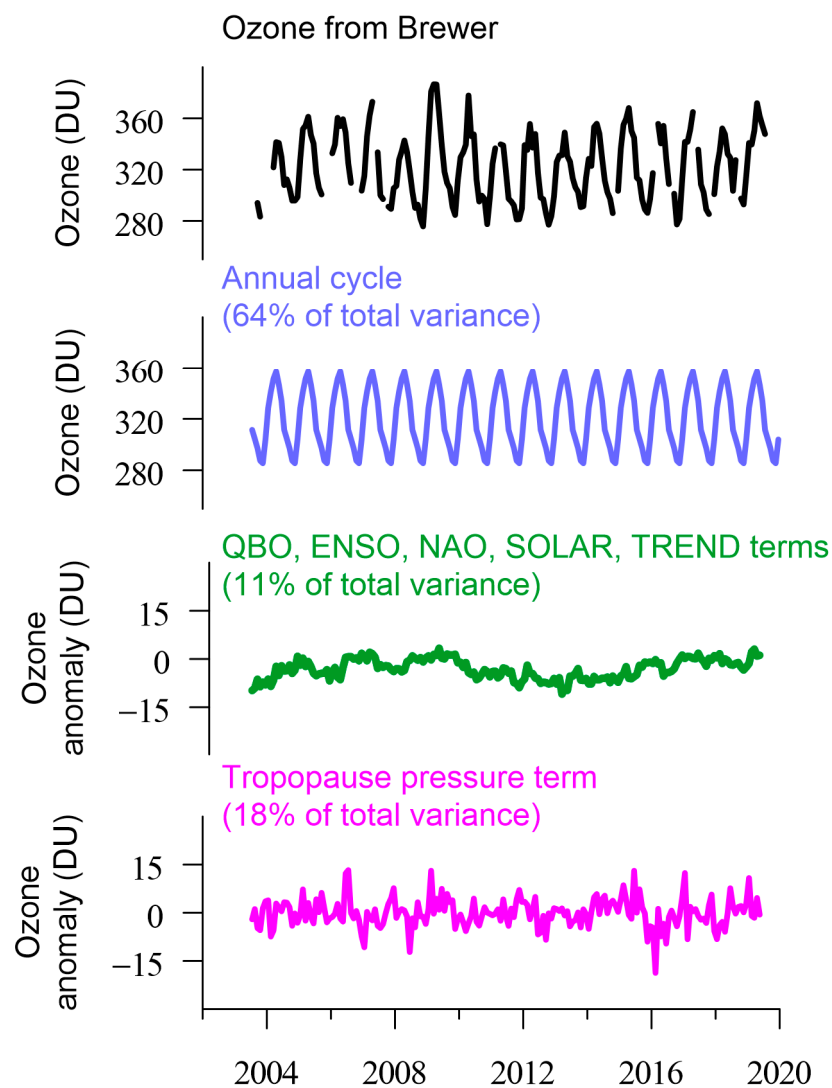


Figure 5. Contribution of different explanatory variables to ozone fluctuations over Athens, Greece, obtained from the MLR analysis. The bottom panel shows the residuals of ozone as related to the respective residuals of tropopause pressure.

Table 3. MLR regression statistics for the proxy terms considered in Equation (7).

MLR Regression Statistics	Coefficient	Error	<i>t</i> -Value	<i>p</i> -Value
Intercept	2.623	1.683	1.556	0.12102
QBO at 30 hPa	0.002	0.039	0.047	0.96233
QBO at 50 hPa	0.111	0.059	1.874	0.06272
ENSO	−0.093	0.069	−1.348	0.17953
NAO	0.678	0.632	1.073	0.28472
SOLAR	−0.070	0.018	−3.853	0.00017
TREND	0.003	0.013	0.249	0.80335
TROPOPAUSE	0.378	0.059	6.459	1.15×10^9

**Figure 6.** Time series of monthly ozone from the Brewer spectrophotometer versus the annual cycle; the QBO, ENSO, NAO, SOLAR, TREND terms grouped together; and the tropopause pressure term separately. The highest contribution comes from the seasonal cycle (see text).

The contribution of all components to ozone fluctuations cumulatively is presented in Figure 7, which shows the observed versus the regressed ozone data. As can be seen, there is good agreement between the observed ozone data and the statistical model calculations obtained from Equation (7). The correlation coefficient between the observed and regressed ozone data is estimated as $R = +0.941$. The residuals (observed minus regressed data) are shown in the bottom panel.

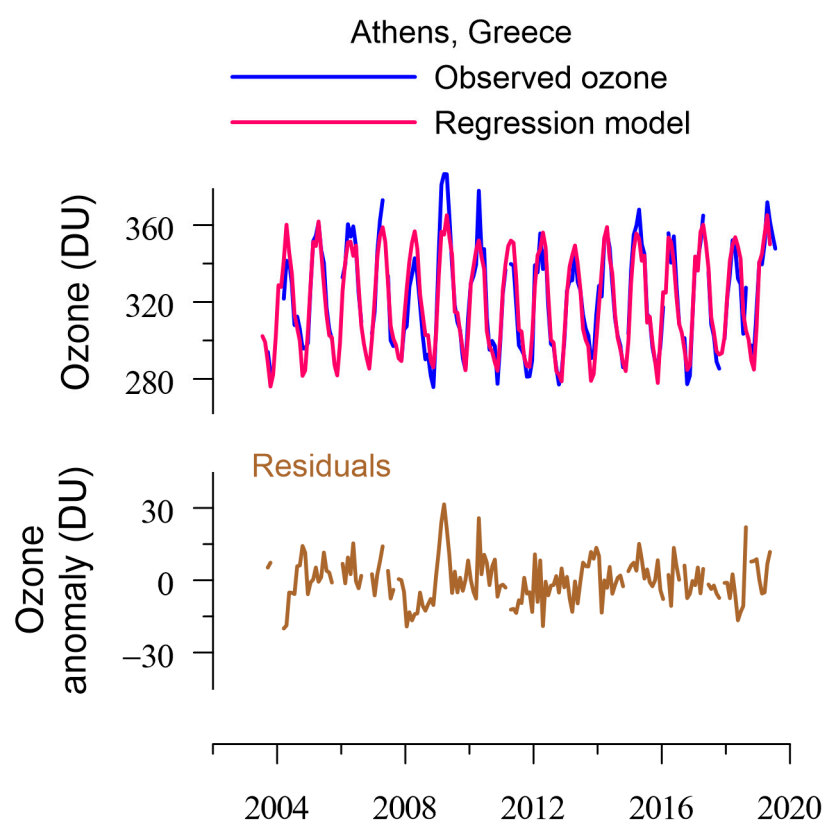


Figure 7. Observed and regressed columnar ozone over Athens, Greece, and respective residuals (observed–regressed).

4. Conclusions

We analyzed 16 years of total ozone measurements over Athens, Greece, with a Brewer spectrophotometer. The main findings can be summarized as follows:

- There are strong correlations between total ozone from the Brewer spectrophotometer and total ozone from the OMI, TOMS, GOME-2A and GOME-2B satellite instruments greater than 0.9.
- The main contribution to ozone variability comes from the seasonal cycle. We estimate that the seasonal variability explains about 64% of the variability in total ozone over Athens.
- Natural fluctuations (QBO, ENSO, NAO, solar cycle trend) together explain about 11% of total ozone variability. Adding the variability related to the tropopause pressure, the multiple linear regression model explains about 27% of ozone fluctuations.
- Accounting for seasonal, solar cycle, and tropopause pressure variability in a statistical regression model, we can simulate the variability of total ozone over Athens quite well.
- We estimate a small, insignificant change in total ozone over Athens, Greece, during the period 2003–2019 of 0.6 ± 4.9 DU (change ± 2 standard error limits).

Supplementary Materials: The following are available online at <https://www.mdpi.com/article/10.3390/oxygen1010005/s1>, Figure S1: Information about the stability of the Brewer spectrophotometer according to the calibrations of the instrument in (1) 2004, (2) 2007, (3) 2010, (4) 2013 and (5) 2019.

Author Contributions: Conceptualization, K.E.; methodology, K.E., C.Z.; software, K.E.; formal analysis, K.E.; investigation, K.E., D.K., C.Z.; data curation, K.E., D.K.; writing—original draft preparation, K.E., D.K.; writing—review and editing, K.E., D.K.; visualization, K.E.; supervision, C.Z.; project administration, K.E., D.K.; funding acquisition, K.E., C.Z. All authors have read and agreed to the published version of the manuscript.

Funding: This research was partially funded by the Hellenic Foundation for Research and Innovation (H.F.R.I.) under the “First Call for H.F.R.I. Research Projects to support Faculty members and Researchers and the procurement of high-cost research equipment grant” (Project Number: 300).

Institutional Review Board Statement: Not applicable.

Informed Consent Statement: Not applicable.

Data Availability Statement: Brewer ozone data are submitted to WOUDC (Station ID 449-Academy of Athens) (<https://woudc.org/data/stations/>) (accessed on 25 June 2021). OMI and GOME-2 satellite ozone data were downloaded from the NASA Aura Validation Data Center (<https://avdc.gsfc.nasa.gov/index.php?site=599065317>) (access on 8 May 2021). The QBO data were provided by FU-Berlin (<http://www.geo.fu-berlin.de/met/ag/strat/produkte/qbo/qbo.dat>) (last access: 8 May 2021). The SOI data were provided from the Bureau of Meteorology of the Australian Government (<http://www.bom.gov.au/climate/current/soi2.shtml>) (access on 8 May 2021). The sunspots numbers were provided from the WDC Sunspot Index and Long-term Solar Observations of the Royal Observatory of Belgium, Brussels (<http://sidc.be/silso/datafiles>) (access on 8 May 2021). The NAO index was provided from NCAR Climate Data Guide (<https://climatedataguide.ucar.edu/climate-data/hurrell-north-atlantic-oscillation-nao-index-pc-based>) (access on 8 May 2021).

Acknowledgments: We acknowledge support and funding of this work by the project “Panhellenic Infrastructure for Atmospheric Composition and Climate Change” (MIS 5021516), which is implemented under the action “Reinforcement of the Research and Innovation Infrastructure”, funded by the Operational Program “Competitiveness, Entrepreneurship and Innovation” (NSRF 2014–2020) and co-financed by Greece and the European Union (European Regional Development Fund).

Conflicts of Interest: The authors declare no conflict of interest.

References

1. Langematz, U. Stratospheric ozone: Down and up through the anthropocene. *ChemTexts* **2019**, *5*, 8. [CrossRef]
2. Salawitch, R.J.; Fahey, D.W.; Hegglin, M.I.; McBride, L.A.; Tribett, W.R.; Doherty, S.J. *Twenty Questions and Answers About the Ozone Layer: 2018 Update, Scientific Assessment of Ozone Depletion: 2018*; World Meteorological Organization: Geneva, Switzerland, 2019; p. 84.
3. Bais, A.F.; Bernhard, G.; McKenzie, R.L.; Aucamp, P.J.; Young, P.J.; Ilyas, M.; Jöckel, P.; Deushi, M. Ozone–climate interactions and effects on solar ultraviolet radiation. *Photochem. Photobiol. Sci.* **2019**, *18*, 602–640. [CrossRef] [PubMed]
4. Bais, A.F.; McKenzie, R.L.; Bernhard, G.; Aucamp, P.J.; Ilyas, M.; Madronich, S.; Tourpali, K. Ozone depletion and climate change: Impacts on UV radiation. *Photochem. Photobiol. Sci.* **2014**, *14*, 19–52. [CrossRef] [PubMed]
5. Varotsos, C.A.; Cracknell, A.P. Three years of total ozone measurements over Athens obtained using the remote sensing technique of a Dobson spectrophotometer. *Int. J. Remote Sens.* **1994**, *15*, 1519–1524. [CrossRef]
6. Varotsos, C.A. Total ozone measurements over Athens: Intercomparison between Dobson, TOMS (version 6) and SBUV measurements. *Int. J. Remote Sens.* **1998**, *19*, 3327–3333. [CrossRef]
7. Fragkos, K.; Taylor, M.; Bais, A.F.; Fountoulakis, I.; Tourpali, K.; Meleti, C.; Zempila, M.M. Multi-decadal Trend Analysis of Total Columnar Ozone Over Thessaloniki. In *Perspectives on Atmospheric Sciences*; Karacostas, T.S., Bais, A.F., Nastos, P.T., Eds.; Springer Atmospheric Sciences, Springer International Publishing: Cham, Switzerland, 2017; pp. 983–988. [CrossRef]
8. World Meteorological Organization. *Scientific Assessment of Ozone Depletion: 2010*; Report No. 52; Global Ozone Research and Monitoring Project: Geneva, Switzerland, 2011; p. 516.
9. Zerefos Lab. Available online: <http://www.bioacademy.gr/lab/zerefos> (accessed on 25 June 2021).
10. Gerasopoulos, E.; Kokkalis, P.; Amiridis, V.; Liakakou, E.; Perez, C.; Hausteiner, K.; Eleftheratos, K.; Andreae, M.; Andreae, T.W.; Zerefos, C.S.; et al. Dust specific extinction cross-sections over the Eastern Mediterranean using the BSC-DREAM model and sun photometer data: The case of urban environments. *Ann. Geophys.* **2009**, *27*, 2903–2912. [CrossRef]
11. Kerr, J.B.; McElroy, C.T.; Olafson, R.A. Measurements of ozone with the Brewer ozone spectrophotometer. In Proceedings of the Quadrennial Ozone Symposium, Boulder, CO, USA, 4–9 August 1981; London, J., Ed.; National Center for Atmospheric Research: Boulder, CO, USA, 1980; pp. 74–79.
12. Kerr, J.B. The Brewer Spectrophotometer. In *UV Radiation in Global Climate Change*; Gao, W., Schmoldt, D.L., Slusser, J.R., Eds.; Springer: Berlin/Heidelberg, Germany, 2010; pp. 160–191. [CrossRef]
13. Software for Ozone Spectrophotometers. Available online: <http://www.o3soft.eu/o3brewer.html> (accessed on 30 April 2021).
14. Kazantzidis, A.; Bais, A.F.; Zempila, M.M.; Meleti, C.; Eleftheratos, K.; Zerefos, C.S. Evaluation of ozone column measurements over Greece with NILU-UV multi-channel radiometers. *Int. J. Remote Sens.* **2009**, *30*, 4273–4281. [CrossRef]
15. Raptis, P.I.; Kazadzis, S.; Eleftheratos, K.; Kosmopoulos, P.; Amiridis, V.; Helmis, C.; Zerefos, C. Total ozone column measurements using an ultraviolet multi-filter radiometer. *Int. J. Remote Sens.* **2015**, *36*, 4469–4482. [CrossRef]

16. Fioletov, V.E.; Kerr, J.B.; Wardle, D.I.; Wu, E. Correction of stray light for the Brewer single monochromator. In *Atmospheric Ozone, Proceedings of the Quadrennial Ozone Symposium, Hokkaido University, Sapporo, Japan, 3–8 July 2000*; Shibasaki, K., Bojkov, R.D., Eds.; Hokkaido University: Sapporo, Japan, 2000; pp. 371–372.
17. Weatherhead, E.; Theisen, D.; Stevermer, A.; Enagonio, J.; Rabinovitch, B.; Disterhoft, P.; Lantz, K.; Meltzer, R.; DeLuisi, J.; Rives, J.; et al. Temperature dependence of the Brewer ultraviolet data. *J. Geophys. Res. Space Phys.* **2001**, *106*, 34121–34129. [[CrossRef](#)]
18. Zanjani, Z.V.; Moeini, O.; McElroy, T.; Barton, D.; Savastiouk, V. A calibration procedure which accounts for non-linearity in single-monochromator Brewer ozone spectrophotometer measurements. *Atmos. Meas. Tech.* **2019**, *12*, 271–279. [[CrossRef](#)]
19. Naujokat, B. An Update of the Observed Quasi-Biennial Oscillation of the Stratospheric Winds over the Tropics. *J. Atmospheric Sci.* **1986**, *43*, 1873–1877. [[CrossRef](#)]
20. Dameris, M.; Nodorp, D.; Sausen, R. Correlation between Tropopause Height Pressure and TOMS-Data for the EASOE-Winter 1991/1992. *Beitr. Phys. Atmos.* **1995**, *68*, 227–232.
21. Hoinka, K.P.; Claude, H.; Köhler, U. On the correlation between tropopause pressure and ozone above central Europe. *Geophys. Res. Lett.* **1996**, *23*, 1753–1756. [[CrossRef](#)]
22. Steinbrecht, W.; Claude, H.; Köhler, U.; Hoinka, K.P. Correlations between tropopause height and total ozone: Implications for long-term changes. *J. Geophys. Res. Space Phys.* **1998**, *103*, 19183–19192. [[CrossRef](#)]
23. Kalnay, E.; Kanamitsu, M.; Kistler, R.; Collins, W.; Deaven, D.; Gandin, L.; Iredell, M.; Saha, S.; White, G.; Woollen, J.; et al. The NCEP/NCAR 40-year reanalysis project. *Bull. Am. Meteorol. Soc.* **1996**, *77*, 437–472. [[CrossRef](#)]
24. Zerefos, C.; Kapsomenakis, J.; Eleftheratos, K.; Tourpali, K.; Petropavlovskikh, I.; Hubert, D.; Godin-Beekmann, S.; Steinbrecht, W.; Frith, S.; Sofieva, V.; et al. Representativeness of single lidar stations for zonally averaged ozone profiles, their trends and attribution to proxies. *Atmos. Chem. Phys. Discuss.* **2018**, *18*, 6427–6440. [[CrossRef](#)]
25. Eleftheratos, K.; Kapsomenakis, J.; Zerefos, C.S.; Bais, A.F.; Fountoulakis, I.; Dameris, M.; Jöckel, P.; Haslerud, A.S.; Godin-Beekmann, S.; Steinbrecht, W.; et al. Possible Effects of Greenhouse Gases to Ozone Profiles and DNA Active UV-B Irradiance at Ground Level. *Atmosphere* **2020**, *11*, 228. [[CrossRef](#)]
26. Tzanis, C. Total ozone observations at Athens, Greece by satellite-borne and ground-based instrumentation. *Int. J. Remote Sens.* **2009**, *30*, 6023–6033. [[CrossRef](#)]
27. Kim, S.; Park, S.-J.; Lee, H.; Ahn, D.; Jung, Y.; Choi, T.; Lee, B.; Kim, S.-J.; Koo, J.-H. Evaluation of Total Ozone Column from Multiple Satellite Measurements in the Antarctic Using the Brewer Spectrophotometer. *Remote Sens.* **2021**, *13*, 1594. [[CrossRef](#)]
28. von Storch, H.; Zwiers, F.W. *Statistical Analysis in Climate Research*; Cambridge University Press: Cambridge, UK, 1999; 484p, ISBN 0521450713.